



Analysing phases of matter based on Tensor Train Format

Gabin Leroy

Supervisors : Prof. Chisa Hotta, Prof. Frederic Mila

April 10, 2024

Contents

List of abbreviations	3
Abstract	4
1 Introduction	6
1.1 Basics of characterizing quantum many-body states	6
1.1.1 Quantum many-body states	6
1.1.2 Entanglement and Schmidt decomposition	7
1.1.3 Computing the Schmidt values using reduced density matrix formalism	8
1.1.4 Physical implications	10
1.2 Matrix product state	11
1.2.1 Tensor: definitions and diagrammatic representation	11
1.2.2 Grouping indices	11
1.2.3 Singular value decomposition theorem	12
1.2.4 MPS representation	14
1.2.5 Bond dimension and truncation	15
1.2.6 Entanglement entropy in the context of MPS	16
1.2.7 Application on random data	17
1.3 Phases of matter of interest	20
1.3.1 2D classical Ising model	20
1.3.2 Spin glasses	21
1.4 Analyzing snapshots of phases	27
1.4.1 Scale decomposition and MPS construction	27
1.4.2 Image compression using MPS	28
1.4.3 Snapshot analysis of 2D Ising model	29
2 Encoding data as Quantum state	31
2.1 Tensor train format of data	31
2.1.1 Mapping coordinates using their base q representation	31
2.1.2 Regrouped Scale Tensor Train Format (RSTTF)	33
2.2 Data encoding	35
2.2.1 2D Snapshot and image compression	35
2.2.2 Quantum Cantor state	36
2.3 Interscale entanglement entropy and bond dimension	39
2.3.1 Physical interpretation of bond dimension	39

3 Analyses of phases using tensor train format	43
3.1 Self-similarity	43
3.1.1 Quantum cantor set	43
3.1.2 Self-similar objects	52
3.1.3 Correlation length	57
3.2 Normal image and random data	61
3.3 2D Ising model on the square lattice	62
3.3.1 Numerical analysis	62
3.4 Spin-Glass	76
3.4.1 Data available	76
3.4.2 Raw and overlap snapshots	76
4 Conclusion	88
Acknowledgements	90

List of Abbreviations

EE Entanglement Entropy

MPS Matrix Product State

MC Monte Carlo

SK Sherrington-Kirkpatrick

RSB Replica Symmetry Breaking

RS Replica Symmetric

SVD Singular Value Decomposition

PBC Periodic Boundary Condition

RSTTF Regrouped Scale Tensor Train Format

RSMLT Regrouped Scale Multi Leg Tensor

QCS Quantum Cantor State

MSE Mean Squared Error

Abstract

Understanding the structures of classical phases has been a longstanding pursuit in condensed matter physics. In this thesis, we delve into a novel method that aims to detect certain classical phases based on the real space microstates of spins and the presence of a global structure.

A commonly used method to detect these phases involves computing the correlation length, which entails a significant number of Monte Carlo samples, making it numerically costly, particularly for the most difficult classical problems including spin glasses.

The method consists of representing the real space data in a tensor train format (also known as matrix product states), where physical indices represent different scales of the data. We then map the tensor to a quantum state, enabling quantum mechanical entanglement between consecutive physical indices to signify the entanglement between different scales of the data. This format provides a systematic way to numerically compute the inter-scale entanglement entropy, offering deeper insights into the underlying organization of classical spins in the lattice. The main ingredient of this method will be snapshots of spins belonging to different characteristic phases.

Our first objective is to understand and clarify the physical meaning of the inter-scale entanglement entropy and bond dimension through rigorous treatment, revealing a simple interpretation where the bond dimension can be regarded as the number of independent sub-snapshots needed to compose the data at that scale. Subsequently, we will analyze it on sets with a self-similar structure, beginning with the Cantor set and then broadening the analysis to general self-similar objects. This will provide a better understanding of this quantity.

Finally, we will conduct numerical experiments on two classical phases: the 2D ferromagnetic Ising model on a square lattice and the Heisenberg Edwards-Anderson model of spin glass. We find that encoding real space data in the tensor train format detects the phase transition from the ferromagnetic to paramagnetic phase in the 2D Ising model using a very small number of Monte Carlo samples. Additionally, the method allows us to identify the critical temperature. Moreover, we can detect the development of correlations in the spin glass overlap snapshots.

In conclusion, our findings suggest that the proposed approach can effectively detect critical phases in two-dimensional systems that present some global structure of spins, as well as self-similar structures.

In the first chapter, we will set the scene by briefly recalling some generalities on quantum many-body states, emphasizing the notion of entanglement and explaining how to compute it using the local density matrix as well as the Schmidt decomposition theorem. We will provide a detailed explanation of how to represent any tensor as a Matrix Product State (MPS) and how to compute the Entanglement Entropy of a quantum state for any bipartition of space using its MPS form. The chapter will conclude by presenting the theory of the phases we will analyze and by reviewing some recent work on MPS that motivated this study.

In Chapter 2, we present the primary method of expressing any data in a discrete D -dimensional cube as a multi-leg tensor, aiming to separate the different scales. We will explain how to map it to a quantum state and interpret Entanglement Entropy and bond dimension in this context. The discussion will be supplemented with numerous examples.

Finally, in Chapter 3, we construct what we call the Quantum Cantor State (QCS), which is the quantum state associated with the well-known Cantor set, and extract some properties of Entanglement Entropy and bond dimension. Motivated by this problem, we will provide a unique characterization of self-similar objects through inter-scale Entanglement Entropy and bond dimension. Subsequently, we will apply the method to two known models: the 2D Ising model on a square lattice with ferromagnetic interactions and the spin glass Heisenberg Edwards-Anderson model. For both models, we will compute the Entanglement Entropy and bond dimension as a function of the bond index and analyze the results.

Chapter 1

Introduction

In the first half of this Chapter, we overview the preliminaries of how to describe or analyze quantum many-body states with a particular emphasis on the matrix product state (MPS) representation. Using the techniques related to MPS, the thesis deals with two characteristic phases of condensed matter, which are the two-dimensional critical phase realized in the classical Ising model and the classical spin glass phase calculated for a three-dimensional cubic lattice with random Heisenberg interactions. Therefore, we briefly introduce the basic properties of these two phases. In the final part of this Chapter, we overview a few closely related works; recent proposal of compressing the data using the tensor train, image compression, and analyzing 2D Ising criticality by the Schmidt decomposition. These ideas are to be integrated into our work which will be presented shortly after this Chapter.

1.1 Basics of characterizing quantum many-body states

1.1.1 Quantum many-body states

A *quantum many-body state* $|\psi\rangle$ lives in a Hilbert space \mathbb{H} that is the tensorial product of the individual Hilbert space associated with each body \mathbb{H}_i :

$$\mathbb{H} = \otimes_{i=1}^N \mathbb{H}_i$$

where N is the number of particles/bodies.

A basis of the Hilbert space \mathbb{H} is obtained by making the tensorial product of the basis of each Hilbert space. In this thesis, we will focus on finite-size Hilbert space, so a finite basis exists for each of these vector spaces. If $\{|i_j\rangle\}$ is the basis of Hilbert space \mathbb{H}_j , then a basis of \mathbb{H} can be written $\mathbb{H} = \{|i_1, \dots, i_j\rangle\}$ where $|i_1, \dots, i_j\rangle$ is a short hand notation for $|i_1\rangle \otimes \dots \otimes |i_j\rangle$. This basis is called the *tensorial product basis* and its dimension equals the product of the dimension of each Hilbert space $\dim \mathbb{H} = \prod_{i=1}^N \dim \mathbb{H}_i$. Hence, any quantum many-body state living in \mathbb{H} , can be written as

$$|\psi\rangle = \sum_{i_1, \dots, i_j} \psi_{i_1, \dots, i_j} |i_1, \dots, i_j\rangle \tag{1.1}$$

where the sum runs over all basis elements of the tensorial product basis and $\psi_{i_1, \dots, i_j} = \langle i_1, \dots, i_j | \psi \rangle$ if we take each basis orthonormal.

1.1.2 Entanglement and Schmidt decomposition

Let us bipartite the many-body Hilbert space \mathbb{H} into two Hilbert spaces as $\mathbb{H} = \mathbb{H}_A \otimes \mathbb{H}_B$. We call $\{|i_A\rangle\}$ an orthonormal basis of \mathbb{H}_A and $\{|i_B\rangle\}$ an orthonormal basis of \mathbb{H}_B , and introduce $|\psi\rangle \in \mathbb{H}_A \otimes \mathbb{H}_B$ as a normalized many body quantum state. We denote $n_A = \dim(\mathbb{H}_A)$ and $n_B = \dim(\mathbb{H}_B)$. Then, the Schmidt decomposition theorem holds :

Theorem 1.1.1 (Schmidt decomposition.). *There exist orthonormal sets $\{|a_1\rangle, \dots, |a_m\rangle\} \subset \mathbb{H}_A$ and $\{|b_1\rangle, \dots, |b_m\rangle\} \subset \mathbb{H}_B$ such that $m = \min(n_A, n_B)$ and*

$$|\psi\rangle = \sum_{i=1}^m s_i |a_i\rangle \otimes |b_i\rangle \quad (1.2)$$

where $s_i \in \mathbb{R}_+$. The set of non-zero s_i are unique up to reordering and are called the Schmidt values. The number of non-zero Schmidt values, called $1 \leq r \leq m$ is called the Schmidt rank.

The convention is to order the Schmidt values $s_1 \geq s_2 \geq \dots \geq s_r > 0$. The quantum state $|\psi\rangle$ living in bipartite Hilbert space $\mathbb{H}_A \otimes \mathbb{H}_B$ is said to be *entangled* if $r \geq 2$. If $r = 1$, then the state is said to be a *pure state* or a *tensorial product state*.

We can also deduce from that theorem some properties on the Schmidt values. We have

$$\langle \psi | \psi \rangle = \sum_{i,j=1}^m s_i s_j (\langle a_i | \otimes \langle b_i |) (\langle a_j | \otimes \langle b_j |) \quad (1.3)$$

$$= \sum_{i=1}^m s_i^2 = \sum_{i=1}^r s_i^2 \quad (1.4)$$

$$= 1 \quad (1.5)$$

and hence the sum of the squared Schmidt values equals 1. This implies that all Schmidt values squared are in $[0, 1]$, and hence for a pure state, there is only one non-zero Schmidt value $s_1 = 1$. The proof of the theorem requires the singular value decomposition (SVD) theorem, which will be presented later. From the Schmidt decomposition, one can define a quantity called the *Von Neumann entanglement entropy*.

Definition 1.1.1 (Von Neumann entanglement entropy (EE)). The Von Neumann EE, S_{AB} , between subsystems \mathbb{H}_A and \mathbb{H}_B of the quantum state $|\psi\rangle \in \mathbb{H}_A \otimes \mathbb{H}_B$ is defined as

$$S_{AB} = - \sum_{i=1}^m s_i^2 \ln(s_i^2) \quad (1.6)$$

Taking a base 2 log or any other log only changes S_{AB} by a constant.

One notices that S_{AB} is the statistical entropy of a random variable \hat{X} with distribution $p_i : \{p_1 = s_1^2, \dots, p_m = s_m^2\}$ on the discrete set $\llbracket 1, m \rrbracket$, where by definition $p_{r+1} = p_{r+2} = \dots = p_m = 0$.

Properties 1.1.1. The quantity S_{AB} verifies

$$0 \leq S_{AB} \leq \ln(r)$$

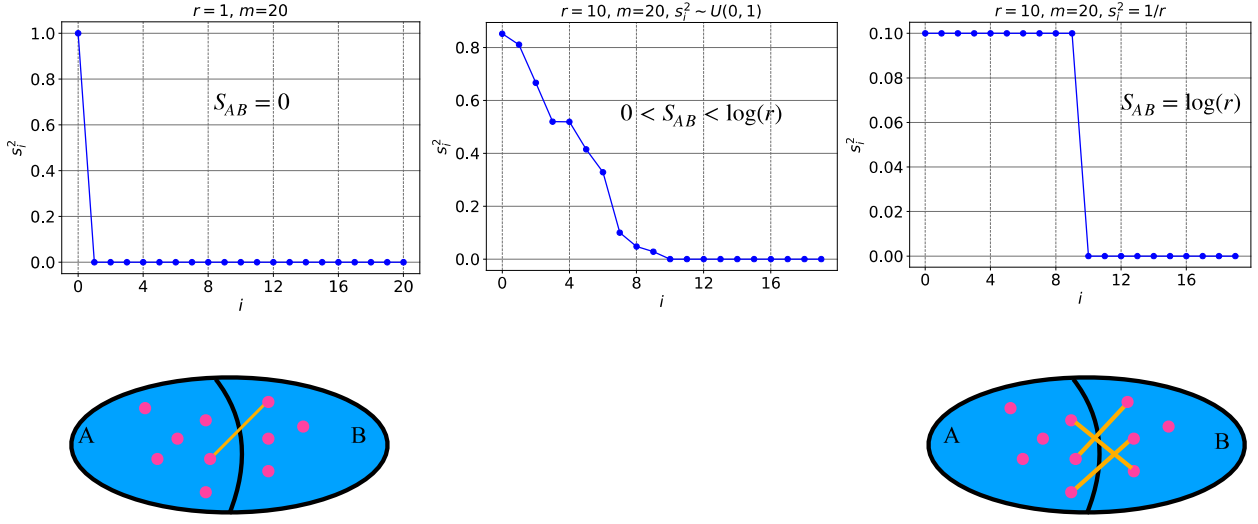


Figure 1.1: The left figure shows the distribution of Schmidt values for $r = 1$, corresponding to a pure state. The middle and right figure corresponds to an entangled state with Schmidt rank $r = 10$. The middle has Schmidt values uniformly distributed, and the right one has constant Schmidt values, where \hat{X} is uniform.

and satisfies the following two properties: Firstly, S_{AB} is maximal if and only if \hat{X} has a uniform distribution : $p_i = s_i^2 = \frac{1}{m}$ for all $i \in \llbracket 1, r \rrbracket$. Second, $S_{AB} = 0$ if and only if \hat{X} takes a value x with probability one. Then, it means that $s_1 = 1$ and $s_i = 0$ for all $i \neq 1$, and hence $|\psi\rangle$ is a pure state. Reciprocally, if $|\psi\rangle$ is a pure state, only one non-zero Schmidt value exists, $s_1 = 1$ and so $S_{AB} = 0$. While the Schmidt rank r gives information on the level of entanglement of the quantum state, the Von Neumann EE S_{AB} gives information about the underlying distribution of the Schmidt values. For a given rank r , The more S_{AB} is close to $\ln(r)$, the more disordered the random variable \hat{X} is. Figure 1.1 shows some possible distribution of the singular values in the range given by the rank.

1.1.3 Computing the Schmidt values using reduced density matrix formalism

The Von Neuman EE is useful for many purposes since it reflects important universal properties of the physical system. It is obtained by the eigenvalues of the so-called reduced density matrix.

Density matrix. Consider a quantum state $|\psi\rangle \in \mathbb{H}_A \otimes \mathbb{H}_B$. Then the density matrix of that quantum state is defined as an observable on \mathbb{H}_{AB}

$$\hat{\rho}_{AB} = |\psi\rangle\langle\psi| \quad (1.7)$$

The reduced density matrix of A is defined on \mathbb{H}_A as

$$\hat{\rho}_A = \text{Tr}_B[\hat{\rho}_{AB}]. \quad (1.8)$$

Similarly the reduced density matrix of B is defined on \mathbb{H}_B as

$$\hat{\rho}_B = \text{Tr}_A[\hat{\rho}_{AB}]. \quad (1.9)$$

Trace of density matrix. Let $c = \langle \psi | \psi \rangle$ be the norm of $|\psi\rangle \in \mathbb{H}_{AB}$. Then

$$\mathrm{Tr}_A(\hat{\rho}_A) = c, \quad \mathrm{Tr}_B(\hat{\rho}_B) = c, \quad \mathrm{Tr}_{AB}(\hat{\rho}_{AB}) = c \quad (1.10)$$

Proof. In this proof, for ease of notation, the sum over basis element of \mathbb{H}_α is denoted \sum_α , where $\alpha \in \{A, B\}$. By definition :

$$\begin{aligned} \mathrm{Tr}_A(\hat{\rho}_A) &= \sum_a \langle a | \hat{\rho}_A | a \rangle \\ &= \sum_a \langle a | \left(\sum_b \langle b | \psi \rangle \langle \psi | b \rangle \right) | a \rangle \\ &= \sum_a \sum_b \langle a, b | \psi \rangle \langle \psi | a, b \rangle \\ &= \langle \psi | \psi \rangle \\ &= c \end{aligned}$$

The proof of the other relations is similar. \square

Now that we have introduced the definition of the reduced density operator, we next see how to use it to compute the Schmidt values.

Properties 1.1.2. The Schmidt values are the square roots of the eigenvalues of $\hat{\rho}_A$, or $\hat{\rho}_B$.

Proof. Using the Schmidt decomposition (Prop.1.1.1), exists orthonormal sets $\{|a_1\rangle, \dots, |a_m\rangle\} \subset \mathbb{H}_A$ and $\{|b_1\rangle, \dots, |b_m\rangle\} \subset \mathbb{H}_B$ that verify for all $i \in \llbracket 1, m \rrbracket$

$$\langle a_i | \psi \rangle = s_i |a_i\rangle, \quad \langle b_i | \psi \rangle = s_i |b_i\rangle \quad (1.11)$$

These orthonormal sets can be extended to an orthonormal basis of respectively \mathbb{H}_A and \mathbb{H}_B :

$$\{|a_i\rangle\} \rightarrow \{|a_i\rangle\} \cup \{|\tilde{a}_i\rangle\} = \mathbb{H}_A \quad (1.12)$$

$$\{|b_i\rangle\} \rightarrow \{|b_i\rangle\} \cup \{|\tilde{b}_i\rangle\} = \mathbb{H}_B \quad (1.13)$$

and we can compute the reduced density operator with these basis :

$$\hat{\rho}_B = \mathrm{Tr}_A(|\psi\rangle \langle \psi|) = \sum_{i=1}^m \langle a_i | \psi \rangle \langle \psi | a_i \rangle + \sum_i \underbrace{\langle \tilde{a}_i | \psi \rangle \langle \psi | \tilde{a}_i \rangle}_{=0} \quad (1.14)$$

$$\hat{\rho}_A = \mathrm{Tr}_B(|\psi\rangle \langle \psi|) = \sum_{i=1}^m \langle b_i | \psi \rangle \langle \psi | b_i \rangle + \sum_i \underbrace{\langle \tilde{b}_i | \psi \rangle \langle \psi | \tilde{b}_i \rangle}_{=0} \quad (1.15)$$

and hence using equations (1.11), we find

$$\hat{\rho}_B = \sum_{i=1}^m s_i^2 |a_i\rangle \langle a_i| \quad (1.16)$$

$$\hat{\rho}_A = \sum_{i=1}^m s_i^2 |b_i\rangle \langle b_i| \quad (1.17)$$

and hence we see that Schmidt values are exactly eigenvalues of ρ_A and ρ_B . \square

1.1.4 Physical implications

The eigenvalues of the density matrix give the distribution function of basis states in forming a quantum many-body state. If the number of nonzero eigenvalues is large, as many basis states join the quantum state. If these states have equal weight it corresponds to the infinite temperature Gibbs state. The random state seems to be closer to that equal-weight state, its weight distributes randomly so that the entropy is less than the maximum value.

The local density matrix in subsystem A represents the distribution of local basis on A joining the local quantum state. Because each local basis of A is combined with the rest of the system $B \equiv \bar{A}$, the weight is determined after tracing out the degrees of freedom of B. If a certain basis in B is combined with many of the basis states in A, it means that tracing out B will generate a finite weight on all these basis states in A. In that sense, "entanglement" will quantify how much variety the basis sets in two subsystems are related across their boundary. If the entanglement is large, more bases have similar weights and we need a larger number of bases to represent that state, otherwise, we can shrink their number without sacrificing the accuracy. We apply the MPS-based formalism because it has the advantage of describing the quantity of information stored, which we consider to be useful to extract to classify or detect the major properties of the phases of matter.

1.2 Matrix product state

Matrix product states (MPS) are a special class of tensors that are written as products over many rank-3 tensors. We here present a basic introduction to MPS, starting from the definitions of tensors, and show how to efficiently compress the information stored.

1.2.1 Tensor: definitions and diagrammatic representation

Tensors are a generalization of matrices to higher dimensions. A *rank L* tensor is an object that has L indices $T_{x_1 \dots x_L}$, where each index can take several values. The dimension of a *leg* x_i is defined as the number of values it can take. A matrix M_{ij} is a rank 2 tensor, and the dimension of leg i equals the number of rows, and the dimension of leg j equals the number of columns. A vector v_i is a tensor of rank 1. There exists a diagrammatical representation of tensor. The rules to draw these diagrams :

- any tensor is a circle
- tensor of rank n has n lines coming out of it
- connected lines means that the indices are contracted

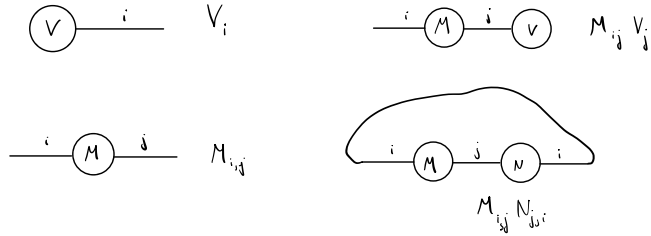


Figure 1.2: Tensor diagrams for tensors of order 1, 2, 3.

The convention is that for matrices, the horizontal left line corresponds to the row index and the horizontal right line to the column index.

1.2.2 Grouping indices

In this work, we will manipulate tensors by changing the number and positions of the leg without changing the information content stored in the tensor. This is allowed by the following proposition

Properties 1.2.1. There is an isomorphism between the space of all tensors of rank L_1 with leg dimensions $a_1 \times a_2 \cdots a_{L_1}$ and between the space of all tensors of rank $b_1 \times b_2 \cdots b_{L_2}$, if and only if

$$\prod_{i=1}^{L_1} a_i = \prod_{i=1}^{L_2} b_i \quad (1.18)$$

This property allows a lot of flexibility in manipulating tensors. For example, consider a vector v_i of size d^L , then we can see this vector as a rank L tensor where each leg has dimension d :

$$v_i = T_{x_1 \dots x_L} = T_{f(i)}$$

where f is a bijective mapping between the position in the vector and the set of indices of the tensor T . This manipulation is called grouping because diagrammatically it consists of grouping legs.

As another example, consider the tensor $T_{x_1 \dots x_L}$, and regroup the indices into two, $x_1 \dots x_i$ and the remaining indices $x_{i+1} \dots x_L$. Then the obtained tensor is a matrix $M_{x_1 \dots x_i, x_{i+1} \dots x_L} \in \mathbb{R}^{d^i \times d^{L-i}}$. We can then reshape this matrix in a matrix of size $\mathbb{R}^{d^{i+1} \times d^{L-i-1}}$, which consists in moving one leg from the right to the left. These operations are summarized in Fig.1.3.

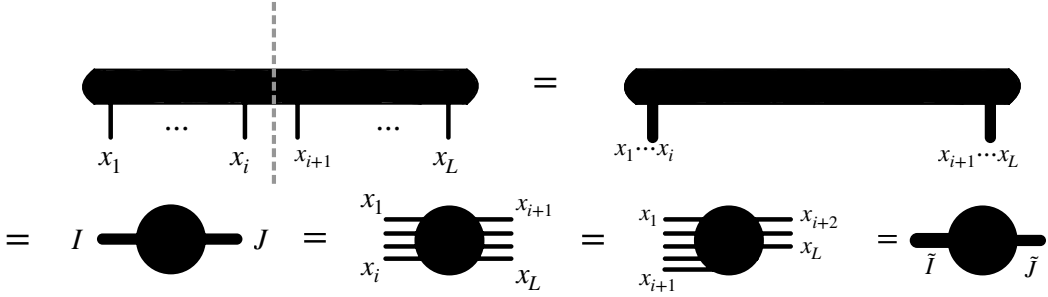


Figure 1.3

The last manipulation on the tensor is called slicing. Consider a matrix $M_{ab,c} \in \mathbb{R}^{n_a n_b \times n_c}$. Then we can slice this matrix, row-wise, into n_a matrix $M_{b,c}^a$ of size $n_b \times n_c$, and see the result as a vector a matrices $v_a = M_{b,c}^a$:

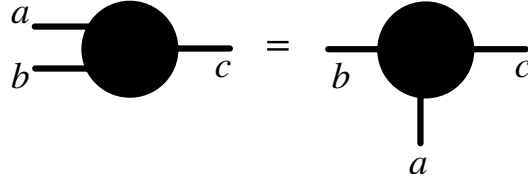


Figure 1.4: Diagrammatic representation of slicing.

1.2.3 Singular value decomposition theorem

The singular value decomposition (SVD) is a factorization of a matrix of the form $M = USV^\dagger$. The SVD is always possible and the eigenvalues $\text{Diag}(S)$ are uniquely determined. These values characterize the quantum state in the MPS formalism. Here, we show the proof to support the Schmidt decomposition we introduced earlier.

Theorem 1.2.1. *Consider an arbitrary matrix $M \in \mathbb{C}^{n_A \times n_B}$, where n_A and n_B are non zero integers. Let us call $m = \min(n_A, n_B)$. Then :*

1. Exists a matrix $U \in \mathbb{C}^{n_A \times m}$ with orthonormal columns $U^\dagger U = 1_{n_A}$, called the left singular vectors.
2. $S \in \mathbb{C}^{m \times m}$ such that $S = \text{Diag}(\dots, S_{aa}, \dots)$ and one usually uses the notation $S_{aa} = s_a$. The scalars s_a are called the singular values of the matrix M .
3. $V^\dagger \in \mathbb{C}^{m \times n_B}$ that has orthonormal rows called the right singular vectors, i.e $V V^\dagger = 1_{n_B}$.

such that

$$M = USV^\dagger. \quad (1.19)$$

The equation (1.19) is called the singular value decomposition of the matrix M . We will always choose the base change such that $s_1 \geq s_2 \geq \dots \geq s_i > \dots > 0$. A diagram that illustrates the SVD decomposition is presented at Figure 1.5.

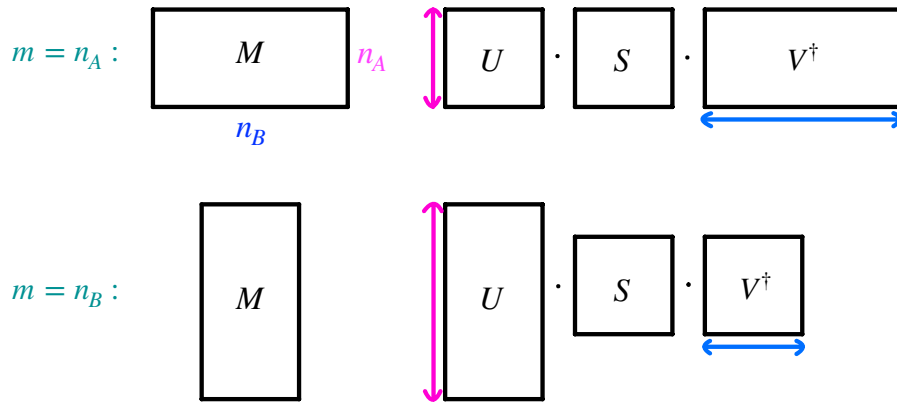


Figure 1.5: Illustration of the shape of the matrices appearing in the SVD decomposition of an arbitrary matrix $M \in \mathbb{C}^{n_A \times n_B}$.

Now with that theorem, we can prove the Schmidt decomposition theorem 1.1.1 as follows;

Proof. Decomposing the state $|\psi\rangle \in \mathbb{H}_A \otimes \mathbb{H}_B$ in an orthonormal basis

$$|\psi\rangle = \sum_{i,j} \psi_{ij} |i_A\rangle |j_B\rangle. \quad (1.20)$$

Applying the SVD decomposition theorem 1.2.1 on the matrix $\psi_{ij} \in \mathbb{R}^{n_A \times n_B}$ yields,

$$|\psi\rangle = \sum_{i,j} \sum_{k=1}^{\min(n_A, n_B)} U_{ik} S_{kk} V_{kj}^\dagger |i_A\rangle |j_B\rangle. \quad (1.21)$$

Calling $m = \min(n_A, n_B)$ and changing the order of summation, we find,

$$|\psi\rangle = \sum_{k=1}^m \underbrace{\left(\sum_i U_{ik} |i_A\rangle \right)}_{=:|a_k\rangle} S_{kk} \underbrace{\left(\sum_j V_{jk}^* |j_B\rangle \right)}_{=:|b_k\rangle}. \quad (1.22)$$

□

1.2.4 MPS representation

To obtain the MPS representation of the quantum state, we want to factorize any given rank L tensor into the product of matrices, as such tensor represents the coefficients of superpositions of basis states in forming a quantum state. We thus show the proof of the following theorem. In this work, tensor will have real valued data.

Theorem 1.2.2. *Any rank L tensor ψ with leg dimensions d can be written exactly as a product of matrices*

$$\psi_{x_1, \dots, x_L} = A^{x_1} \cdots A^{x_L} \quad (1.23)$$

where

- $x_1, \dots, x_L \in \llbracket 0, d - 1 \rrbracket$ are called the physical indices
- $A^{x_i} \in \mathbb{R}^{m_{i-1}, m_i}$ for all $x_i \in \llbracket 0, d - 1 \rrbracket$
- $m_0 = m_L = 1$ for the outermost (dummy) bonds.

To demonstrate this theorem, we give an algorithm that, starting from the tensor, builds the matrices of the right-hand side.

Proof. Let us suppose that the $\psi_{x_1 \dots x_L}$ is a row vector in \mathbb{R}^{d^L} . Then, we do the following :

1. Reshape the row vector $\psi_{x_1 \dots x_L}$ of size d^L into a matrix $\psi_{x_1, (x_2 \dots x_L)}$ of size $d \times d^{L-1}$.
2. Then find SVD decomposition of $\psi_{x_1, x_2 \dots x_L}$: $\psi = U S V^\dagger$

$$\psi_{x_1, x_2 \dots x_L} = \sum_{a_1=1}^{m_1} U_{x_1, a_1} S_{a_1, a_1} V_{a_1, x_2 \dots x_L}^\dagger \quad (1.24)$$

and $m_1 = \min(d, d^{L-1})$.

3. Row-wise slice matrix U into d -matrices A^{x_1} of size $1 \times m_1$.

This first step gives the first set of matrices A^{x_1} at the first site, and diagrammatically, can be represented like :

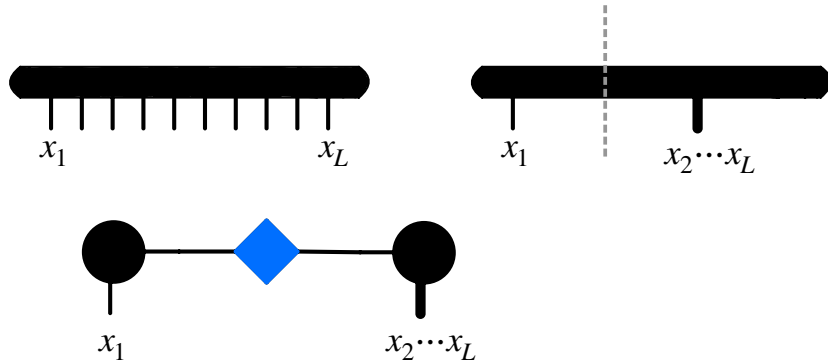


Figure 1.6: First step of the construction to the MPS form of a tensor of rank L . It consists in writing a row vector of L indices into a product of three matrices, by first reshaping the row vector into a matrix (indicated by a dashed line) and then writing this matrix as a product of 3 matrices, using its SVD decomposition.

Precisely, given the matrices $S \in \mathbb{R}^{m_i \times m_i}$ and $V^\dagger \in \mathbb{R}^{m_i \times d^{L-i}}$ obtained at last step, we do the following :

1. Reshape SV^\dagger into a matrix of size $m_id \times d^{L-i-1}$ and call this matrix our new ψ .
2. Find SVD decomposition of this new $\psi = USV^\dagger$ where $U \in \mathbb{R}^{m_id \times m_{i+1}}$, $S \in \mathbb{R}^{m_{i+1} \times m_{i+1}}$ and $V^\dagger \in \mathbb{R}^{m_{i+1} \times d^{L-1-i}}$ with $m_{i+1} = \min(m_id, d^{L-1-i})$.
3. Row-wise slice the matrix U into d matrices $A^{x_{i+1}}$ of size $m_i \times m_{i+1}$.

We see that the construction of the MPS simply consists in reshaping and slicing matrices recursively :

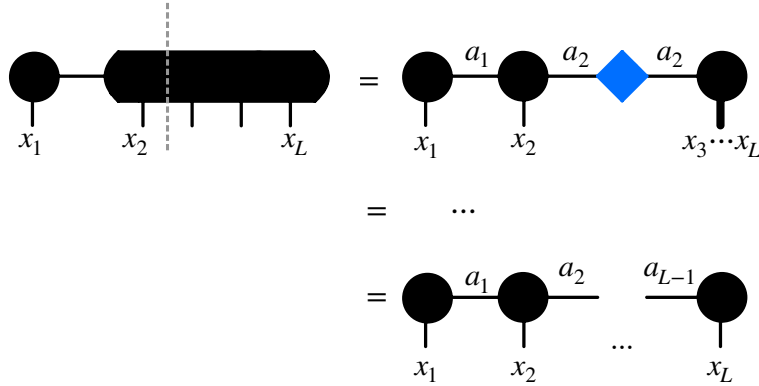


Figure 1.7: Further steps of construction of MPS representation.

□

For now on, we will call the process presented in the previous proof the *MPS procedure*.

1.2.5 Bond dimension and truncation

The theorem 1.2.2 tells us that one can write any rank L tensor as a product of matrices A^{x_i} :

$$\psi_{x_1 \dots x_L} = \sum_{a_1, \dots, a_{L-1}} A_{1,a_1}^{x_1} A_{a_1,a_2}^{x_2} \cdots A_{a_{L-1},1}^{x_L}$$

For a given value of physical indices, the result is a product of matrices. The leg jointing two matrices is called *bond*, and its dimension is called *bond dimension*. The leg jointing matrix A^{x_i} and $A^{x_{i+1}}$ has dimension m_i .

During the construction of the MPS form of a tensor, we successively performed the SVD decomposition. Figure 1.8 represents the MPS representation of the tensor where the singular value matrices are explicitly appearing, and represented as blue squares.



Figure 1.8: MPS representation of a tensor of rank L . The blue rotated square represents a singular value matrix.

Consider a given singular value matrix between site i and site $i + 1$: $S = \text{Diag}(s_1, \dots, s_{m_i})$. Then, for some systems, a lot of singular values are small, and truncating them does not cause too much loss of information. The low-rank approximation theorem tells us that for an arbitrary matrix M of rank r , the best approximation among all the matrices with rank $r' < r$ is obtained by taking the SVD of M and keeping only the r' first singular values[1].

Therefore, let us introduce a truncation parameter $\epsilon > 0$ and define $a_\epsilon = \#\{s_i \mid s_i > \epsilon\}$ as the number of singular values that are greater than this threshold parameter, and $k \in \{2, 3, \dots\}$ as another truncation parameter, that will determine the maximum bond dimension. The *truncation procedure* that takes place each time we do an SVD is:

If $k \leq a_\epsilon$, we truncate the matrices U, S, V in the following way :

$$U \rightarrow U_k \in \mathbb{R}^{n,k}, \quad S \rightarrow S_k \in \mathbb{R}^{k,k}, \quad V^\dagger \rightarrow V_k^\dagger \in \mathbb{R}^{k,m}$$

where $n \times m$ is the dimension of the original matrix, equal to USV^\dagger .

Else if $k > a_\epsilon$, we truncate like this :

$$U \rightarrow U_\epsilon \in \mathbb{R}^{n,a_\epsilon}, \quad S \rightarrow S_k \in \mathbb{R}^{a_\epsilon,\epsilon}, \quad V^\dagger \rightarrow V_\epsilon^\dagger \in \mathbb{R}^{a_\epsilon,m}.$$

For a given SVD decomposition between site i and site $i + 1$, we have a bond dimension m_i and a Schmidt rank r_i , and after the truncation, the value of r_i will become $\min(a_\epsilon, k) = r(\epsilon, k)$.

The *truncation error* induced by truncating with (k, ϵ) on the tensor $\psi_{x_1 \dots x_L}$ is,

$$e_\psi(k, \epsilon) := \frac{|\psi - \tilde{\psi}(k, \epsilon)|}{|\psi|}, \quad (1.25)$$

with $\tilde{\psi}(k, \epsilon)$ the result of MPS after the truncation procedure. The norm is the usual Euclidean norm.

1.2.6 Entanglement entropy in the context of MPS

The EE of a quantum state living in a bipartite Hilbert space is fully determined by the Schmidt values and we have seen that one way to have them is to compute the eigenvalues of the reduced density matrix. However, if one has the MPS representation of that state, one has easy access to the EE for any bipartition of the Hilbert space.

More precisely, consider a many body quantum state $|\psi\rangle \in \mathbb{H} = \otimes_{i=1}^L \mathbb{H}_{x_i}$ where each space \mathbb{H}_{x_i} has finite dimension d . Then the coefficients $\psi_{x_1 \dots x_L}$ of that state form a vector of size d^L , and the MPS procedure can be applied to that vector. Let us denote S_i the Von Neumann EE of $|\psi\rangle$ for a bipartition $\mathbb{H}_A = \otimes_{j=1}^i \mathbb{H}_{x_j}$ and $\mathbb{H}_B = \otimes_{j=i+1}^L \mathbb{H}_{x_j}$.

Properties 1.2.2. The value of S_i is fully determined by the singular values $\{s_1, \dots, s_{r_i}\}$ appearing at bond joining site i and $i + 1$ during the MPS procedure :

$$S_i = - \sum_{a=1}^{r_i} s_a^2 \log(s_a^2) \quad (1.26)$$

In other words, the nonzero singular values appearing at bond from site i to $i + 1$ are the Schmidt values of the state $|\psi\rangle$ living in the Hilbert space bipartite between the left sites $1, \dots, i$ and the right sites $i + 1, \dots, L$.

If some truncation is made, then $S_i(\epsilon, k) = - \sum_{a=1}^{r_i(\epsilon, k)} s_a^2 \log(s_a^2)$ will start to differ from the non truncated one $S_i(0, +\infty)$.

1.2.7 Application on random data

To clarify the meaning of the truncation, we apply the MPS procedure on a vector $\psi_{x_1 \dots x_L} \sim U(0, 1)$ with random entries, of size $d^L = 2^9$. Figure 1.9 shows the set of singular values $\{s_i\}$ at each bond, and the value of the truncation parameter ϵ , represented as a dashed line, for two values of compression. One notices that the Schmidt rank at all sites is nonzero ; it is represented by the blue curve in Fig. 1.10a. This Schmidt rank grows up to bond 4 and then decays and has a perfectly symmetric curve. However, as one compresses, the bond dimension curve loses this shape as shown in the blue line in Fig. 1.10b. We observe that as we compress, the equality (1.1.1) is violated.

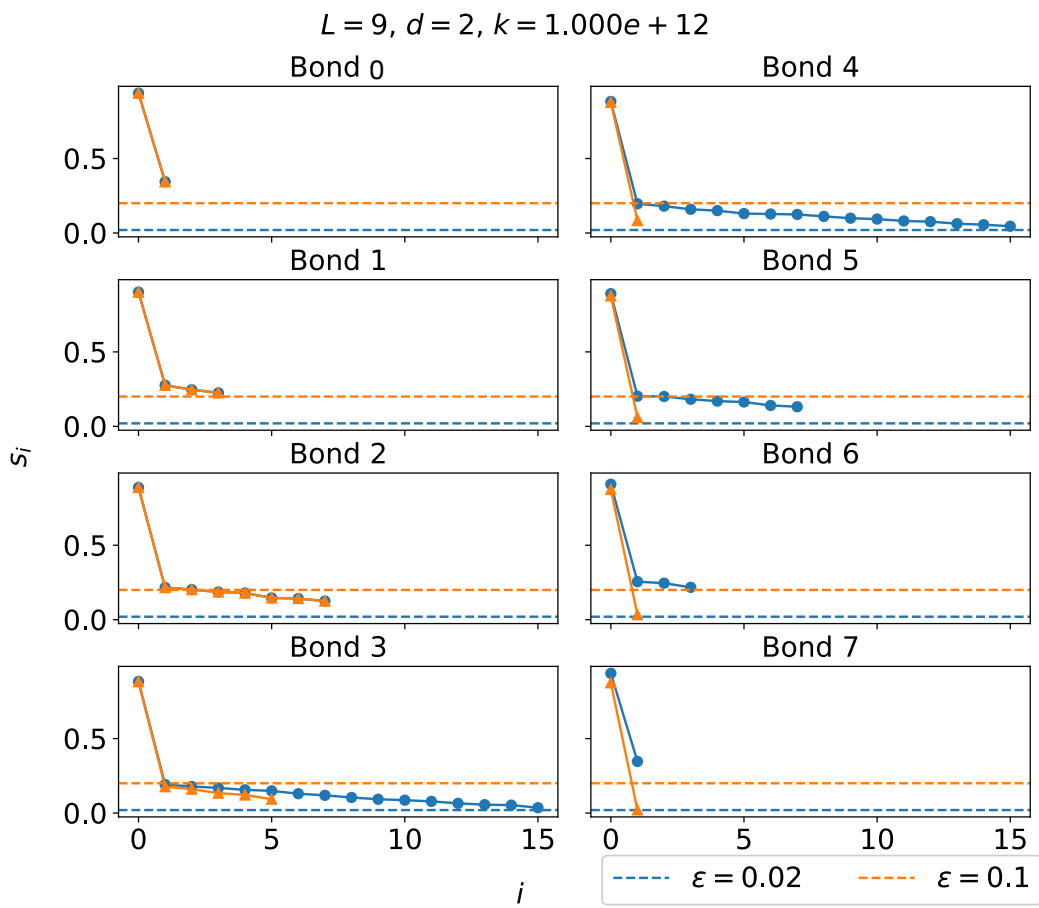
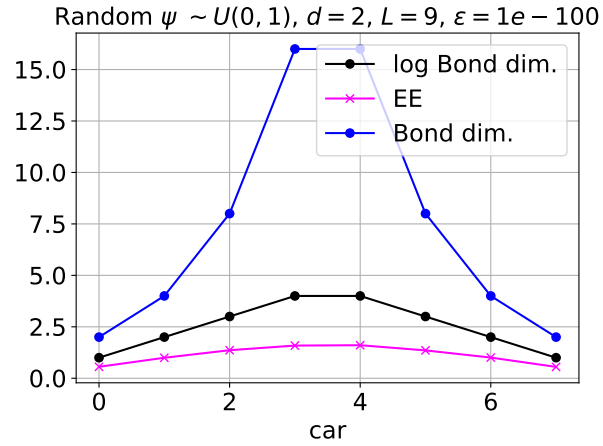
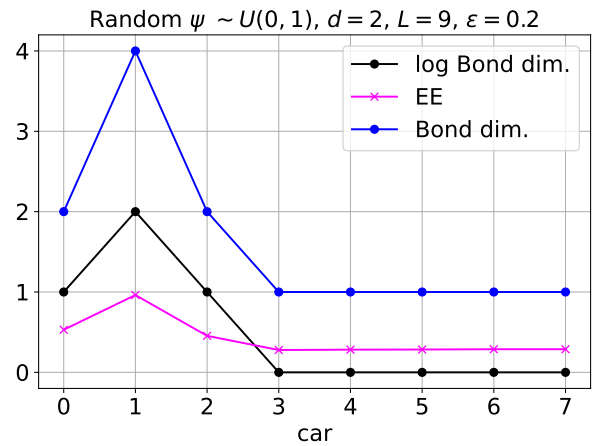


Figure 1.9: Singular values at each bond for uniformly distributed data, when there is no truncation.



(a) No truncation.



(b) Finite truncation.

Figure 1.10: Bond dimension, upper bond of the EE (log Bond dim.) and EE for uniformly distributed data for different truncation parameters. The log is taken to be base 2 because numerically the EE is computed with base 2.

1.3 Phases of matter of interest

In this thesis, we consider two characteristic phases; one is the 2D Ising model which undergoes a second-order phase transition at finite temperature to the magnetically ordered phase. The other is the Heisenberg Edwards-Anderson model in a 3D discrete lattice ; in this model, a quenched bond disorder is present and the system is believed to have a thermodynamic phase transition to a spin glass phase (and also the chiral glass phase) at finite temperature[2]. However, unlike the usual phase transition like the 2D Ising model, the spin glass phase lacks a local order parameter. Indeed, the magnetic susceptibility does not show any divergence but shows a cusp, while instead, the nonlinear susceptibility (at higher order) diverges at the transition. The question is, whether this kind of phase transition can be discriminated as a development of particular (possibly not a local but a global) structure of spins?

1.3.1 2D classical Ising model

The 2D ferromagnetic Ising model with zero magnetic field is defined by the Hamiltonian

$$\mathcal{H} = -J \sum_{\langle i,j \rangle} S_i S_j \quad (1.27)$$

where $S_i = \pm 1$ is the Ising variable, N is the number of spins, $J > 0$ the coupling between spins taken to be $J = 1$ in this thesis, and $\langle i, j \rangle$ a pair of nearest neighbour spins. The exact solution of this model was derived by Onsager in 1944 [3] using a transfer matrix method. It shows that the thermal average of the total magnetization $m(T) = \langle \sum_{i=1}^N S_i \rangle$, has a discontinuity in its derivative with respect to T at the critical temperature $T_c k_B / J = 2 / \ln(1 + \sqrt{2}) \approx 2.269$. There are several other approaches to finding the exact solutions after Onsager, which we do not go into here [4, 5, 6, 7, 8, 9, 10].

Table 1.1: Behavior of physical properties in the 2D ferromagnetic Ising model. The quantity d is the dimension of the space, $d = 2$ for the 2D Ising model. The exponents η, ν, α are called the critical exponent, and their values for the 2D Ising model are respectively $1/4, 1, 0$.

T	$< T_c$	$\approx T_c$	$> T_c$
$m(T)$	finite	2nd order PT	$= 0$
phase	ferromagnetic	critical	paramagnetic
G_{ij}	slow decay	$r_{ij}^{-d+2-\eta}$	$e^{-r_{ij}/\xi(T)}$
macr. order	yes	yes	no
$\xi(T)$	∞	$ T - T_c ^{-\nu}$	lattice spacing
C_h		$ T - T_c ^{-\alpha}$	

We now summarize the basic features of the model in Table 1.1. The correlation function between spins at sites i and j is defined as $G_{ij} = \langle S_i S_j \rangle - \langle S_i \rangle \langle S_j \rangle$. At a zero magnetic field, the system is translational invariant, and hence G_{ij} only depends on the distance between sites i and j . Let \mathbf{r}_i be the position of a spin. If $\lim_{|\mathbf{r}_i - \mathbf{r}_j| \rightarrow \infty} G_{ij} \neq 0$, the system has a magnetic long-range order, and if G_{ij} decays in power law with distance, $|\mathbf{r}_i - \mathbf{r}_j|$, the system is critical. One universal aspect of the second-order phase transition, symptomatic of critical phenomena near T_c , is that the correlation at all length scales and the scale invariance are present. When $T < T_c$, all spin are correlated and G_{ij} quickly extrapolates to a finite value, namely the correlation length is infinite. Whereas at

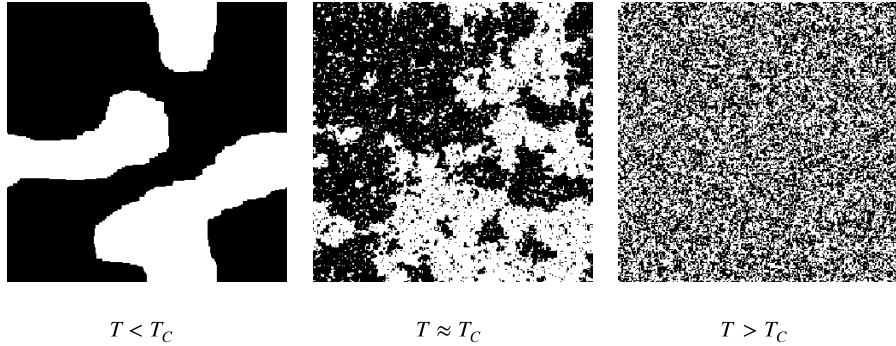


Figure 1.11: Snapshots of the ferromagnetic Ising model with zero magnetic field (1.27), at different temperatures.

high temperatures, each spin behaves almost randomly independently with the other, so that G_{ij} exhibits an exponential decay, where the correlation length is given by the lattice spacing. Figure 1.11 presents three snapshots of the thermal equilibrium states of the model in Eq.(1.27), obtained by the classical Monte Carlo method [11]. We see that at low temperatures, several big islands of spins are present, and inside these islands, almost all spins point in the same direction. Near critical temperature, several big islands are present but even inside them, there are numerous smaller islands, indicating that the fluctuations are present. At high temperatures, the snapshot looks completely random. The distribution of these islands have been studied using Monte Carlo simulations, and it is believed that they are fractals [12] and that the large clusters have scaling properties. Whether or not we can detect the criticality phenomena quantitatively by our framework is one of the issues we discuss in Section 3.3.

1.3.2 Spin glasses

Introduction - a quenched disorder in glasses

In a crystal, atoms are arranged periodically, while in a glass, this is not the case. A thermal disorder refers to the agitation of spins (large fluctuation) when temperature is increased, whereas the glasses are the *frozen* disordered configuration of atoms or spins. In order to study these types of phases, it is often required to include the explicit randomness to the model, which is called *quenched disorder*. In the same context as the magnetic moment induced by the magnetic field is not the intrinsic order, the positional disorder induced by the quenched randomness of the site-potential on atoms or the orientational disorder of spins induced by the field randomness is not the intrinsic glass ordering. For a structural glass, the model without quenched disorder, while with the relatively long interactions are known to exhibit glassy behavior, but whether there is a thermodynamic glass transition in one to three spatial dimensions is not clarified yet. In lattice spin models for spin glass, the quenched randomness is introduced as the randomness in the interactions J_{ij} between spins and is called the Edwards-Anderson model.

Quenched hamiltonian

The Edwards-Anderson model [13] includes only the random bond interactions J_{ij} which average to zero. Consider the Ising Edwards-Anderson Hamiltonian :

$$H = - \sum_{\langle i,j \rangle} J_{ij} S_i S_j \quad (1.28)$$

where $\{J_{ij}\} = \mathbf{J}$ is the set of bond interactions as random variables that are iid. Usually, the chosen distribution $P(J_{ij})$ is a Gaussian

$$P(J_{ij}) = \frac{1}{\sqrt{2\pi\sigma^2}} e^{-\frac{(J_{ij}-J_0)^2}{2\sigma^2}}$$

with a variance σ^2 and a mean value $J_0 = 0$. There are two probability spaces associated with the model; One is the micro-states $\{\omega\} = \Omega$ spanned by spin configurations and the other is for bond configurations. In this setting, the thermodynamic potential is averaged over the micro-states and over the support of \mathbf{J} . The quenched Hamiltonian (1.28) is thus a function of two species of random variables $H = H(\{S_i\}, \mathbf{J})$.

The free energy is related to the partition function (we take $k_B = 1$) as

$$F_T = -T \ln(Z_T), \quad (1.29)$$

but this free energy is random since

$$Z = \sum_{S_1, \dots, S_N} e^{-\beta H(S_1, \dots, S_N, \mathbf{J})}$$

is a function of \mathbf{J} , where needs to average over the quenched variable. This is called *configurational average* taken as

$$[F_T] = \int_{S_J} d\mathbf{J} P(\mathbf{J}) F_T(\mathbf{J}) = -T \int_{S_J} d\mathbf{J} P(\mathbf{J}) \ln(Z_T(\mathbf{J})), \quad (1.30)$$

where S_J is the support of \mathbf{J} .

The free energy has a so-called *self-averaging* quantity, meaning that in the thermodynamic limit, it converges to a defined function independent of \mathbf{J} [14]

$$F_T(\mathbf{J}) \sim F_T^\infty. \quad (1.31)$$

Quenched averaging on both sides yields

$$[F_T] = F_T^\infty, \quad (1.32)$$

or more precisely, we can prove that

$$[F_T^2] - [F_T]^2 = \mathcal{O}\left(\frac{1}{N}\right). \quad (1.33)$$

Replica method

To obtain the thermodynamic properties of a quenched disorder system, one needs to compute the logarithm of the partition function, and then take the configurational average of it. However, computing $[\ln(Z_T)]$ can be too difficult. There is a treatment called the *replica method* that allows to compute it using the following algorithm :

1. Consider n independent copies (non-interacting) of the original system, where all copies have the same quenched variable \mathbf{J} . The hamiltonian of the total system made of the n replicas is

$$H = \sum_{\gamma=1}^n H_\gamma, \quad H_\gamma = H_\gamma(\{S_i^\gamma\}, \mathbf{J}). \quad (1.34)$$

The partition function of the total system is

$$\begin{aligned} Z_T(\mathbf{J}) &= \sum_{\mathbf{S}^1, \dots, \mathbf{S}^n} \exp \left(-\beta \sum_{\gamma=1}^n H_\gamma(\mathbf{S}^\gamma, \mathbf{J}) \right) \\ &= \sum_{\mathbf{S}^1, \dots, \mathbf{S}^n} \prod_{\gamma=1}^n \exp(-\beta H_\gamma(\mathbf{S}^\gamma, \mathbf{J})) \\ &= \sum_{\mathbf{S}^1} e^{-\beta H_1(\mathbf{S}^1, \mathbf{J})} \dots \sum_{\mathbf{S}^n} e^{-\beta H_n(\mathbf{S}^n, \mathbf{J})} \\ &= \prod_{\gamma=1}^n z_T(\mathbf{J}) = (z_T(\mathbf{J}))^n \end{aligned}$$

where z_T is the one-replica partition function. Hence

$$[Z_T(\mathbf{J})] = [z_T(\mathbf{J})]^n. \quad (1.35)$$

2. Use the following identity (without proof) :

$$[\ln z_T(\mathbf{J})] = \lim_{n \rightarrow 0} \frac{[z_T(\mathbf{J})]^n - 1}{n} \quad (1.36)$$

that tells us that to compute the one-replica free energy, it suffises to compute the partition function of the n -replica system, and take the $n \rightarrow 0$ limit. The one-replica free energy is

$$F_T(\mathbf{J}) = -T \ln z_T(\mathbf{J}) \Rightarrow [F_T(\mathbf{J})] = -\lim_{n \rightarrow 0} T \left(\frac{[z_T(\mathbf{J})]^n - 1}{n} \right). \quad (1.37)$$

Sherrington-Kirkpatrick model (SK model)

Let us apply the replica method described in the preceding section to the so-called *Sherrington-Kirkpatrick model*, which is described as a paradigmatic example of mean-field spin-glass,

$$H(\mathbf{J}, \{S_i\}) = - \sum_{i < j} J_{ij} S_i S_j - h \sum_{i \in V} S_i^\gamma. \quad (1.38)$$

This model is a fully connected model, meaning that each spin interacts with all the other spins. The n -replica partition function is

$$[Z_T] = \int \left(\prod_{i < j} dJ_{ij} P(J_{ij}) \right) \sum_{\{\sigma\}} \exp \left(\beta \sum_a \sum_{<i,j>} J_{ij} \sigma_i^a \sigma_j^b + \beta h \sum_a \sum_i \sigma_i^a \right), \quad (1.39)$$

where

$$\sum_{\{\sigma\}} = \sum_{\sigma^1} \cdots \sum_{\sigma^n}, \quad \sum_a \text{ sum over replicas .} \quad (1.40)$$

We can show, by means of Gaussian integrals [15] that

$$[Z_T] = \sum_{\{\sigma\}} \exp \left(\beta h \sum_i \sum_a \sigma_i^a \right) \exp \left(\frac{\beta^2}{4} (Nn - n^2) \right) \prod_{a < b} \exp \left(\frac{\beta^2}{2N} \left(\sum_i \sigma_i^a \sigma_i^b \right)^2 \right), \quad (1.41)$$

where N is the number of spins. Using

$$\sqrt{\frac{A}{\pi}} \int dx e^{-Ax^2+Bx} = e^{\frac{B^2}{4A}}, \quad (1.42)$$

with

$$A = \frac{N\beta^2}{2}, \quad B = \beta^2 \left(\sum_i \sigma_i^a \sigma_i^b \right), \quad (1.43)$$

to express $\exp \left(\frac{\beta^2}{2N} \left(\sum_i \sigma_i^a \sigma_i^b \right)^2 \right)$ as a gaussian integral¹, we obtain the following expression for the partition function

$$[Z_T] = \sum_{\{\sigma\}} \exp \left(\beta h \sum_i \sum_a \sigma_i^a \right) \exp \left(\frac{\beta^2}{4} (Nn - n^2) \right) \prod_{a < b} \mathcal{N}(N, \beta) \int dx e^{-\frac{N\beta^2}{2} x^2 + x \beta^2 \sum_i \sigma_i^a \sigma_i^b} \quad (1.44)$$

For each pair a, b of the product, there is an integration over x , so let us rename these integrated variables Q_{ab} :

$$[Z_T] = \sum_{\{\sigma\}} \exp \left(\beta h \sum_i \sum_a \sigma_i^a \right) \exp \left(\frac{\beta^2}{4} (Nn - n^2) \right) \prod_{a < b} \int dQ_{ab} e^{-\frac{N\beta^2}{2} Q_{ab}^2 + Q_{ab} \beta^2 \sum_i \sigma_i^a \sigma_i^b}. \quad (1.45)$$

In the limit $N \rightarrow \infty$, we will make a saddle point calculation and discard all terms that are not exponential in N and retain only terms exponential in n :

$$[Z_T] \propto \int dQ e^{-N\mathcal{S}[Q, h]}, \quad (1.46)$$

where

$$\mathcal{S}[Q, h] := -\frac{\beta^2 n}{4} + \frac{\beta^2}{2} \sum_{a < b} Q_{ab} - \mathcal{W}[Q], \quad (1.47)$$

$$\mathcal{W}[Q] := \ln \sum_{\sigma^1 \in \{-1, 1\}} \cdots \sum_{\sigma^n \in \{-1, 1\}} \exp \left(\beta h \sum_a \sigma^a + \beta^2 \sum_{a < b} \sigma^a \sigma^b Q_{ab} \right), \quad (1.48)$$

¹this operation is called a *Hubbard-Stratanovich* transformation.

and the free energy density is

$$f(\beta, h) = \lim_{n \rightarrow 0} \lim_{N \rightarrow \infty} \left(-\frac{1}{\beta N n} \ln [Z_T] \right) = \lim_{n \rightarrow 0} \frac{1}{\beta n} \text{extr}_Q S[Q, h], \quad (1.49)$$

So, the replica method tells us that to compute the free energy density, one has to find a matrix $Q_{ab} \in \mathbb{R}^{n \times n}$ that extremizes the action. The matrix element Q_{ab} is related to the overlap between the two replicas a and b defined as $\frac{1}{N} \sum_{i=1}^N \langle \sigma_i^a \sigma_i^b \rangle$ [16].

We can first assume that the solution Q^* is totally symmetric, meaning that for any permutation π over n symbols, we have

$$\{Q_{ab}^*\} = \{Q_{\pi(a)\pi(b)}^*\}. \quad (1.50)$$

The only matrix verifying this property is

$$A = \begin{bmatrix} 0 & q & q & \cdots & q \\ q & 0 & q & \cdots & q \\ q & q & 0 & \cdots & q \\ \vdots & \vdots & \vdots & \ddots & \vdots \\ q & q & q & \cdots & 0 \end{bmatrix}.$$

In this case, the action depends only on two parameters $\mathcal{S} = \mathcal{S}[q, h]$ and the externalisation becomes

$$\frac{\partial \mathcal{S}[q, h]}{\partial q} = 0. \quad (1.51)$$

By using (1.48) and (1.49) we can show that this implies

$$q = \int \frac{dz}{\sqrt{2\pi}} e^{-\frac{z^2}{2}} \tanh(\beta h + \beta \sqrt{q} z), \quad (1.52)$$

which is the state equation for q . This equation for $h = 0$ is such that

- it has a unique solution $q = 0$ for $\beta < \beta_c := 1$,
- it has another solution $q \neq 0$ for $\beta > \beta_c$.

Therefore, it seems that for $h = 0$, there is a phase transition at $\beta_c = 1$. However, this solution called the *replica symmetric* (RS) solution has negative entropy at zero temperature. Actually, an analysis of the Hessian matrix

$$\frac{\partial^2 \mathcal{W}}{\partial Q_{ab} \partial Q_{cd}} =: M_{ab,cd} \in \mathbb{R}^{\frac{n(n-1)}{2} \times \frac{n(n-1)}{2}}, \quad (1.53)$$

reveals that the RS solution is only stable above the so-called Almeida-Thouless (dAT) line in the (h, T) phase space. We say that the replica symmetry is broken at this line. The solution below this line was derived by Parisi, and is called the *replica-symmetry breaking* [14] solution. We will very briefly present the construction for the solution in the next section. Physically, the spin-glass phase appears when the RS solution is not stable anymore at low temperatures.

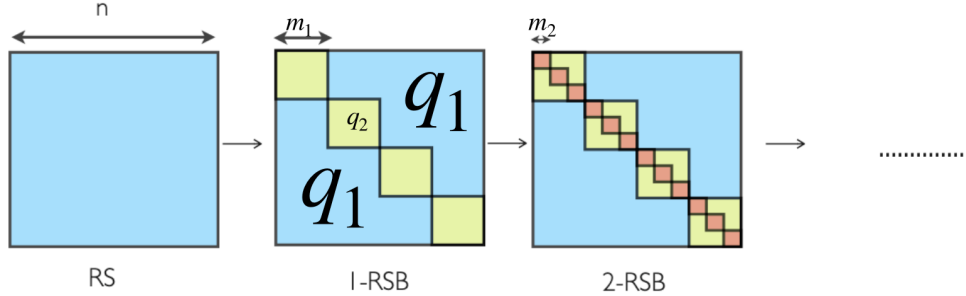


Figure 1.12: Iterative construction of the RSB solution. Figure taken from Ref.[15].

Breaking replica symmetry

The construction of this solution is an iterative procedure. First, order the replica in $\frac{n}{m_1}$ groups of $m_1 \leq n$ replica each. Then define Q_{ab} such that if replica a and b are in the same group, then $Q_{ab} = q_2$, otherwise $Q_{ab} = q_1$. This matrix constitutes the 1-RSB solution. The 2-RSB solution is built by regrouping in each already existing sub-group of replica, m_1/m_2 groups of m_2 replica, and inside these new subgroups, $Q_{ab} = q_3$ (see Fig. 1.12).

The k -RSB solution depends on several parameters

$$Q_{ab} = Q_{ab}(q_1, \dots, q_{k+1}, m_1, \dots, m_k), \quad n \geq m_1 \geq m_2 \geq \dots \geq 1 \quad (1.54)$$

Depending on the specific choices of the Hamiltonian, the RSB of different values of k [16] can take place. The $k \rightarrow +\infty$ limit is called the full-RSB solution, and in this case the matrix Q_{ab} is parameterized by a continuous function $q(x)$, $x \in [0, 1]$. By the symmetry property (1.50), if there exists a particular solution for Q_{ab} with a RSB structure, then any other matrix obtained via a permutation of the replica indices in Q_{ab} is also a solution. All these states are stabilized in the thermodynamic limit. In the full-RSB scenario, the distribution $P(q)$ is continuous over a finite range p .

The Heisenberg Edwards-Anderson model

The model we will study in this thesis with quenched disorder is defined by the Heisenberg Hamiltonian

$$H = - \sum_{\langle i,j \rangle} J_{ij} \mathbf{S}_i \cdot \mathbf{S}_j \quad (1.55)$$

where $J_{ij} \sim \mathcal{N}(0, J^2)$, with the sum $\langle i,j \rangle$ runs over nearest neighbors. We use the classical vector spins $\mathbf{S}_i = (S_{ix}, S_{iy}, S_{iz})$ of size $|\mathbf{S}_i| = 1$, and number of spins is $N = L(L-1)^2$ with L the linear size of the system.

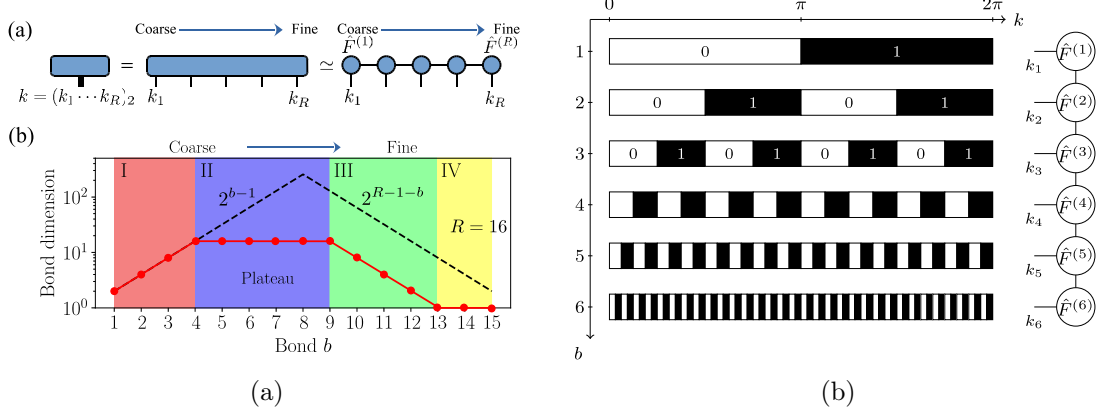


Figure 1.13: (a) MPS representation of the function $f(k)$, where legs represent the scales. As we move from left to right, we go from coarser to finer scales. (b) Illustration of the base-2 representation of the wave vector k . The matrices $\hat{F}^{(i)}$ are the one appearing in the MPS of $f(k_1, \dots, k_L)$. Figures are taken from Ref.[17].

1.4 Analyzing snapshots of phases

In our work, we want to use the snapshots of thermal equilibrium states obtained by the classical Monte Carlo calculation to detect particular phases of matter. We will explain in the next Chapter that these snapshots will be expressed at a multi-leg tensor through a scale separation of the coordinates, and then expressed as a MPS, allowing EE and bond dimension analysis.

In this section, we will review some previous inspiring papers related to our study. In Section 1.4.1, the tensor train method is presented in Refs. [17],[18] is briefly explained. They apply the particular construction of multi-leg tensor to analyze the Green's function and other physical quantities. In Section 1.4.2, we introduce a prior work that uses the same tensor train construction for image compression, which is not related to Refs. [17],[18] or discussed together so far. Finally in 1.4.3, a different way of analysis of the 2D Ising model (1.27) using SVD on the snapshot data is shown.

1.4.1 Scale decomposition and MPS construction

Motivated by the curse of dimensionality in computing for example correlation functions of quantum systems, Shinaoka, *et.al.*[17, 18] developed a method to represent the high-dimensional functions as an MPS where each leg is an auxiliary bit, representing exponentially different length scales in space-time. For example, for a function $f(k) : [0, 2\pi] \rightarrow \mathbb{R}$ in momentum space, the construction works in the following way: let (k_1, k_2, \dots, k_R) be the base-2 digit of k with R being the number of distinct scales, then $f(k) \equiv f(k_1, \dots, k_R)$ and the MPS procedure is applied on the resulting tensor. In this way, the finite bond dimensions take care of the entanglement between different scales of the wave vector k . This paper argues that for many functions, singular values of the SVD matrices of the MPS are small, allowing to compress the MPS without losing too much information. The basic data operations, such as a Fourier transform can be formulated in the compressed form in this framework. This enables the method to compute the imaginary time momentum and real-time dependence of correlation functions in equilibrium and non-equilibrium systems.

Based on the works of Oseledets [19] and Khomoskij [20], Refs. [21],[22],[17] state that for functions

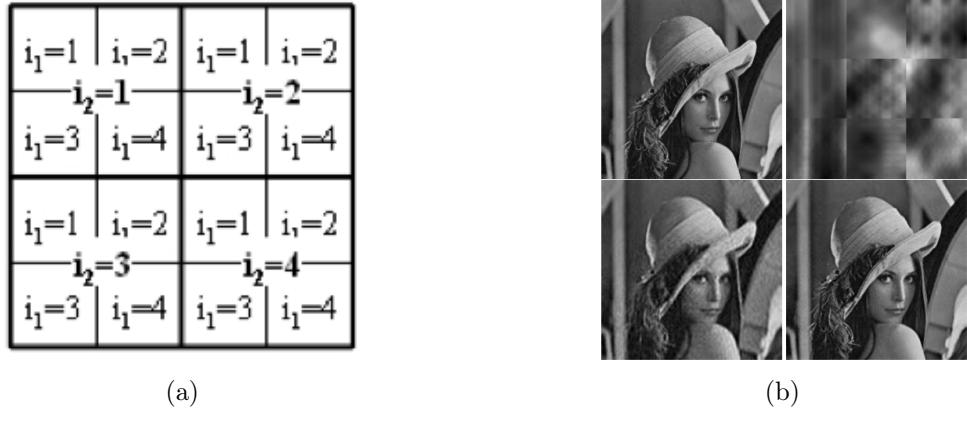


Figure 1.14: (a) Schematic illustration of the renormalization group inspired, addressing of pixel positions to cast an image into a ket function. (b) Compression of image; the original 6561 pixels image in the upper-left corner is compressed following the qpeg algorithm with $\chi_{\text{trunc}} = 1$ (right-upper corner, PSNR=17), 4 (left-lower corner, PSNR=25.6) and 8 (right-lower corner, PSNR=31.9). Figures are taken from Ref. [23].

that exhibit similar structure on different length scales, the corresponding MPS Ansatz exhibits small bond dimensions between the corresponding scales. Ref.[18] refers to this property as *strong compressibility*.

1.4.2 Image compression using MPS

Latorre [23] applies the same construction of tensors and MPS as the one given in Ref.[17], for the purpose of two-dimensional image compression. Each pixel (x, y) carries a value $f(x, y) \equiv f(x_1, y_1, \dots, x_R, y_R)$, where x_1, \dots, x_R and y_1, \dots, y_R are the base 2 representation of the coordinate. Then MPS procedure is applied on $f(x_1, \dots, y_R)$ (see Fig. 1.14(a)). This paper argues that the strong compressibility property hold for many real images carrying smooth texture, allowing efficient compression of the MPS representation. The compression method is however different from Shinaoka *et.al.*[17], where at each SVD, only singular values greater than a threshold are kept.

Lattore assigns a maximum bond dimension and then finds the state that minimizes the distance to the original one, leading to a converging iterative procedure. The process is summarized as follows; (1) Divide the original image in boxes. (2) Apply a discrete cosine Fourier transform to the box. (3) Cast the Fourier transformed box to $|\psi_i\rangle$ and make an MPS representation. (4) Truncate the MPS by a preassigned bond dimension χ_{trunc} .

Figure 1.14(b) shows the actual compression of the image photo. The original size of each block contains a total of 6561 integers in the range $[0 : 255]$. They use the common measure of the quality of compression is the PSNR measure in decibels, $\text{PSNR}(dB) = 10 \log_{10}(255^2 \text{MSE})$, where $\text{MSE} = 1/n \sum_i (y_i - x_i)^2$ means the sum over all n pixels of the squared difference between the original pixel value x_i and the one resulting from the compression y_i .

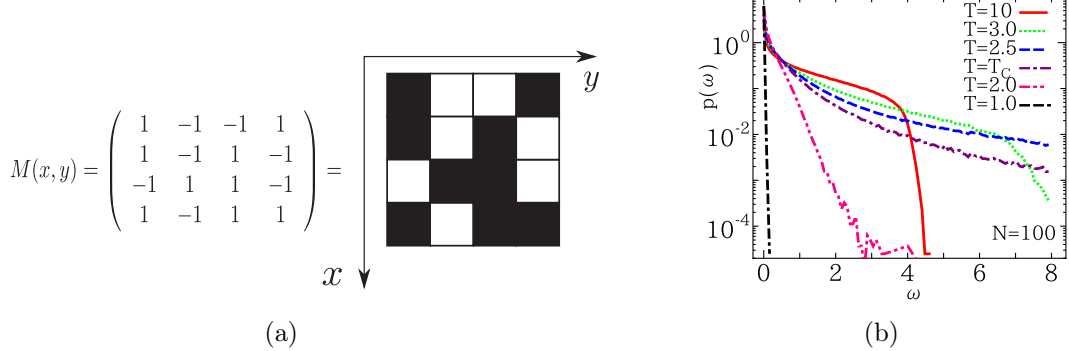


Figure 1.15: (a) Ising snapshot. (b) Snapshot singular values distribution for several temperatures in $N \rightarrow \infty$. Figure is taken from Ref.[24].

1.4.3 Snapshot analysis of 2D Ising model

The idea of processing the snapshot data of the physical phases is given previously in the other way around in Ref.[24]. This work by Imura, *et.al.* studied the critical phenomena in 2D ferromagnetic Ising model with periodic boundary conditions (PBC) using a SVD of the Ising snapshot represented by $M(x,y) = \pm 1$, where (x,y) is the position of the spin and $M(x,y)$ is up(+1) and down (-1) orientation of spin at that position (see Fig. 1.14a). They regard $M(x,y)$ as $L \times L$ matrix and perform an SVD to it. The normalized singular values of the SVD are called the snapshot spectrum $\{w_n\}$, which serves as a key ingredient of this paper. They are computed using a Householder diagonalization of the snapshot density matrix

$$\rho_X(x,x') = \frac{1}{N_y} \sum_{y=1}^{N_y} M(x,y) M(x',y),$$

which is real symmetric and $\text{tr}(\rho_X) = N_x$.

The distribution of snapshot spectrum $p(w) = \frac{1}{N_x} \sum_n \delta(w - w_n)$ is determined numerically on MC snapshots of 2D Ising model with PBC (Eq.(1.27)) for $N_x = N_y = N \rightarrow \infty$ ² One of the results is shown in Fig. 1.14b. Depending on T , the distribution is different :

- In the high T phase, $M(x,y)$ is a random matrix and ρ_X is a Wishart matrix in RMT ; this implies that there is an upper bound of eigenvalue distribution, which is observed.
- In the low T phase, the spins in a snapshot mostly have the same value, which implies (see the paper for the details) that a lot of singular values are zero, and this is confirmed by Fig. 1.14b where at low T , the distribution is picked in zero.
- In $T \sim T_c$, the distribution is fitted by a power-law $p(w) \propto w^{-\alpha}$ for $w \gg 1$, which is a direct evidence of the critical behavior.

A theoretical explanation of this power law decay at $T \sim T_c$ is proposed in the paper. The key argument is to say that in a snapshot, the average of two spins distant by $x - x'$ with respect to the y -direction equals to the matrix element of the reduced density matrix $\rho_X(x,x') \sim G(x-x') \equiv$

²they also studied the case $N_x < N_y$ but in this work we will stick to $N_x = N_y$.

$\langle S_{x,0}S_{x',0} \rangle$ by the self-averaging property. Using translational invariance, they diagonalized ρ_x by the Fourier transformation,

$$w(k) \sim |G(k)| \sim \left| \sum_{r=0}^{N-1} r^{-\eta} \exp(ikr) \right|,$$

where $r = |x - x'|$ and $k = 2\pi n/N$. In the limit $N \rightarrow \infty$ the function $w(k)$ can be evaluated as an integral and $w(k) \sim |k^{\eta-1}|$. From this they derived

$$p(\omega) \sim w^{\frac{(2-\eta)}{(1-\eta)}}. \quad (1.56)$$

For the Ising model $\eta = 1/4$, the exponent is $7/3$, which confirms their observation.

In our work, we will also try to discriminate the different phases of the 2D Ising model, but using the entanglement between different scales, stored in the MPS constructed by scale separation. We will be able to detect the different phases, with a very small amount of classical Monte Carlo sample, compared to the large amount $5 \times (10^3 - 1) \times 10^5$ used to compute $p(\omega)$ in Ref.[24]. Moreover, we will show that using the compression feature of the MPS, it is possible to read the critical temperature.

Chapter 2

Encoding data as Quantum state

2.1 Tensor train format of data

In this section, we establish a mapping scheme based on the base- q representation of real numbers. This mapping connects coordinates within a D -dimensional discrete cube to a base q Hamming-like cube. As each coordinate carries data, this mapping allows us to define its tensor representation, where legs have bond dimension q and represent the base q digits. Following this strategy, we delve into the concept of Regrouped Scale Tensor Train Format (RSTTF) for efficient representation of high-dimensional functions on the discrete cube, which consists of regrouping by scale the legs of the tensor, and then viewing it as the coefficient of a many-body quantum state.

2.1.1 Mapping coordinates using their base q representation

We first explain how to map the coordinates defined on a D -dimensional discrete lattice point to a base q Hamming-like cube. The D dimensional discrete cube of linear size n , is defined as a set of coordinates $\mathbb{Q}_n^D := \llbracket 0, n - 1 \rrbracket^D$ where $D \in \mathbb{N}^*$ and $n \in \mathbb{N}^*$. This set can be mapped to vertices of D -dimensional cubic lattices. (Fig. 2.1).

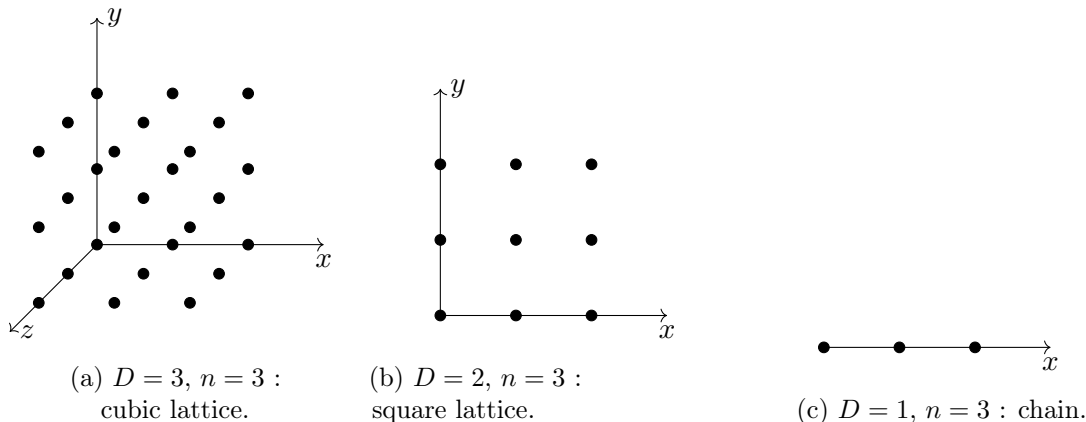


Figure 2.1: Some lattices whose vertices can be mapped to the D dimensional discrete cube of size n . For example for the 2D square lattices, the first layer of vertices, at $y = 0$, can be mapped to $(0, 0), (1, 0), (2, 0)$, and the second layer, at $y = 1$ to $(1, 0), (1, 1), (2, 1)$.

Any point in \mathbb{Q}_n^D is indexed by a set of integers $\mathbf{i} = (i_1, \dots, i_D)$

$$\frac{i_k}{n} \in [0, 1[\quad \forall k \quad (2.1)$$

Suppose that the linear size can be written as $n = q^R$ where $q \in \{2, 3, \dots\}$ and $R \in \mathbb{N}^*$. In other words, dividing the total number of points R times by q determines the number of points in one dimension.

Consider the base- q representation of the normalized k -th coordinate of a point : $\frac{i_k}{n}$, that is exact regarding the expression of n :

$$\frac{i_k}{n} = \sum_{j=1}^R \frac{x_j^k}{q^j} \quad (2.2)$$

where (x_1^k, \dots, x_R^k) are defined as the base q digits of i_k . This representation defines a one-to-one mapping $\mathbf{b}_{q,R}$ between $\mathbb{Q}_{n=q^R}^D$ and the set $\mathbb{F}_q^{D \cdot R} := \llbracket 0, q-1 \rrbracket^{D \cdot R}$

$$\mathbf{b}_{q,R} : \mathbb{F}_q^{D \cdot R} \rightarrow Q_{q^R}^D \quad (2.3)$$

$$(x_1^1, \dots, x_R^1, \dots, x_1^D, \dots, x_R^D) \mapsto \frac{1}{n}(i_1, \dots, i_D) \quad (2.4)$$

Example 1. Consider a chain of $q^R = 2^3 = 8$ atoms (Fig. 2.2). Each atom belongs to a division of space, where 3 division by 2 has been made. Their coordinate in $Q_{n=2^3}^{D=1}$ can then be mapped to their bit ($q = 2$) representation. The mapping works in the following way: the first division of space (biggest dashed line) determines the first digit of the bits representation, so all vertices on the left have $x_1^1 = 0$ and all the right ones $x_1^1 = 1$. Then take each obtained division and divide them again in two, and this will determine the second bits; all atoms in the first and third quarter will have $x_2^1 = 0$, and the other $x_2^1 = 1$. Repeat this process R times in total.

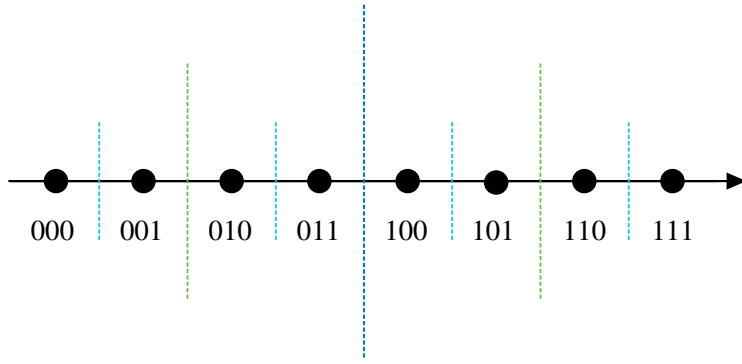


Figure 2.2: Illustration of the attribution of the base 2 sequence to each site of a one-dimensional chain.

Example 2. Consider a two-dimensional square lattice $D = 2$ with linear size $n = 2^2$ (see Fig. 2.3), corresponding to $q = 2$ and $R = 2$. Then any point in this lattice verifies

$$2^2 \mathbf{b}_{2,2}(x_1^1, x_2^1, x_1^2, x_2^2) = (i_1, i_2)$$

For example

$$2^2 \mathbf{b}_{2,2}(0, 1, 1, 1) = 2^2 \left(\frac{0}{2^1} + \frac{1}{2^1}, \frac{1}{2^1} + \frac{1}{2^2} \right) = (2, 3)$$

The mapping between the square lattice Q_n^D with $n = 2^R$ is obtained by diving it into 4 sub-lattices, then again diving each obtained sub-lattices in 4, and repeating the procedure R times. The first division corresponds to the first scale, the coarsest scale and the position of a point in one of these 4 is represented by the first bits in the base-2 representation. The second division corresponds to the second bits, etc.

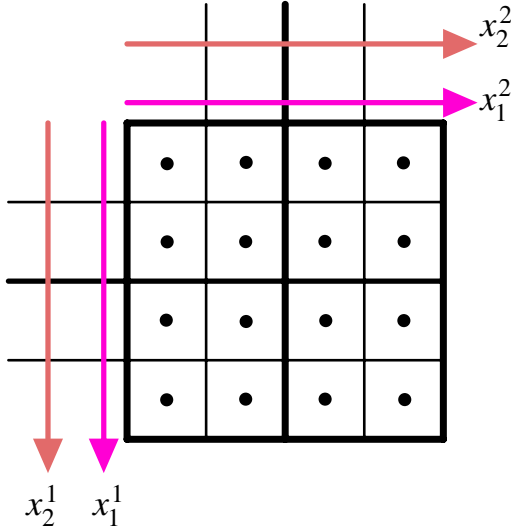


Figure 2.3: Illustration of mapping between the square lattice of linear size 2^2 through the bits representation of the point.

To be brief, when we represent the location of a certain site on a D dimensional cube as a set of coordinates, $\mathbb{Q}_{n=q^R}^D$, each of the variables in $(x_1^1, \dots, x_R^1, \dots, x_1^D, \dots, x_R^D)$ represents the location about each scale indexed as $1, \dots, R$.

2.1.2 Regrouped Scale Tensor Train Format (RSTTF)

Regrouped Scale Multi-leg tensor (RSMLT)

We now introduce the Regrouped Scale Tensor Train Format (RSTTF) applied to any high-dimensional function. Consider a real valued function $f(i_1, \dots, i_D)$ defined on $\mathbb{Q}_{n=q^R}^D$. Then, using the mapping introduced in Section 2.1.1, we obtain

$$f(i_1, \dots, i_D) = (f \circ \mathbf{b}_{q,R})(x_1^1, \dots, x_R^1, \dots, x_1^D, \dots, x_R^D). \quad (2.5)$$

The right-hand side can be seen as the coefficient of a rank $D \cdot R$ tensor where each leg has dimension $d = q$. For convenience, let us regroup the indices of that tensor by scale :

$$(f \circ \mathbf{b}_{q,R})(x_1^1, \dots, x_1^D, \dots, x_R^1, \dots, x_R^D) = (f \circ \mathbf{b}_{q,R})(\mathbf{x}_1, \dots, \mathbf{x}_R). \quad (2.6)$$

Now that we have expressed a high dimensional function as a multi-legs tensor, with each index representing one bit of the base q representation of one of the coordinates. Let us call this tensor the Regrouped Scale Multi-Legs Tensor (RSMLT) associated to the function f on $\mathbb{Q}_{n=q^R}^D$. After applying the MPS procedure on that tensor, we obtain the so-called the *regrouped scaled Tensor Train Format* (RSTTF) of the function f on $\mathbb{Q}_{n=q^R}^D$.

Mapping to a quantum state

Now, consider $\mathbb{Q}_{q^R}^D$, the D dimensional discrete cube of linear size $n = q^R$, and denote the RSMLT of a function $f(i_1, \dots, i_D)$ on this set as $\psi_{\mathbf{x}_1, \dots, \mathbf{x}_R}$. This tensor ψ can be seen as the coefficients of a many-body quantum state $|\psi\rangle$ living in a Hilbert space,

$$\mathbb{H}_{\mathbf{x}_1 \dots \mathbf{x}_R} =: \otimes_{i=1}^R \mathbb{H}_{\mathbf{x}_i},$$

where $\mathbb{H}_{\mathbf{x}_i} = \mathbb{C}^{q^D}$ represents the degrees of freedom at scale i of the quantum state. Physically, in our work, the snapshot of a classical state is converted to a fictitious quantum state using RSTTF. We will show the examples in the following sections.

2.2 Data encoding

We first show how to encode the $D = 2$ snapshot data to RSTTF. Then, show the example of the Cantor set represented by RSTTF, which can be solved analytically.

2.2.1 2D Snapshot and image compression

A *snapshot* in 2D is defined as a square matrix S_{ij} with i, j being the indices of the Cartesian coordinate. This square matrix carries two-dimensional data, where the simplest example is a black-and-white image as a binary function, $S_{ij} = \pm 1$. In reality, S_{ij} can be set to store more information depending on the variation of the color of the pixel.

Formally, consider the $D = 2$ dimensional discrete cube of size $n = q^R$, and a function $f(i_1, i_2)$ defined on it. Then, the snapshot associated with f is defined as a matrix $S_{i_1 i_2} = f(i_1, i_2)$, of size $q^R \times q^R$. For simplicity of notation, in the case of snapshots, the base- q digits of a point (i_1, i_2) in the 2D cube will be denoted as

$$(x_1^1, x_1^2, \dots, x_R^1, x_R^2) = (x_1, y_1, x_2, y_2, \dots, x_R, y_R)$$

where we dropped the upper script, representing the axis where the coordinate belongs to.

Consider the snapshot given in Fig. 2.4. The function f of that snapshot is defined as $f(0, 0) = f(0, 1) = f(1, 0) = f(1, 1) = f(0, 3) = f(1, 2) = f(1, 3) = 1$ and -1 on all the other points.

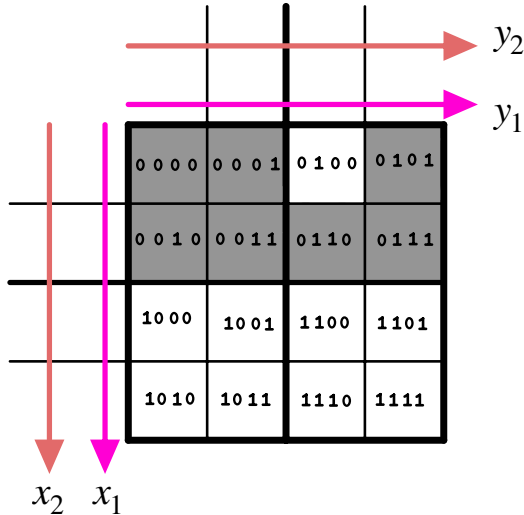


Figure 2.4: Snapshot of linear size $q^R = 2^2$, where S_{ij} is black or white. In each box is written the base-2 digits x_1, y_1, x_2, y_2 of the associated point $(i_1, i_2) \in [0, 3]^2$, regrouped by scale.

Then the quantum state associated with the RSMLT of the snapshot is,

$$|\psi\rangle = \sum_{x_1, x_2, y_1, y_2 \in \{0, 1\}} \psi_{x_1 y_1 x_2 y_2} |x_1, y_1, x_2, y_2\rangle = \psi_{0000} |0, 0, 0, 0\rangle + \psi_{0001} |0, 0, 0, 1\rangle + \dots, \quad (2.7)$$

and $\psi_{x_1 y_1 x_2 y_2} = S_{b_{q=2, R=2}(x_1, y_1, x_2, y_2)}$.

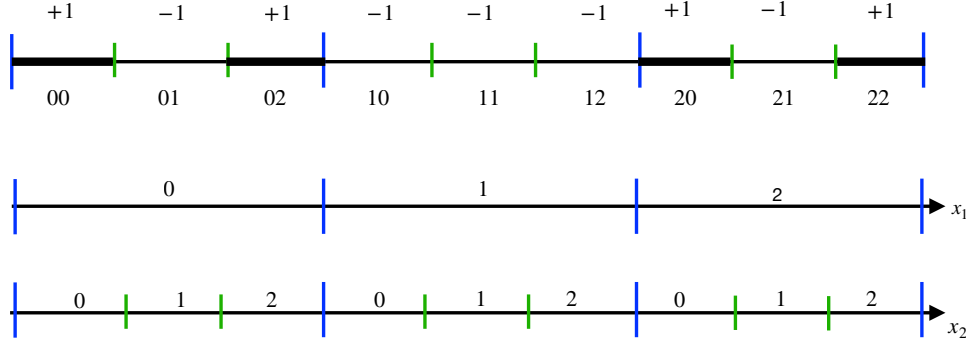


Figure 2.5: Diagram of the discrete Cantor set at iteration $R = 2$. The top panel is the assignment of the values, where each segment has a value ± 1 . The lower two panels are the coordinates, x_1, x_2 , given as a sequence of base 3 digits. Generally, the first digit (x_1) represents the position among the largest segment, and the last digit the most precise scale.

2.2.2 Quantum Cantor state

To illustrate the way one transforms some data into a quantum state, we will construct a well-known example and obtain its RSTTF analytically.

Consider the discrete cantor set at iteration R defined as a function f_{cantor} of the set $\mathbb{Q}_{n=3^R}^{D=1}$. This function assigns to each point $i \in \{0, \dots, 3^R - 1\}$ a value ± 1 in the following way :

- Start with the $[0, 1] \subset \mathbb{R}$ segment.
- Divide the segment in three, each segment is assigned a value: the middle has value -1 and both sides as $+1$, giving the discrete cantor set $(1, -1, 1)$, at iteration $R = 1$.
- The $(R + 1)$ -th iteration applies the same procedure to each segment, giving rise to 3^{R+1} segments, e.g. the obtained discrete cantor set is, at $R = 2$ the vector $(1, -1, 1, -1, -1, 1, -1, 1)$.

Each segment in the discrete cantor set can be mapped to a sequence of coordinate $(x_1 x_2 \cdots x_R)$ where $x_i \in \{0, 1, 2\}$ corresponding to the base 3 representation of its position in the vector. For example at iteration 2, we have the mapping shown in Fig. 2.5.

The discrete cantor set is a 1D data (vector). This data is mapped to a quantum state $|\psi_R^{\text{cantor}}\rangle \in \mathbb{H}_{x_1 x_2 \cdots x_R}$, where the total Hilbert space is the product of the Hilbert space associated with each scale $\mathbb{H}_{x_1 x_2 \cdots x_R} = \mathbb{H}_{x_1} \otimes \mathbb{H}_{x_2} \otimes \cdots \otimes \mathbb{H}_{x_R}$ with $\mathbb{H}_{x_i} = \mathbb{C}^3$. The coefficients $\psi_{x_1 x_2 \cdots x_R}$ of this quantum state store the values, $\{1, -1\}$, at the location in terms of base 3 sequence, $(x_1 x_2 \cdots x_R)$.

Example. We first explicitly write down the $R = 2$ quantum state as

$$\begin{aligned} |\psi_2^{\text{cantor}}\rangle &= (+1) |0\rangle_{x_1} |0\rangle_{x_2} + (-1) |0\rangle_{x_1} |1\rangle_{x_2} + (+1) |0\rangle_{x_1} |2\rangle_{x_2} \\ &\quad + (-1) |1\rangle_{x_1} |0\rangle_{x_2} + (-1) |1\rangle_{x_1} |1\rangle_{x_2} + (-1) |1\rangle_{x_1} |2\rangle_{x_2} \\ &\quad + (+1) |2\rangle_{x_1} |0\rangle_{x_2} + (-1) |2\rangle_{x_1} |1\rangle_{x_2} + (+1) |2\rangle_{x_1} |2\rangle_{x_2}, \end{aligned}$$

where the first line corresponds to points in the first blue segment, the second line to the middle

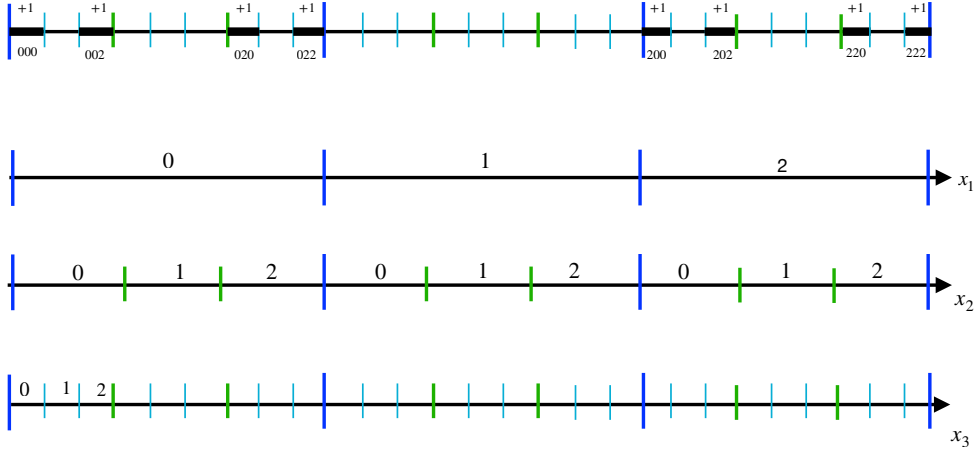


Figure 2.6: Discrete cantor set for $R = 3$.

blue segments, and the last line to the last blue segment on the right. It is rewritten as

$$\begin{aligned} |\psi_2^{\text{cantor}}\rangle &= (-1)|1\rangle_{x_1} \otimes (|0\rangle_{x_2} + |1\rangle_{x_2} + |2\rangle_{x_2}) & [\cdot, \cdot, \cdot, -1, -1, -1, \cdot, \cdot, \cdot] \\ &+ (-1)(|0\rangle_{x_1} + |2\rangle_{x_1}) \otimes |1\rangle_{x_2} & [\cdot, -1, \cdot, \cdot, \cdot, \cdot, -1, \cdot] \\ &+ (|0\rangle_{x_1} + |2\rangle_{x_1}) \otimes (|0\rangle_{x_2} + |2\rangle_{x_2}) & [1, \cdot, 1, \cdot, \cdot, \cdot, 1, \cdot, 1]. \end{aligned}$$

For $R = 3$, the quantum state is given as

$$\begin{aligned} |\psi_2^{\text{cantor}}\rangle &= (+1)|0\rangle_{x_1}|0\rangle_{x_2}|0\rangle_{x_3} + (-1)|0\rangle_{x_1}|0\rangle_{x_2}|1\rangle_{x_3} + (+1)|0\rangle_{x_1}|0\rangle_{x_2}|2\rangle_{x_3} \\ &+ (-1)|0\rangle_{x_1}|1\rangle_{x_2}|0\rangle_{x_3} + (-1)|0\rangle_{x_1}|1\rangle_{x_2}|1\rangle_{x_3} + (-1)|0\rangle_{x_1}|1\rangle_{x_2}|2\rangle_{x_3} \\ &+ (+1)|0\rangle_{x_1}|2\rangle_{x_2}|0\rangle_{x_3} + (-1)|0\rangle_{x_1}|2\rangle_{x_2}|1\rangle_{x_3} + (+1)|0\rangle_{x_1}|2\rangle_{x_2}|2\rangle_{x_3} \\ &+ (-1)|1\rangle_{x_1}|0\rangle_{x_2}|0\rangle_{x_3} + (-1)|1\rangle_{x_1}|0\rangle_{x_2}|1\rangle_{x_3} + (-1)|1\rangle_{x_1}|0\rangle_{x_2}|2\rangle_{x_3} \\ &+ (-1)|1\rangle_{x_1}|1\rangle_{x_2}|0\rangle_{x_3} + (-1)|1\rangle_{x_1}|1\rangle_{x_2}|1\rangle_{x_3} + (-1)|1\rangle_{x_1}|1\rangle_{x_2}|2\rangle_{x_3} \\ &+ (-1)|1\rangle_{x_1}|2\rangle_{x_2}|0\rangle_{x_3} + (-1)|1\rangle_{x_1}|2\rangle_{x_2}|1\rangle_{x_3} + (-1)|1\rangle_{x_1}|2\rangle_{x_2}|2\rangle_{x_3} \\ &+ (+1)|2\rangle_{x_1}|0\rangle_{x_2}|0\rangle_{x_3} + (-1)|2\rangle_{x_1}|0\rangle_{x_2}|1\rangle_{x_3} + (+1)|2\rangle_{x_1}|0\rangle_{x_2}|2\rangle_{x_3} \\ &+ (-1)|2\rangle_{x_1}|1\rangle_{x_2}|0\rangle_{x_3} + (-1)|2\rangle_{x_1}|1\rangle_{x_2}|1\rangle_{x_3} + (-1)|2\rangle_{x_1}|1\rangle_{x_2}|2\rangle_{x_3} \\ &+ (+1)|2\rangle_{x_1}|2\rangle_{x_2}|0\rangle_{x_3} + (-1)|2\rangle_{x_1}|2\rangle_{x_2}|1\rangle_{x_3} + (+1)|2\rangle_{x_1}|2\rangle_{x_2}|2\rangle_{x_3} \end{aligned}$$

General expression. Based on the quantum state representation of $R = 2, 3$, we reach the expression for arbitrary iteration number R , given as

$$|\psi_R^{\text{cantor}}\rangle = \underbrace{(|0\rangle + |2\rangle)_{x_1 \dots x_R}}_{=: |\psi_R^1\rangle} + \sum_{i=1}^R (-1) \underbrace{(|0\rangle + |2\rangle)_{x_1 \dots x_{i-1}} |1\rangle_{x_i} (|0\rangle + |1\rangle + |2\rangle)_{x_{i+1} \dots x_R}}_{=: |\psi_R^{i,-1}\rangle}. \quad (2.8)$$

Using the notation, $|\psi\rangle_{abcde\dots} = |\psi\rangle_a \otimes |\psi\rangle_b \otimes |\psi\rangle_c \otimes \dots$, one can write this state even more compactly as

$$|\psi_R^{\text{cantor}}\rangle = |\psi_R^1\rangle - \sum_{i=1}^R |\psi_{i-1}^1\rangle \otimes |1\rangle_{x_i} \otimes (|0\rangle + |1\rangle + |2\rangle)_{x_{i+1}\dots x_R} \quad (2.9)$$

where the term for $i = 1$ equals $|1\rangle_{x_1} \otimes (|0\rangle + |1\rangle + |2\rangle)_{x_2\dots x_R}$. Let us call the state given in Eq. (2.8) the *Quantum Cantor State* (QCS).

One useful property of that state is that it satisfies,

$$\langle \psi_R^1 | \psi_R^{i,-1} \rangle = 0, \quad \forall i \in \llbracket 1, R \rrbracket. \quad (2.10)$$

Normalization of the cantor quantum state. We normalize the quantum state defined in Eq. (2.8).

$$\langle \psi_R^{\text{cantor}} | \psi_R^{\text{cantor}} \rangle = \left(\langle \psi_R^1 | - \sum_{j=1}^R \langle \psi_R^{j,-1} | \right) \left(|\psi_R^1\rangle - \sum_{j=1}^R |\psi_R^{j,-1}\rangle \right),$$

and by developing the product one finds,

$$\langle \psi_R^{\text{cantor}} | \psi_R^{\text{cantor}} \rangle = \underbrace{\langle \psi_R^1 | \psi_R^1 \rangle}_{=2^R} - \underbrace{\sum_{j=1}^R \langle \psi_R^1 | \psi_R^{j,-1} \rangle}_{=0} - \underbrace{\sum_{j=1}^R \langle \psi_R^{j,-1} | \psi_R^1 \rangle}_{=0} + \sum_{j,l=1}^R \langle \psi_R^{j,-1} | \psi_R^{l,-1} \rangle.$$

We compute the last term :

$$\begin{aligned} \sum_{j,l=1}^R \langle \psi_R^{j,-1} | \psi_R^{l,-1} \rangle &= \sum_{j=1}^R \langle \psi_R^{j,-1} | \psi_R^{j,-1} \rangle \\ &= \sum_{j=1}^R 2^{j-1} 3^{R-j} \\ &= 3^R 2^{-1} \sum_{j=1}^R (2 \cdot 3^{-1})^j \\ &= 3^R 2^{-1} \left(\frac{1 - (2 \cdot 3^{-1})^R}{1 - 2 \cdot 3^{-1}} \right) \\ &= 3^{R-1} \left(\frac{1 - (2/3)^R}{1/3} \right) \\ &= 3^R - 2^R \end{aligned}$$

So finally, the normalization of the quantum cantor state is given as

$$\langle \psi_R^{\text{cantor}} | \psi_R^{\text{cantor}} \rangle = 2^R + (3^R - 2^R) = 3^R.$$

For the QCS to be normalized to 1, we have,

$$|\psi_R^{\text{cantor}}\rangle \rightarrow \frac{1}{\sqrt{3^R}} |\psi_R^{\text{cantor}}\rangle.$$

Now that we have found the full description of the QCS, we can examine its characteristics. QCS is known to have a scale-invariant structure, and indeed, it is reflected in the nature of RSTTF. The details of such analysis are presented shortly in Section 3.1.1.

2.3 Interscale entanglement entropy and bond dimension

2.3.1 Physical interpretation of bond dimension

Again, consider a snapshot $S_{i_1, i_2} = f(i_1, i_2)$ and the quantum state $|\psi\rangle$ associated with RSMLT.

$$|\psi\rangle = \sum_{x_1 y_1 \cdots x_R y_R} \psi_{x_1 y_1 \cdots x_R y_R} |x_1 y_1 \cdots x_R y_R\rangle. \quad (2.11)$$

Let the bond of the RSTTF at which we make a bipartition be denoted as either $(x_1 y_1 \cdots x_i y_i | x_{i+1} \cdots x_R)$ or $(x_1 y_1 \cdots x_i | y_i x_{i+1} \cdots x_R)$, depending on the two choices for each scale $i = 1, \dots, R$. We have basically $j = 0, \dots, 2R - 2$ choices of bipartition, and for each we define the EE as S_j .

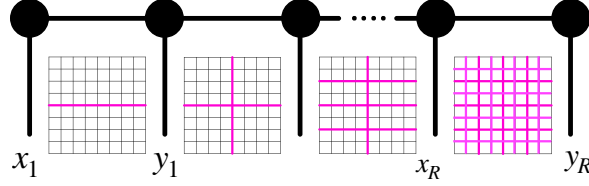


Figure 2.7: Interpretation of the structure of MPS of the RSTTF of a 2D snapshot.

Figure 2.7 shows the schematic snapshot for comprehensiveness; from left to right, each bond $x_i | y_i$ divides the x axis (vertical axis) into q horizontal sub-snapshots, and so as $y_i | x_{i+1}$ the y axis into q vertical sub-snapshots.

To understand the physical implication of the division, we show in Fig. 2.8 the example. Suppose we have a state defined on $\mathbb{Q}_{n=q^R}^{D=2}$. The finest boxes (black boxes) of this mesh grid have positions determined by $(x_1 y_1 \cdots x_R y_R)$. The smaller boxes in the red mesh have position determined by $(x_1 y_1 \cdots x_i y_i)$. We have $2^i \times 2^i = 16$ ($i = 2$) red boxes, each containing $2^{R-i} \times 2^{R-i}$ data points (smaller boxes) which carry a *sub-snapshot* information represented by $|\psi(x_1 \cdots y_i)\rangle$, that shall differ depending on which red box we choose. Then, the whole quantum state at that bipartition is given as a superposition of these sixteen sub-snapshots as

$$|\psi\rangle = \sum_{x_1 \cdots y_i} |x_1 \cdots y_i\rangle \otimes |\psi(x_1 \cdots y_i)\rangle \quad (2.12)$$

$$= \sum_{s=1}^{2^i} \underbrace{(\text{coarse-grained snapshot down to scale-}i)}_{\in \mathbb{H}_{x_1 \cdots y_i}} \otimes \underbrace{(\text{sub-snapshot of scale-}i)}_{\in \mathbb{H}_{x_{i+1} \cdots y_R}}, \quad (2.13)$$

which we say that *we look at the data at scale- i* . For that bipartition, the matrix of $|\psi\rangle$ is such that each row specified by a set of $(x_1 \cdots y_i)$ is made of the coefficients of $|\psi(x_1 \cdots y_i)\rangle$. The number of linearly independent rows is the rank of the matrix, which is the dimension of the bond $(x_1 y_1 \cdots x_i y_i | x_{i+1} y_{i+1} \cdots x_R y_R)$. Because each row is a sub-snapshot, one can write the following property :

Properties 2.3.1 (Interpretation of inter-scale bond dimension.). The bond dimension r_i of the bipartition $(x_1 y_1 \cdots x_i y_i | x_{i+1} y_{i+1} \cdots x_R y_R)$ equals the number of linearly independent sub-snapshots at scales $x_1 y_1 \cdots x_i y_i$. More generally, for the RSTTF of f on $\mathbb{Q}_{n=q^R}^D$, the bond dimension determines

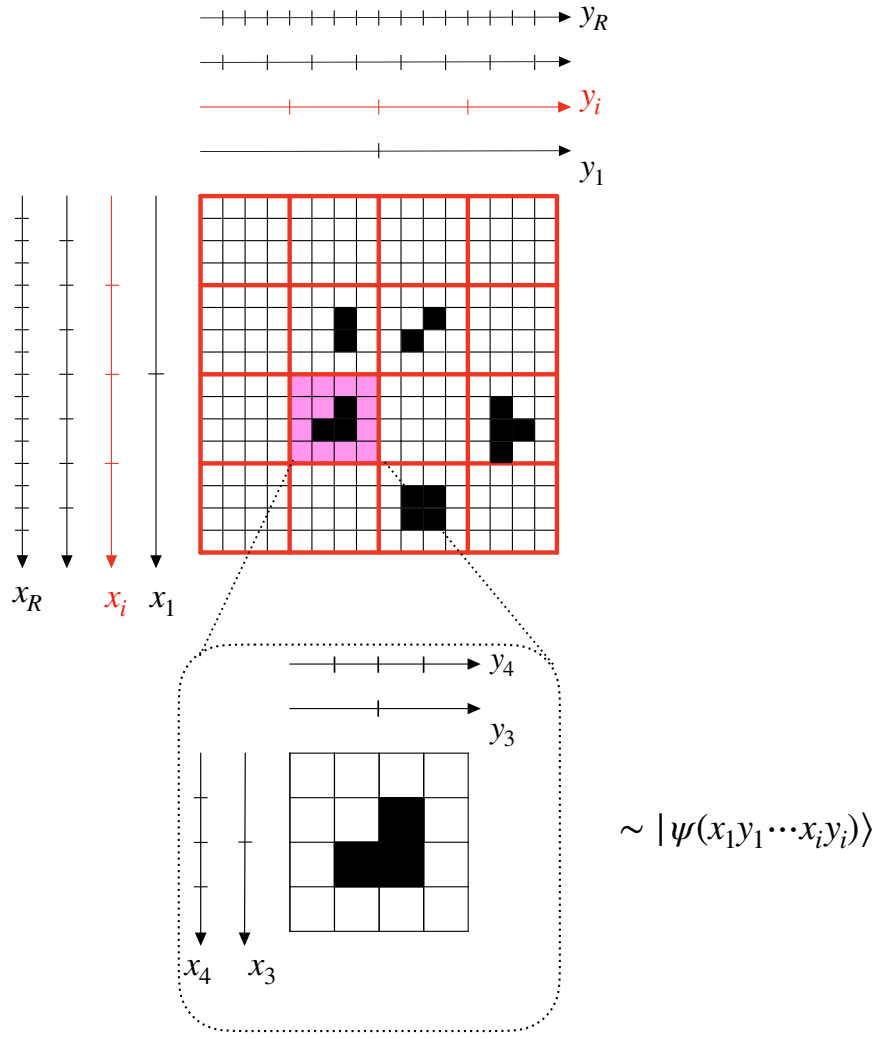


Figure 2.8: Schematic illustration of the snapshot on a $\mathbb{Q}_{n=q^R}^{D=2}$ as a grid box where $R = 4$. Each box carries black/white data and is assigned a position $(x_1 y_1 \cdots x_R y_R)$. The bipartition is made at scale i shown in red boxes as, $(x_1 \cdots y_i | x_{i+1} \cdots x_R)$. Each set of $2^{R-i} \times 2^{R-i}$ data points inside each red box is represented by $|\psi(x_1 \cdots y_i)\rangle$ and is called sub-snapshot. The whole wave function is given by the superposition of the combination coarse-grained snapshot $|x_1 \cdots y_i\rangle \otimes$ sub-snapshot $|\psi(x_1 \cdots y_i)\rangle$.

the number of linearly independent sub- D dimensional cubes at scales fixed by all physical indices on the left of the bond.

Two snapshots S_{i_1, i_2} and S'_{i_1, i_2} are linearly dependent if exists a non trivial combination $\alpha S + \beta S' = 0$.

Example 1. To understand the previous discussion, which may be quite abstract at that point let us compute the inter-scale bond dimension r_1 for the simple snapshot (2.7). We assign black point as $S_{i_1, i_2} = 1$ and white point 0. Then, the quantum state is

$$\begin{aligned} |\psi\rangle = & 1 \cdot |0000\rangle + 1 \cdot |0001\rangle + 1 \cdot |0010\rangle + 1 \cdot |0011\rangle \\ & 0 \cdot |0100\rangle + 1 \cdot |0101\rangle + 1 \cdot |0110\rangle + 1 \cdot |0111\rangle \\ & 0 \cdot |1000\rangle + 0 \cdot |1001\rangle + 0 \cdot |1010\rangle + 0 \cdot |1011\rangle \\ & 0 \cdot |1100\rangle + 0 \cdot |1101\rangle + 0 \cdot |1110\rangle + 0 \cdot |1111\rangle. \end{aligned} \quad (2.14)$$

We can write this state as a tensorial product state

$$|\psi\rangle = \underbrace{|0\rangle}_{\in \mathbb{H}_{x_1}} \otimes \underbrace{(|000\rangle + |001\rangle + |010\rangle + |011\rangle + |100\rangle + |101\rangle + |110\rangle + |111\rangle)}_{\in \mathbb{H}_{y_1 x_2 y_2}}, \quad (2.15)$$

meaning that the Schmidt rank between \mathbb{H}_{x_1} and $\mathbb{H}_{y_1 x_2 y_2}$ is equal to 1 and the state is not entangled. However, if we suppose that black is $S_{i_1, i_2} = 1$ and white is -1 , then the state becomes entangled. We can see that by writing the matrix $\psi_{x_1|y_1 x_2 y_2}$:

$$\begin{array}{cccccccccc} & 000 & 001 & 010 & 011 & 100 & 101 & 110 & 111 & \\ \psi_{x_1|y_1 x_2 y_2} = & \left(\begin{array}{cccccccc} 1 & 1 & 1 & 1 & -1 & 1 & 1 & 1 \\ -1 & -1 & -1 & -1 & -1 & -1 & -1 & -1 \end{array} \right) & & & & & & & & \end{array} \quad (2.16)$$

This matrix has two linearly independent rows, so its rank is 2, and the quantum state is entangled. This small example illustrates the following; if one has an image of black and white pixels, then the way we map the colors to the snapshot values seems to have an impact on the entanglement of the associated scaled regrouped quantum state. We will come back to this problem.

Example 2. Now, consider a series a snapshots of size $2^3 \times 2^3$ at left column of Fig. 2.9, where each color is data and the snapshot is expressed in the RSTTF. The bond dimension and the EE are plotted without truncation. The second snapshot is made of 4 sub-snapshots having an individual color. Dividing it into 2 parts leads to two linearly independent snapshots, hence a bond dimension is 2, confirmed by the right blue plot. Now, dividing again the figure into 4, we obtain 4 sub-snapshots, each one carrying one color. Because any matrices with constant entries for each matrix are linearly dependent, the bond dimension is 1. Dividing further, we will not encounter any particular structure but stay in one-color sub-snapshots, illustrating the constant bond dimension 1.

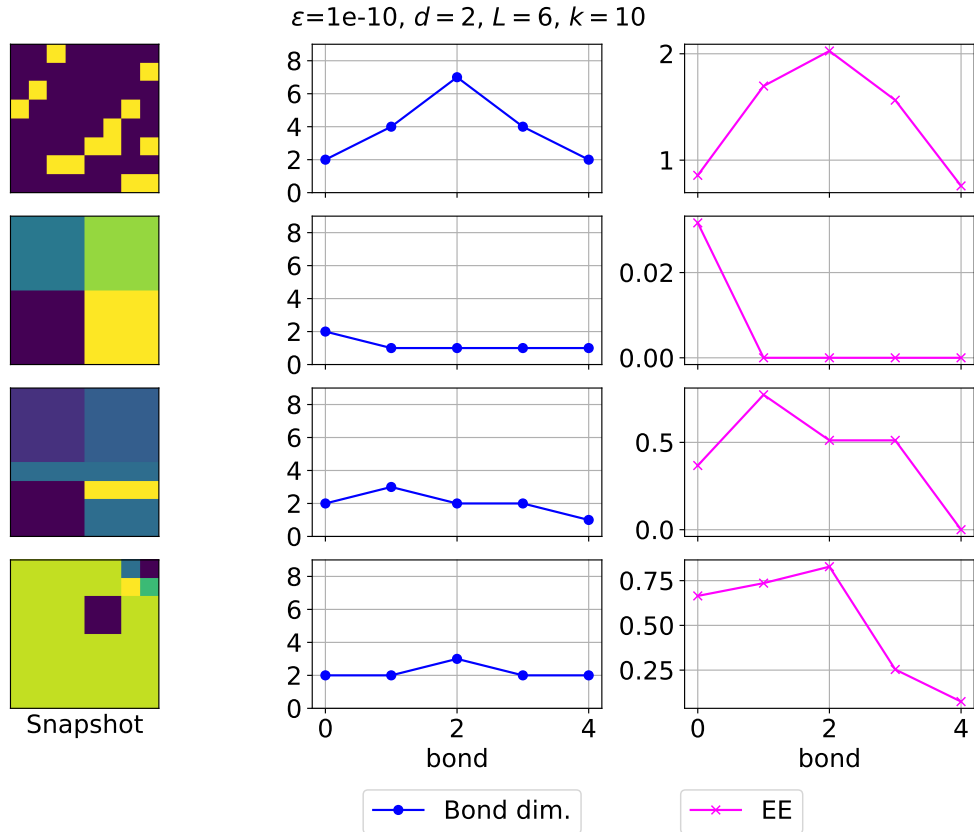


Figure 2.9: Example of the analysis of bond dimensions on the simple colored snapshots. The first column presents several snapshots that are analyzed. For each, bond dimension and EE are plotted on respectively second and third columns, obtained without truncation.

Chapter 3

Analyses of phases using tensor train format

In this Chapter, using the RSTTF framework, we analyze the quantum Cantor set and more generally self-similar structure, 2D classical Ising critical phase, and 3D Heisenberg spin glass phase. The Cantor set, with its self-similar and scaling properties, draws parallels to critical phenomena. In a similar manner, physical systems near phase transitions display scale invariance [25] with observables exhibiting power-law behavior. We first compare the results of these two established phases to understand how the underlying structures of complex real space configurations may become visible in the entanglement-related quantities of RSTTF. In the spin glass, we find that the real space spin configuration is not different from the paramagnet at high temperature, while instead the replica overlaps snapshot shall behave critically near the spin glass transition, and can be captured within the present framework.

3.1 Self-similarity

3.1.1 Quantum cantor set

Analytical form of the local density matrix

As the Cantor set is constructed through recursive removal of segments [26], it exhibits a fractal structure, reflecting scale invariance. In this section, we will prove rigorously, that it is possible to use the RSTTF of the discrete version of the cantor set we built in Section 2.2.2 to detect its self-similarity. For that purpose, we will compute analytically the interscale bond dimension using the reduced density matrix formalism (Sec.1.1.3) as a function of the bond index. This part is rather technical and the reader may go directly to the result presented at Eq.(3.28).

Properties 3.1.1. Let α_i be the number of tensorial product states in $\mathbb{H}_{x_{i+1} \dots x_R}$ that contains no $|1\rangle$ and let β_i be the number of states that contains at least one $|1\rangle$. Then we find the following relations :

$$\alpha_i = 2^{R-i} \tag{3.1}$$

$$\alpha_i + \beta_i = \#\mathbb{H}_{x_{i+1} \dots x_R} = 3^{R-i} \tag{3.2}$$

Proof. The first relation holds because a state in $\mathbb{H}_{x_{j+1} \cdots x_R}$ is written $|i_{j+1}, \dots, i_R\rangle$ where each $i_k \in \{0, 2\}$ giving a total number of 2^{R-j} states. The second relation is obvious because a state either contains no $|1\rangle$, or it contains at least one $|1\rangle$. \square

Let us define $\hat{\rho}_{x_1 \cdots x_k}$ as the reduced density matrix $\text{Tr}_B(|\psi_R^{\text{cantor}}\rangle \langle \psi_R^{\text{cantor}}|)$ where $A = (x_1 \cdots x_k)$ and $B = (x_{k+1} \cdots x_R)$. Then by definition, we have

$$\hat{\rho}_{x_1 \cdots x_k} = \sum_{\mathbf{i} \in \{0,1,2\}^{R-k}} \langle i_{k+1}, \dots, i_R | \psi_R^{\text{cantor}} \rangle \langle \psi_R^{\text{cantor}} | i_{k+1}, \dots, i_R \rangle \quad (3.3)$$

By using the expression of the QCS (2.8), this becomes

$$\begin{aligned} \hat{\rho}_{x_1 \cdots x_k} &= \sum_{\mathbf{i} \in \{0,1,2\}^{R-k}} \langle i_{k+1}, \dots, i_R | \psi_R^1 \rangle \langle \psi_R^1 | i_{k+1}, \dots, i_R \rangle \\ &\quad - \underbrace{\sum_{\mathbf{i} \in \{0,1,2\}^{R-k}} \langle i_{k+1}, \dots, i_R | \psi_R^1 \rangle \sum_{j=1}^R \langle \psi_R^{j,-1} | i_{k+1}, \dots, i_R \rangle}_{=: \phi^{k+1}} \\ &\quad - \underbrace{\sum_{\mathbf{i} \in \{0,1,2\}^{R-k}} \langle i_{k+1}, \dots, i_R | \sum_{j=1}^R \langle \psi_R^{j,-1} | \psi_R^1 | i_{k+1}, \dots, i_R \rangle}_{=: \phi^{k+1\dagger}} \\ &\quad + \underbrace{\sum_{\mathbf{i} \in \{0,1,2\}^{R-k}} \langle i_{k+1}, \dots, i_R | \sum_{j=1}^R \langle \psi_R^{j,-1} | \sum_{l=1}^R \langle \psi_R^{l,-1} | i_{k+1}, \dots, i_R \rangle}_{=: \tilde{\phi}^{k+1}} \end{aligned} \quad (3.4)$$

Properties 3.1.2. For all $j \in [\![2, N]\!]$

$$\sum_{\mathbf{i} \in \{0,1,2\}^{R-(j-1)}} \langle i_j, i_{j+1}, \dots, i_R | \psi_R^1 \rangle \langle \psi_R^1 | i_j, i_{j+1}, \dots, i_R \rangle = \alpha_{j-1} (|0\rangle + |2\rangle)_{x_1 \cdots x_{j-1}} (\langle 0 | + \langle 2 |)_{x_1 \cdots x_{j-1}} \quad (3.5)$$

Proof. The L.H.S. equals

$$\begin{aligned} \sum_{\mathbf{i} \in \{0,1,2\}^{R-(j-1)}} (|0\rangle + |2\rangle)_{x_1 \cdots x_{j-1}} \langle i_j | (|0\rangle + |2\rangle) \langle i_{j+1} | (|0\rangle + |2\rangle) \cdots \langle i_R | (|0\rangle + |2\rangle) (\cdot)^\dagger \\ = \alpha_{j-1} (|0\rangle + |2\rangle)_{x_1 \cdots x_{j-1}} (\langle 0 | + \langle 2 |)_{x_1 \cdots x_{j-1}} \end{aligned}$$

\square

Properties 3.1.3. For all $k \in [\![2, N]\!]$,

$$\phi^k = \alpha_{k-1} (|0\rangle + |2\rangle)_{x_1 \cdots x_{k-1}} \left(\sum_{j=1}^{k-1} \langle \psi_{k-1}^{j,-1} | \right)^\dagger \quad (3.6)$$

Proof.

$$\begin{aligned} \phi^k = & \sum_{\mathbf{i} \in \{0,1,2\}^{N-(k-1)}} \langle i_k \cdots | \psi_N^1 \rangle \langle \psi_N^{1,-1} | i_k \cdots \rangle + \sum_{\mathbf{i} \in \{0,1,2\}^{N-(k-1)}} \langle i_k \cdots | \psi_N^1 \rangle \langle \psi_N^{2,-1} | i_k \cdots \rangle + \\ & \cdots + \sum_{\mathbf{i} \in \{0,1,2\}^{N-(k-1)}} \langle i_k \cdots | \psi_N^1 \rangle \langle \psi_N^{k-1,-1} | i_k \cdots \rangle + \sum_{\mathbf{i} \in \{0,1,2\}^{N-(k-1)}} \langle i_k \cdots | \psi_N^1 \rangle \sum_{j \geq k}^N \langle \psi_N^{j,-1} | i_k \cdots \rangle \end{aligned} \quad (3.7)$$

□

where we just split $\sum_{j=1}^N = \sum_{j=1}^{k-1} + \sum_{j=k}^N$. Now $\langle i_k \cdots | \psi_N^1 \rangle = 0$ if and only if the bra contains at least one $\langle 1|$, which implies that the sums over basis states $\sum_{\mathbf{i}}$ become the sum over the basis states that have no $|1\rangle$. Moreover, for such basis elements we find:

$$\langle i_k \cdots | \psi_N^{j,-1} \rangle = \begin{cases} (|0\rangle + |2\rangle)_{x_1 \cdots x_{j-1}} |1\rangle_{x_j} (|0\rangle + |1\rangle + |2\rangle)_{x_{j+1} \cdots x_{k-1}} = |\psi_{k-1}^{j,-1}\rangle & \text{if } j \in [1, k-1] \\ 0 \text{ if } j \geq k \end{cases} .$$

Hence the last term of Eq.(3.7) is zero, which demonstrates the relation.

Properties 3.1.4.

$$\begin{aligned} \tilde{\phi}^k = & \sum_{j=1}^{k-1} |\psi_{k-1}^{j,-1}\rangle \left((\alpha_{k-1} + \beta_{k-1}) \sum_{l=1}^{k-1} \langle \psi_{k-1}^{l,-1}| + \beta_{k-1} \langle \psi_{k-1}^1 | \right) \\ & + |\psi_{k-1}^1\rangle \left(\beta_{k-1} \sum_{j=1}^{k-1} \langle \psi_{k-1}^{j,-1}| + \beta_{k-1} \langle \psi_{k-1}^1 | \right) \end{aligned} \quad (3.8)$$

Proof. In this proof, for ease of notation, one replaces $\sum_{\mathbf{i} \in \{0,1,2\}^{N-(k-1)}}$ by $\sum_{\mathbf{i}}$. By definition, one has

$$\tilde{\phi}^k = \sum_{\mathbf{i}} \sum_{j,l=1}^N \langle i_k \cdots | \psi_N^{j,-1} \rangle \langle \psi_N^{l,-1} | i_k \cdots \rangle \quad (3.9)$$

We can split the sum into 4 sectors (see Fig. 3.1) :

$$\sum_{j,l=1}^N = \sum_{j,l=1}^{k-1} + \sum_{j=1}^{k-1} \sum_{l=k}^N + \sum_{j=k}^N \sum_{l=1}^{k-1} + \sum_{j,l=k}^N$$

The first sum corresponds to the pink sector, where both indices are in the square $[1, k]^2$. The second and third sums correspond to the blue sectors, where one of the two indexs is out of the square, and the green sector where both indices are out.

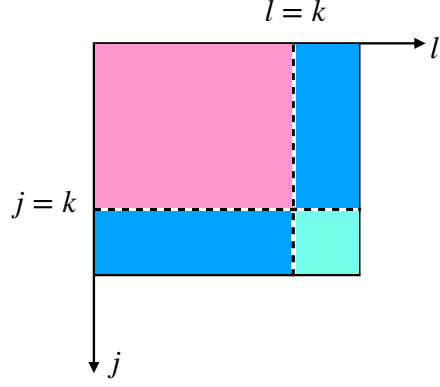


Figure 3.1: Sectors of summation over j, l at equation (3.9).

Let us call $\tilde{\phi}_{\text{pink}}^k, \tilde{\phi}_{\text{blue}}^k, \tilde{\phi}_{\text{green}}^k$, the corresponding terms of $\tilde{\phi}^k$. To compute the pink term, one needs the relation, that holds for all $j \in \llbracket 1, k-1 \rrbracket$ and all $\mathbf{i} \in \{0, 1, 2\}^{N-(k-1)}$:

$$\left\langle i_k \cdots \middle| \psi_N^{j,-1} \right\rangle = \left| \psi_{k-1}^{j,-1} \right\rangle. \quad (3.10)$$

With that relation, the pink term becomes easy to compute as

$$\tilde{\phi}_{\text{pink}}^k = (\alpha_{k-1} + \beta_{k-1}) \sum_{j,l \in \text{pink}} \left| \psi_{k-1}^{j,-1} \right\rangle \left\langle \psi_{k-1}^{l,-1} \right|. \quad (3.11)$$

To compute the blue term, one needs the relation, true for all $l \in \llbracket k, N \rrbracket$

$$\left\langle i_k \cdots \middle| \psi_N^{l,-1} \right\rangle = \begin{cases} (|0\rangle + |2\rangle)_{x_1 \cdots x_{k-1}} & \text{if } \exists i_j = 1 \\ 0 & \text{otherwise} \end{cases} \quad (3.12)$$

and so

$$\begin{aligned} \tilde{\phi}_{\text{blue}}^k &= \sum_{\mathbf{i} \mid \exists i_j = 1} \left[\sum_{j=1}^{k-1} \left| \psi_{k-1}^{j,-1} \right\rangle (\langle 0| + \langle 2|)_{x_1 \cdots x_{k-1}} + \sum_{l=1}^{k-1} (|0\rangle + |2\rangle)_{x_1 \cdots x_{k-1}} \left\langle \psi_{k-1}^{j,-1} \right| \right] \\ &= \beta_{k-1} \left[\sum_{j=1}^{k-1} \left| \psi_{k-1}^{j,-1} \right\rangle (\langle 0| + \langle 2|)_{x_1 \cdots x_{k-1}} + \sum_{l=1}^{k-1} (|0\rangle + |2\rangle)_{x_1 \cdots x_{k-1}} \left\langle \psi_{k-1}^{j,-1} \right| \right] \\ &= \beta_{k-1} \left[\sum_{j=1}^{k-1} \left| \psi_{k-1}^{j,-1} \right\rangle \langle \psi_{k-1}^1 | + \sum_{l=1}^{k-1} |\psi_{k-1}^1 \rangle \left\langle \psi_{k-1}^{j,-1} \right| \right]. \end{aligned} \quad (3.13)$$

Finally, the green term is

$$\begin{aligned} \tilde{\phi}_{\text{green}}^k &= \sum_{\mathbf{i}} \sum_{j,l \in \text{green}} \left\langle i_k \cdots \middle| \psi_N^{j,-1} \right\rangle \left\langle \psi_N^{j,-1} \middle| i_k \cdots \right\rangle \\ &= \sum_{\mathbf{i} \mid \exists i_j = 1} \sum_{j,l \in \text{green}} \left\langle i_k \cdots \middle| \psi_N^{j,-1} \right\rangle \left\langle \psi_N^{j,-1} \middle| i_k \cdots \right\rangle \\ &= \beta_{k-1} (|0\rangle + |2\rangle)_{x_1 \cdots x_{k-1}} (\langle 0| + \langle 2|)_{x_1 \cdots x_{k-1}} \\ &= \beta_{k-1} |\psi_{k-1}^1 \rangle \langle \psi_{k-1}^1|. \end{aligned} \quad (3.14)$$

Then, by summing the green, pink, and blue parts, one obtains

$$\begin{aligned}\tilde{\phi}^k = & (\alpha_{k-1} + \beta_{k-1}) \sum_{j,l \in \text{pink}} |\psi_{k-1}^{j,-1}\rangle \langle \psi_{k-1}^{l,-1}| + \beta_{k-1} \left[\sum_{j=1}^{k-1} |\psi_{k-1}^{j,-1}\rangle \langle \psi_{k-1}^1| + \sum_{l=1}^{k-1} |\psi_{k-1}^1\rangle \langle \psi_{k-1}^{j,-1}| \right] \\ & + \beta_{k-1} |\psi_{k-1}^1\rangle \langle \psi_{k-1}^1|\end{aligned}\quad (3.15)$$

□

Properties 3.1.5.

$$\hat{\rho}_{x_1 \dots x_k} = (\alpha_k - \beta_k) |\psi_k^{\text{cantor}}\rangle \langle \psi_k^{\text{cantor}}| + 2\beta_k \left(|\psi_k^1\rangle \langle \psi_k^1| + \sum_{j,l=1}^k |\psi_k^{j,-1}\rangle \langle \psi_k^{j,-1}| \right) \quad (3.16)$$

Proof. Using the propositions (3.1.2),(3.1.3),(3.8), and Eq.(3.4), one obtains

$$\begin{aligned}\hat{\rho}_{x_1 \dots x_k} = & \alpha_k |\psi_k^1\rangle \langle \psi_k^1| - \phi^{k+1} - (\phi^{k+1})^\dagger + \tilde{\phi}^{k+1} \\ = & \alpha_k |\psi_k^1\rangle \langle \psi_k^1| - \alpha_k |\psi_k^1\rangle \sum_{j=1}^k |\psi_k^{j,-1}| - \alpha_k \sum_{j=1}^k |\psi_k^{j,-1}\rangle \langle \psi_k^1| \\ & + (\alpha_k + \beta_k) \sum_{j,l=1}^k |\psi_k^{j,-1}\rangle \langle \psi_k^{l,-1}| + \beta_k \sum_{j=1}^k |\psi_k^{j,-1}\rangle \langle \psi_k^1| + \beta_k \sum_{j=1}^k |\psi_k^1\rangle \langle \psi_k^{j,-1}| + \beta_k |\psi_k^1\rangle \langle \psi_k^1| \\ = & |\psi_k^1\rangle \left[\alpha_k \langle \psi_k^1| - \alpha_k \sum_{j=1}^k |\psi_k^{j,-1}| + \beta_k \sum_{j=1}^k |\psi_k^{j,-1}| + \beta_k \langle \psi_k^1| \right] \\ & + \sum_{j=1}^k |\psi_k^{j,-1}\rangle \left[-\alpha_k \langle \psi_k^1| + (\alpha_k + \beta_k) \sum_{l=1}^k |\psi_k^1| \right] \\ = & |\psi_k^1\rangle \left[N_k \langle \psi_k^1| + (\beta_k - \alpha_k) \sum_{j=1}^k |\psi_k^{j,-1}| \right] + \sum_{j=1}^k |\psi_k^{j,-1}\rangle \left[(\beta_k - \alpha_k) \langle \psi_k^1| + N_k \sum_{l=1}^k |\psi_k^{l,-1}| \right]\end{aligned}\quad (3.17)$$

where $N_k = \alpha_k + \beta_k$. Now, using $\alpha_k - \beta_k = 2\beta_k - N_k$,

$$\begin{aligned}\hat{\rho}_{x_1 \dots x_k} = & N_k |\psi_k^1\rangle \langle \psi_k^{\text{cantor}}| - N_k \sum_{j=1}^k |\psi_k^{j,-1}\rangle \langle \psi_k^{\text{cantor}}| \\ & + 2\beta_k \underbrace{\left[|\psi_k^1\rangle \sum_{j=1}^k |\psi_k^{j,-1}| + \sum_{j=1}^k |\psi_k^{j,-1}\rangle \langle \psi_k^1| \right]}_{-|\psi_k^{\text{cantor}}\rangle \langle \psi_k^{\text{cantor}}| + |\psi_k^1\rangle \langle \psi_k^1| + \sum_{j,l=1}^k |\psi_k^{j,-1}\rangle \langle \psi_k^{l,-1}|} \\ & - |\psi_k^{\text{cantor}}\rangle \langle \psi_k^{\text{cantor}}| + |\psi_k^1\rangle \langle \psi_k^1| + \sum_{j,l=1}^k |\psi_k^{j,-1}\rangle \langle \psi_k^{l,-1}|\end{aligned}\quad (3.18)$$

Now, let us find the matrix representation of $\hat{\rho}_{x_1 \dots x_k}$. For that, one uses Eq.(3.17). Let us define

$$\{|\chi_i^k\rangle\} := \{|i_1, \dots, i_k\rangle, i_j \in \{0, 2\}\} \quad (3.19)$$

as a tensorial product state of k states, $|0\rangle$ or $|2\rangle$. Also, define $|\xi_i^k\rangle$ as a tensorial product state containing a $|1\rangle$ at some position, only $|0\rangle$ or $|2\rangle$ before, and $|0\rangle$ or $|1\rangle$ or $|2\rangle$ after, such that

$$\sum_{j=1}^k |\psi_k^{j,-1}\rangle = \sum_{j=1}^k |\psi_{j-1}^1\rangle |1\rangle_{x_j} \sum_{\mathbf{i} \in \{0,1,2\}^{N-j}} |i_{j+1}, \dots, i_k\rangle = \sum_{i=1}^{3^k - 2^k} |\xi_i^k\rangle. \quad (3.20)$$

Then, the basis of $\mathbb{H}_{x_1 \dots x_k}$ is

$$\mathbb{H}_{x_1 \dots x_k} \propto \left\{ |\chi_i^k\rangle ; i = 1, \dots, 2^k \right\} \cup \left\{ |\xi_i^k\rangle ; i = 1, \dots, 3^k - 2^k \right\}. \quad (3.21)$$

Put in words, a basis of the Hilbert space corresponding to scales x_1, \dots, x_k consists of the union of a basis made of tensorial product state containing at least one $|1\rangle$, and a basis containing only $|0\rangle$ and $|2\rangle$. The first basis corresponds to the black states and the second basis to the white states that do not belong to a cantor segment. These two sub-spaces are orthogonal, and hence it becomes easy to compute the matrix elements of the reduced density operator in this representation. One has, using Eq. (3.17)

$$\langle \xi_i^k | \hat{\rho}_{x_1 \dots x_k} = (\beta_k - \alpha_k) \langle \psi_k^1 | + N_k \sum_{l=1}^k \langle \psi_k^{l,-1} |, \quad (3.22)$$

and so

$$\langle \xi_i^k | \hat{\rho}_{x_1 \dots x_k} | \chi_j^k \rangle = \beta_k - \alpha_k, \quad (3.23)$$

$$\langle \xi_i^k | \hat{\rho}_{x_1 \dots x_k} | \xi_j^k \rangle = N_k. \quad (3.24)$$

One has also

$$\langle \chi_i^k | \hat{\rho}_{x_1 \dots x_k} = N_k \langle \psi_k^1 | + (\beta_k - \alpha_k) \sum_{j=1}^k \langle \psi_k^{j,-1} |, \quad (3.25)$$

and so

$$\langle \chi_i^k | \hat{\rho}_{x_1 \dots x_k} | \chi_j^k \rangle = N_k, \quad (3.26)$$

$$\langle \chi_i^k | \hat{\rho}_{x_1 \dots x_k} | \xi_j^k \rangle = \beta_k - \alpha_k. \quad (3.27)$$

Hence, the matrix representation of the reduced density operator is

$$\begin{array}{cc} \{|\chi_i^k\rangle\} & \{|\xi_i^k\rangle\} \\ \begin{pmatrix} N_k A_k & (\beta_k - \alpha_k) B_k \\ (\beta_k - \alpha_k) B_k^T & N_k C_k \end{pmatrix} & \begin{pmatrix} \{|\chi_i^k\rangle\} \\ \{|\xi_i^k\rangle\} \end{pmatrix} \end{array}$$

□

We finally obtain the form of the analytical reduced density matrix of the quantum Cantor set.

Properties 3.1.6.

$$\rho_{x_1 \dots x_k} = \begin{pmatrix} (\alpha_k + \beta_k)A_k & (\beta_k - \alpha_k)B_k \\ (\beta_k - \alpha_k)B_k^T & (\alpha_k + \beta_k)C_k \end{pmatrix} \in \mathbb{R}^{3^k \times 3^k}, \quad (3.28)$$

where A_k, B_k, C_k are matrices where each entry equals 1 and their dimensions are

$$A_k \in \mathbb{R}^{2^k \times 2^k}, \quad B_k \in \mathbb{R}^{(3^k - 2^k) \times 2^k}, \quad C_k \in \mathbb{R}^{(3^k - 2^k) \times (3^k - 2^k)}. \quad (3.29)$$

This matrix is real and symmetric and clearly has a rank 2 since it has 2 linearly independent rows. This means that the number of nonzero eigenvalues equals 2. The spectrum of the density matrix is thus given as

$$\sigma_{\rho_{x_1 \dots x_k}} = \{0, \lambda_1^k, \lambda_2^k\}, \quad \forall k \in \llbracket 1, R-1 \rrbracket. \quad (3.30)$$

The EE for several k is computed from (3.28). This requires to compute, at each k , the eigenvalues of a matrix of size $3^k \times 3^k$, for $k \in \{1, \dots, R-1\}$. Parallelly, the EE is also computed from the MPS encoding method. This is done for $R=8$ and $R=9$ and the obtained curves are plotted in Fig.3.2, where the results from the two methods show perfect agreement.

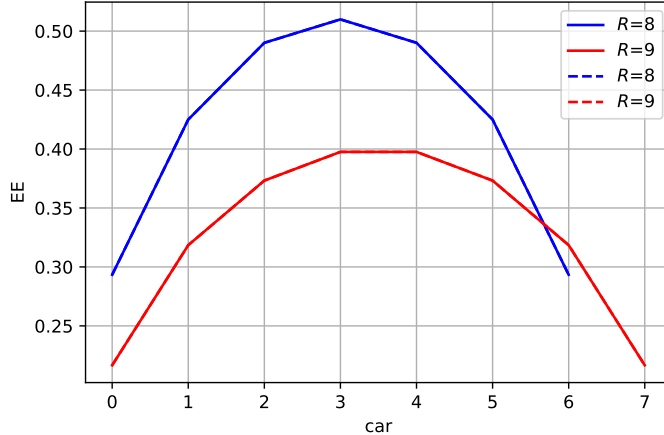


Figure 3.2: The dashed line represents the EE obtained from MPS method and the red plain line from the analytical calculation of reduced density matrix (3.28).

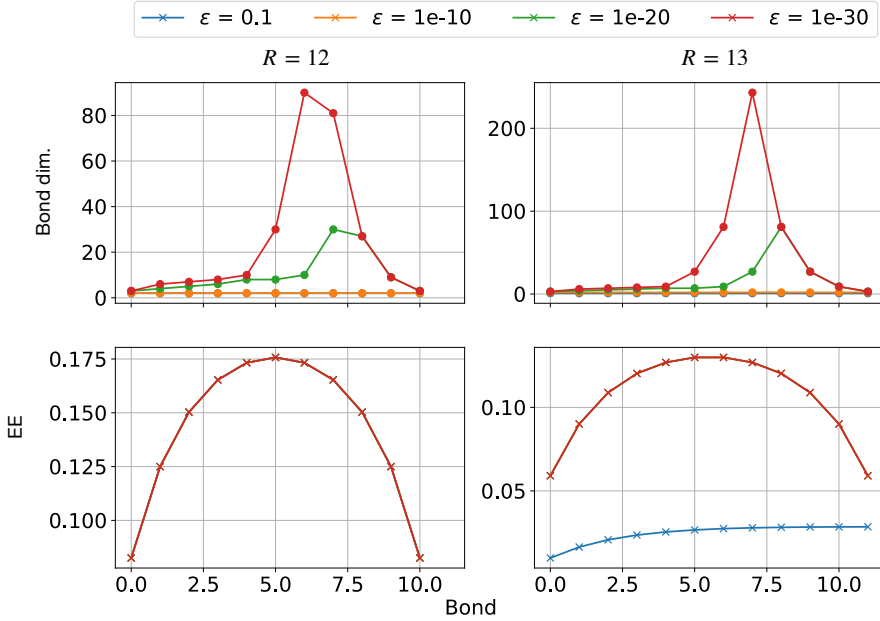


Figure 3.3: EE and bond dimension for the QCS with -1 and 1 data. The MPS parameters are $L = R$, $k = +\infty$, $d = 3$.

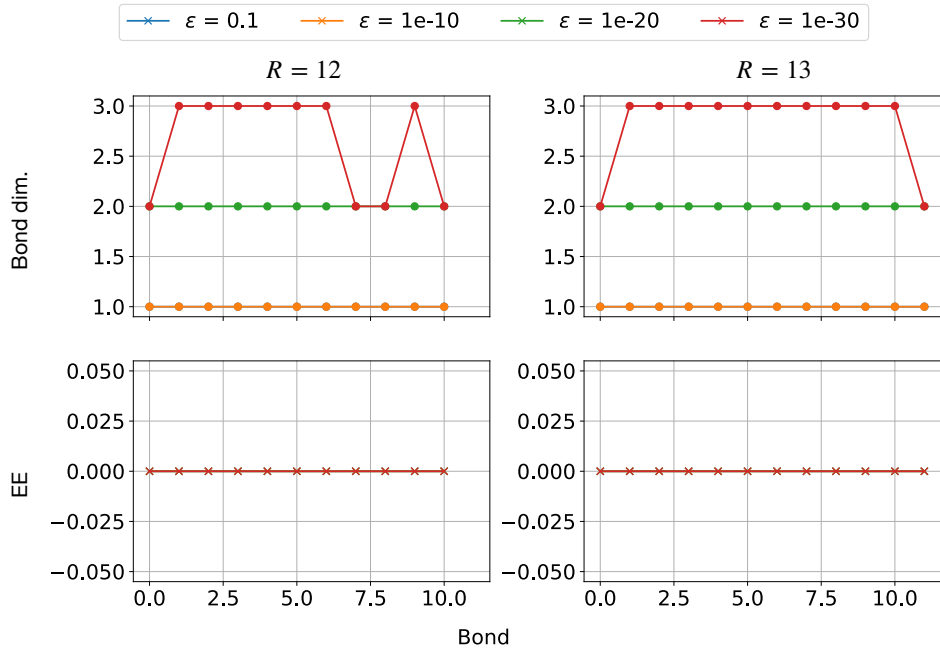


Figure 3.4: EE and bond dimension for the QCS with 0 and 1 data. The MPS parameters are $L = R$, $k = +\infty$, $d = 3$.

Facultativity of the data

We make some important remarks on the relationships between the data and the EE. The construction of the QCS at Sec. 2.2.2 was such that f_{cantor} assigned $+1$ and -1 to $\mathbb{Q}_{n=3^R}^{D=1}$. The choice of the values was rather arbitrary, and we could choose any value $a \neq b$ to discriminate the two types of segment. As it was already discussed in the example 1 of Section 2.3, the values of a and b have an impact on the resulting interscale EE and bond dimension.

Indeed, if we take instead of $+1$ and -1 , the value $a = +1$ when the segment is in the cantor set, and 0 when it is not. In this case, the QCS (2.8) becomes a simple product state

$$|\psi_R^{\text{cantor}}\rangle = |\psi_R^1\rangle = (|0\rangle + |2\rangle)_{x_1 \dots x_R} \quad (3.31)$$

and hence for any bipartition, the bond dimension is 1 and the EE is zero. For the $-1, 1$ encoding, the bond dimension was also constant, but not the EE. Numerical simulations were made, which confirm the analytical calculation : for a value of iteration $R = 12$ and $R = 13$, we computed the bond dimension and EE of the QCS for several truncation parameters ϵ . Figure 3.3 shows the result for the case where f_{cantor} assigns -1 and 1 and Fig. 3.4 for the case where f_{cantor} assigns 0 and 1 . Because QCS is simple enough, is intuitive to understand why it affects the EE. When assigning zero to a segment not in the cantor set, the QCS ignores these element, since they are multiplied by zero, and the QCS structure becomes perfectly self-similar. If they are assigned the value -1 , then the QCS is not perfectly self-similar because of the middle segment.

Finding optimal encoding

Regarding the previous discussion, consider the coefficient $c_{x_1 \dots x_R}$ of the QCS. Consider a bond $(x_1 \dots y_i \mid x_{i+1} \dots y_R)$ and denote $x \in X$ the left indices and $y \in Y$ the right indices. Consider the affine transformation

$$f(x, y) \rightarrow af(x, y) + b =: f^{a,b}(x, y) \quad (3.32)$$

Passing from a $0, +1$ to $-1, +1$ assignment can be encoded by this transformation by choosing $a = 2$ and $b = -1$. But more generally, in this parameterized form, we can now choose the values a and b that minimize the EE. However, minimizing the Von Neuman Entanglement entropy can be difficult, so one can instead minimize the Reany-2 entanglement entropy, defined as

$$S_2(a, b) = -\log \left[\frac{\text{Tr}_X(\rho_X^2)}{(\text{Tr}_X(\rho_X))^2} \right] \quad (3.33)$$

where the argument of the logarithm is called the *purity*, which can be written

$$\mathbb{P}(a, b) = \frac{\sum_{xx'yy'} f^{a,b}(x, y) f^{a,b}(x, y') f^{a,b}(x', y') f^{a,b}(x', y)}{\left(\sum_{xy} f^{a,b}(x, y)^2 \right)} \quad (3.34)$$

Instead, the Reany-2 entanglement entropy is believed to behave as $\log(\text{bond dimension})$ [27], which constitutes an upper bound on the Von Neuman EE. So by finding a, b that verify

$$\frac{\partial \mathbb{P}(a, b)}{\partial a \partial b} = 0 \quad (3.35)$$

we can encode the data such that the EE is minimal.

3.1.2 Self-similar objects

Consider some data on $\mathbb{Q}_{n=q^R}^D$ and the quantum state $|\psi\rangle$ associated with the RSTTF of that data. Experiencing the above QCS case, we want to understand further how the self-similarity of such data is represented in the quantum state. We aim to derive some property of inter-scale EE and bond dimension on a totally general self-similar object.

We will do the calculation for a 2D snapshot, while the discussion generalizes easily to higher dimension D .

Definition 3.1.1 (Self-similarity). A snapshot data on $\mathbb{Q}_{n=q^R}^{D=2}$ is self-similar at scale $x_1y_1 \cdots x_iy_i$ (or $x_1y_1 \cdots x_i$) if zooming at that scale¹, the data looks the same for all possible values of base q digits of that scale.

Example. Consider the snapshot in Fig. 3.5 of size $2^3 \times 2^3$, $q = 2$. It is made of assembling a 2×2 snapshot so it is self-invariant at scale $x_1y_1 \cdots x_{R-1}y_{R-1}$.

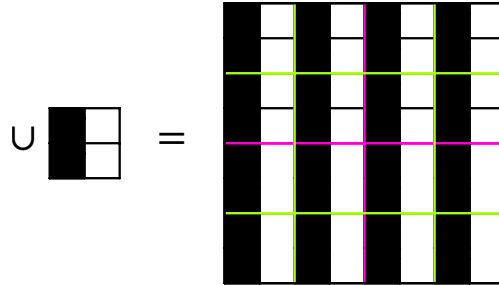


Figure 3.5

The next proposition shows how the self-invariant property translates very beautifully to the quantum word.

Properties 3.1.7. (Self-similarity in the quantum world.) A snapshot data on $\mathbb{Q}_{n=q^R}^{D=2}$ is self-similar at scale $(x_1y_1 \cdots x_iy_i)$ (or $(x_1y_1 \cdots x_i)$) if and only if the quantum state associated with the RSTTF can be written as

$$|\psi_i^{\text{self s.}}\rangle = \left[\otimes_{k=1}^{L_i} (|0\rangle + \cdots + |q-1\rangle) \right] \otimes \left(\sum_{x_{i+1}(y_i) \cdots y_R} \psi_{x_{i+1}(y_i) \cdots y_R} |x_{i+1}(y_i) \cdots y_R\rangle \right), \quad (3.36)$$

where L_i is the number of physical indices on the left part of the bipartition :

$$L_i = \begin{cases} 2i & \text{if } (x_1y_1 \cdots x_iy_i) \\ 2i - 1 & \text{if } (x_1y_1 \cdots x_i), \end{cases} \quad (3.37)$$

i.e. it is a product state on the scale at which it is self-similar.

¹we mean that sub-dividing the snapshot in 4 equal sub-snapshots and repeating i times, we will obtain $2^i \times 2^i$ squared sub-snapshots, and we zoom on these sub-snapshots.

Proof. We will prove the property for $(x_1y_1 \cdots x_iy_i)$ and $q = 2$ but the proof is easily generalized for $q > 2$ and $(x_1y_1 \cdots x_i)$. To prove this property, it suffices to notice that the snapshot data is self-similar at scale $(x_1y_1 \cdots x_iy_i)$ if and only if the coefficients of the quantum state verify

$$\begin{aligned}\psi_{0x_2 \cdots x_R y_R} &\equiv \psi_{1x_2 \cdots x_R y_R} \\ \psi_{01y_2 \cdots x_R y_R} &\equiv \psi_{01y_2 \cdots x_R y_R} \equiv \psi_{10y_2 \cdots x_R y_R} \equiv \psi_{11y_2 \cdots x_R y_R} \\ &\vdots \\ \psi_{x_1y_1 \cdots x_iy_i x_{i+1}y_{i+1} \cdots x_R y_R} &\text{ are the same for all } x_1y_1 \cdots x_iy_i\end{aligned}$$

The quantum state can hence be written

$$\begin{aligned}|\psi_i^{\text{self s.}}\rangle &= \sum_{x_1} \sum_{y_1} \cdots \sum_{x_R} \sum_{y_R} \psi_{x_1y_1 \cdots x_R y_R} |x_1y_1 \cdots x_R y_R\rangle \\ &= \sum_{y_1} \cdots \sum_{x_R} \sum_{y_R} \left(\underbrace{\psi_{0y_1 \cdots x_R y_R}}_{\equiv \psi_{y_1 \cdots x_R y_R}} |0y_1 \cdots x_R y_R\rangle + \underbrace{\psi_{1y_1 \cdots x_R y_R}}_{\equiv \psi_{y_1 \cdots x_R y_R}} |1y_1 \cdots x_R y_R\rangle \right) \\ &= \sum_{y_1} \cdots \sum_{x_R} \sum_{y_R} \psi_{y_1 \cdots x_R y_R} \underbrace{\left(|0y_1 \cdots x_R y_R\rangle + |1y_1 \cdots x_R y_R\rangle \right)}_{[|0\rangle + |1\rangle] \otimes |y_1 \cdots x_R y_R\rangle} \\ &= [|0\rangle + |1\rangle] \otimes \left(\sum_{y_1} \cdots \sum_{x_R} \sum_{y_R} \psi_{y_1 \cdots x_R y_R} |y_1 \cdots x_R y_R\rangle \right) \\ &= [|0\rangle + |1\rangle] \otimes \left(\sum_{x_2} \cdots \sum_{x_R} \sum_{y_R} \psi_{x_2 \cdots x_R y_R} (|0x_2 \cdots x_R y_R\rangle + |1x_2 \cdots x_R y_R\rangle) \right) \\ &= \left[\otimes_{k=1}^2 (|0\rangle + |1\rangle) \right] \otimes \left(\sum_{x_2} \cdots \sum_{x_R} \sum_{y_R} \psi_{x_2 \cdots x_R y_R} |x_2 \cdots x_R y_R\rangle \right) \\ &\vdots \\ &= \left[\otimes_{k=1}^{2i} (|0\rangle + |1\rangle) \right] \otimes \left(\sum_{x_{i+1}y_{i+1} \cdots y_R} \psi_{x_{i+1}y_{i+1} \cdots x_R y_R} |x_{i+1}y_{i+1} \cdots x_R y_R\rangle \right).\end{aligned}$$

□

For the state to be normalized as $\langle \psi_i^{\text{self s.}} | \psi_i^{\text{self s.}} \rangle = 1$, the coefficients must fulfill,

$$q^{2i} \sum_{x_{i+1} \cdots y_R} |\psi_{x_{i+1} \cdots y_R}|^2 = 1. \quad (3.38)$$

Now that we understand how the quantum state of the RSTTF is expressed for self-similar objects, let us explore some interesting features related to the inter-scale bond dimension and entanglement entropy (EE).

With the proposition mentioned earlier (Prop.2.3.1), we naturally expect the bond dimension to remain constant across the self-similar scale- i . However, to ensure clarity, we will use density matrices to formally prove this.

Once we establish the constancy of the bond dimension, our next step is to express the inter-scale EE associated with these bonds. By keeping it straightforward and clear, we aim to unveil the nature of entanglement between different scales.

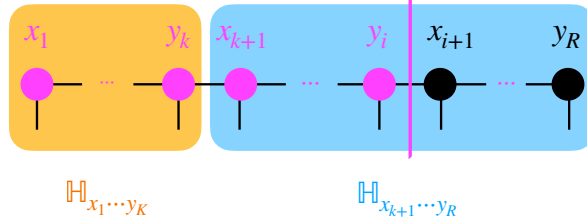


Figure 3.6: Bipartition of the Hilbert space where $|\psi_i^{\text{self s.}}\rangle$ live, at a bond belonging to self-similar scale $(x_1 \dots y_i)$ into orange and blue part. The magenta vertical line bipartite the space into self-similar scales and non-self-similar one.

Properties 3.1.8. (Bond dimension on self similar scale.) Consider the self similar snapshot data $|\psi\rangle_i^{\text{self s.}}$ on $\mathbb{Q}_{n=q^R}^{D=2}$, at scale $(x_1y_1 \dots x_iy_i)$. Let $1 \leq k < i$ be a bond that belong to the self-similar scale $(x_1y_1 \dots x_iy_i)$, that induces the bipartition $\mathbb{H}_A = \mathbb{H}_{x_1 \dots y_k}$ and $\mathbb{H}_B = \mathbb{H}_{x_{k+1} \dots y_i x_{i+1} \dots y_R}$ (see Fig. 3.6). The reduced density matrix of A is

$$\rho_{x_1 \dots y_k} = q^{-2k} \begin{bmatrix} 1 & 1 & \cdots & 1 \\ 1 & 1 & \cdots & 1 \\ \vdots & \vdots & \ddots & \vdots \\ 1 & 1 & \cdots & 1 \end{bmatrix} \in \mathbb{R}^{q^{2k} \times q^{2k}} \quad (3.39)$$

and for the bipartition $\mathbb{H}_{x_1 \dots x_k} \otimes \mathbb{H}_{y_k \dots y_R}$ it is

$$\rho_{x_1 \dots x_k} = q^{-2k+1} \begin{bmatrix} 1 & 1 & \cdots & 1 \\ 1 & 1 & \cdots & 1 \\ \vdots & \vdots & \ddots & \vdots \\ 1 & 1 & \cdots & 1 \end{bmatrix} \in \mathbb{R}^{q^{2k-1} \times q^{2k-1}}, \quad (3.40)$$

So the bond dimension is constant over the self-similar bonds.

Proof. The reduced density matrix of A is

$$\hat{\rho}_{x_1 \dots y_k} = \sum_{x_{k+1} \dots y_R} \langle x_{k+1} \dots y_R | \psi_i^{\text{self s.}} \rangle \langle \psi_i^{\text{self s.}} | x_{k+1} \dots y_R \rangle.$$

With Fig. 3.6 it is easy to see that

$$\langle x_{k+1} \dots y_R | \psi \rangle = \left[\otimes_{k=1}^{2k} (|0\rangle + \dots + |q\rangle) \right] \psi_{x_{i+1} \dots y_R},$$

so the reduced density matrix becomes

$$\begin{aligned} \rho_{x_1 \dots y_k} &= \sum_{x_{k+1} \dots y_R} |\psi_{x_{i+1} \dots y_R}|^2 \left[\otimes_{k=1}^{2k} (|0\rangle + \dots + |q\rangle) \right] \left[\otimes_{k=1}^{2k} (\langle 0| + \dots + \langle q|) \right] \\ &= \left[\otimes_{k=1}^{2k} (|0\rangle + \dots + |q\rangle) \right] \left[\otimes_{k=1}^{2k} (\langle 0| + \dots + \langle q|) \right] \underbrace{\sum_{x_{k+1} \dots y_R} |\psi_{x_{i+1} \dots y_R}|^2}_{q^{-2i} q^{2i-2k}} \\ &= q^{-2k} \left[\otimes_{k=1}^{2k} (|0\rangle + \dots + |q\rangle) \right] \left[\otimes_{k=1}^{2k} (\langle 0| + \dots + \langle q|) \right]. \end{aligned}$$

□

Properties 3.1.9. The interscale EE for all bond $1 \leq k < i$ (see previous proposition) is zero.

Proof. To compute the interscale EE at a bond $1 \leq k < i$, the Prop. 1.1.2 tells us that we have to compute the eigenvalues of the reduced density matrix, given by Prop. 3.1.8. For that, we need to solve the characteristic equation

$$\det(\rho_{x_1 \dots y_k} - \lambda I_{q^{2k} \times q^{2k}}) = 0$$

$$\det(\rho_{x_1 \dots y_k} - \lambda I_{q^{2k} \times q^{2k}}) = \det q^{-2k} \begin{pmatrix} 1 - q^{2k}\lambda & 1 & 1 & \dots & 1 \\ 1 & 1 - q^{2k}\lambda & 1 & \dots & 1 \\ 1 & 1 & 1 - q^{2k}\lambda & \dots & 1 \\ \vdots & \vdots & \vdots & \ddots & \vdots \\ 1 & 1 & 1 & \dots & 1 - q^{2k}\lambda \end{pmatrix}$$

where the matrix we have to compute its determinant is

$$\rho_{x_1 \dots y_k} - \lambda I_{q^{2k} \times q^{2k}} = \begin{cases} q^{-2k} - \lambda & \text{if } i = j \\ q^{-2k} & \text{otherwise} \end{cases} \quad (3.41)$$

Now, we perform the following operations, that will not change the determinant: we add the last column to all other columns:

$$\begin{aligned} c_{q^{2k}-1} &\leftarrow c_{q^{2k}-1} - c_{q^{2k}} \\ c_{q^{2k}-2} &\leftarrow c_{q^{2k}-2} - c_{q^{2k}} \\ &\vdots \\ c_1 &\leftarrow c_1 - c_{q^{2k}} \end{aligned}$$

The operation $c_i - c_{q^{2k}}$ is

$$q^{-2k} \begin{pmatrix} 1 \\ \vdots \\ 1 \\ 1 - q^{2k}\lambda \\ 1 \\ \vdots \\ 1 \end{pmatrix} - q^{-2k} \begin{pmatrix} 1 \\ \vdots \\ 1 \\ 1 - q^{2k}\lambda \end{pmatrix} = \begin{pmatrix} 0 \\ \vdots \\ 0 \\ -\lambda \\ 0 \\ \vdots \\ \lambda \end{pmatrix},$$

and so the determinant we have to compute becomes, after these operations

$$\det \begin{pmatrix} -\lambda & 0 & 0 & \dots & q^{-2k} \\ 0 & -\lambda & 0 & \dots & q^{-2k} \\ 0 & 0 & -\lambda & \dots & q^{-2k} \\ \vdots & \vdots & \vdots & \ddots & \vdots \\ \lambda & \lambda & \lambda & \dots & q^{-2k} - \lambda \end{pmatrix}, \quad (3.42)$$

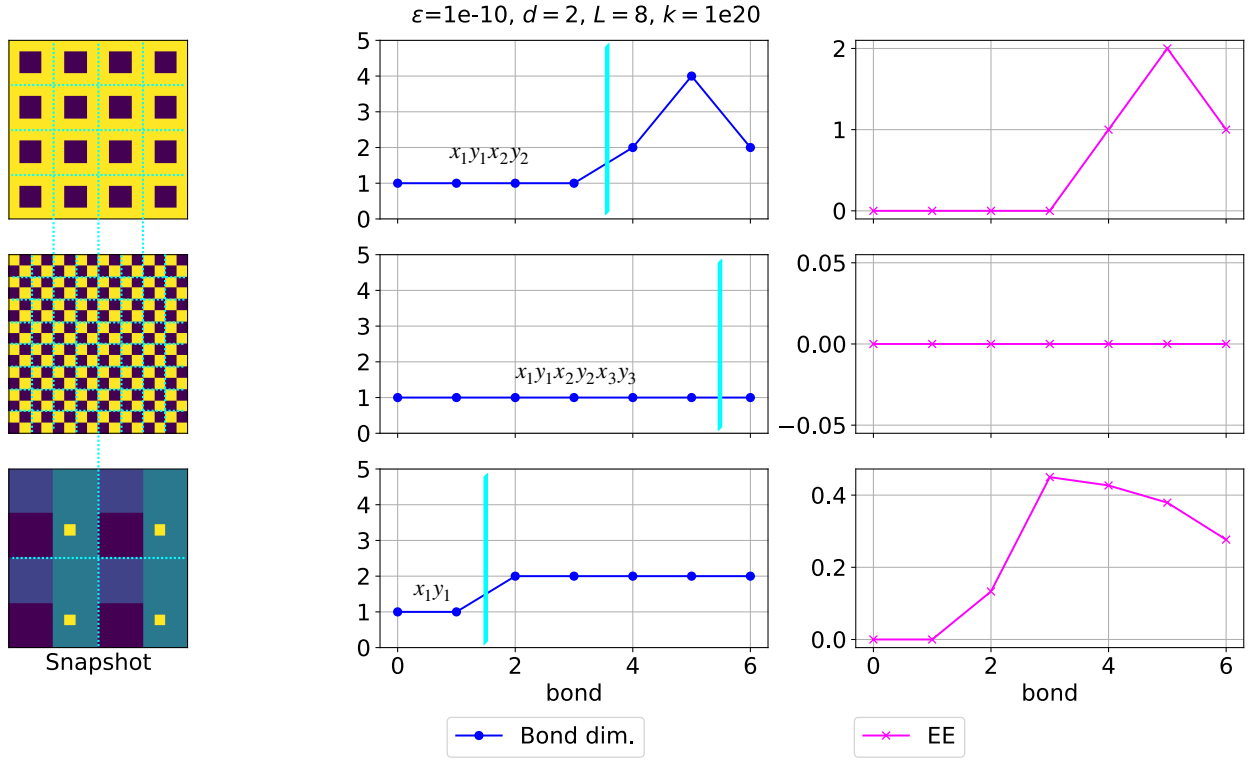


Figure 3.7: Snapshots of size $2^4 \times 2^4$. First column presents self-similar snapshots at scale (from top to down) $(x_1y_1x_2y_2)$, $(x_1y_1x_2y_2x_3y_3)$ and (x_1y_1) . The second and third column plots respectively bond dimension and EE for the snapshot of the same row. The turquoise mesh grid defines the building blocks of each snapshot.

and by adding successively every row, starting from the first, then the second, etc, to the last row, we obtain

$$\det \begin{pmatrix} -\lambda & 0 & 0 & \dots & 1 \\ 0 & -\lambda & 0 & \dots & 1 \\ 0 & 0 & -\lambda & \dots & 1 \\ \vdots & \vdots & \vdots & \ddots & \vdots \\ 0 & 0 & 0 & \dots & (1-\lambda) \end{pmatrix} = (1-\lambda)(-\lambda)^{q^{2k}-1}.$$

Hence, the spectrum is $\{1, 0\}$. The matrix has only one nonzero eigenvalue, which gives zero EE. \square

We have demonstrated rigorously that the RSTTF of data is a tool to characterize self-similar objects, and to detect at which scale the object is self-similar. Figure 3.7 shows an example of self-similar snapshots, together with bond dimension and EE. This Figure confirms our analytical treatment. On the last row, we see that the bond dimension is constant for the bonds $2, \dots, 6$, but not the EE ; for these scales, the snapshot is not self-similar. So we see that bond dimension and EE both have to be constant for the self-similar property to hold. Coming back to the QCS with a -1 and 1 encoding, it has a constant bond dimension for all bonds but not a constant EE, and in fact, this object is not self-similar in our definition.

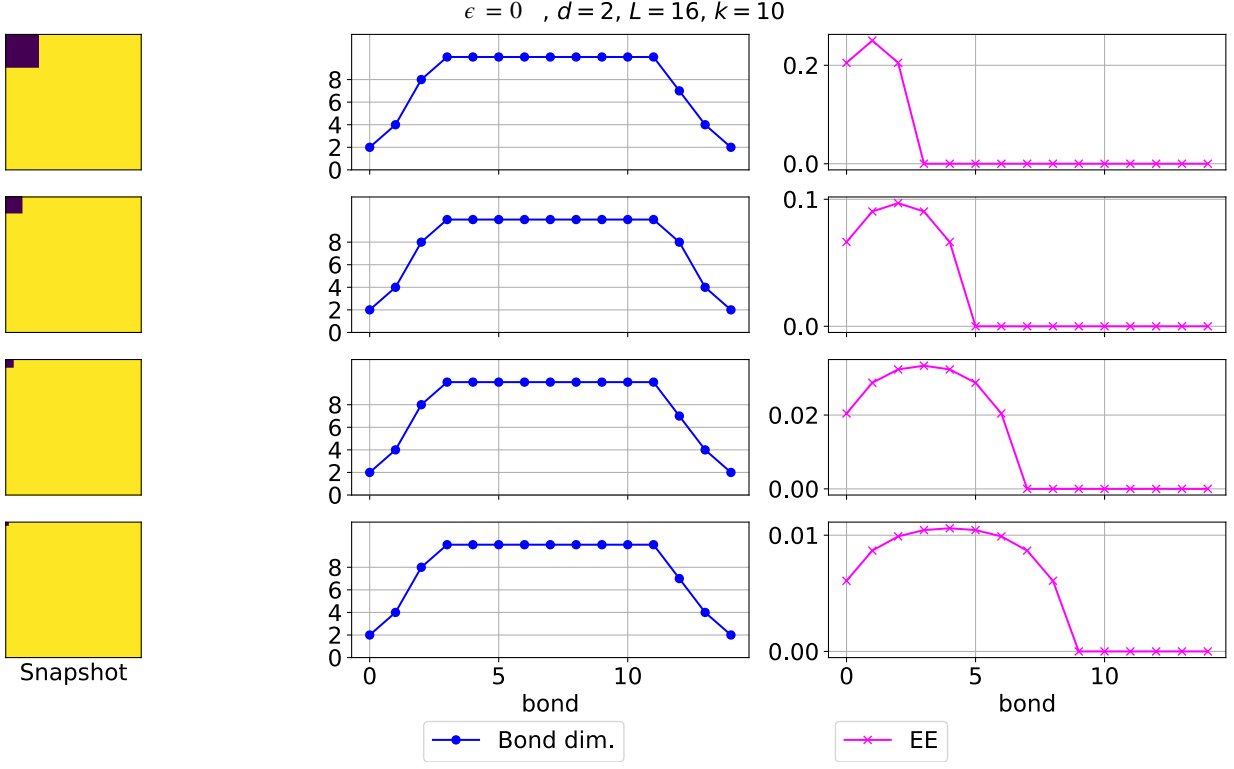


Figure 3.8: Snapshot of size $2^R \times 2^R$ with top corner having an island of +1 segment of size $2^{R-a} \times 2^{R-a}$ with $a = 1, 2, 3, 4$. The bond dimension and inter-scale EE are shown.

3.1.3 Correlation length

Given the utility of the RSTTF in dissecting scale entanglements, a pertinent question arises: Can we, using this tool, provide a basic estimate of the correlation length for a given snapshot dataset? Let us define the snapshot correlation length as the size of the bigger cluster. In a two-color setting, a cluster is an island of pixels sharing the same color.

To start the discussion, we will analyze some very simple data that shows no fluctuation at all. Figure 3.8 displays very simple snapshots of size $2^R \times 2^R$ each containing an island of +1 coefficients at the top left corner, with size varying from $2^{R-a} \times 2^{R-a}$ with $a = 1, 2, 3, 4$. The correlation lengths are the linear sizes of these islands, namely 2^{R-a} . For each snapshot, inter-scale EE and bond dimension are plotted, and we observe the following:

The position where EE attains its maximum increases as the correlation length decreases. For the first snapshot, the correlation length is 2^{R-1} , and the maximum attained at x_1 . For the second it is 2^{R-2} and maximum attained at x_2 , etc.

The EE and the bond dimension become both constant at the larger bond index, as the correlation length becomes smaller. In other words, both quantities exhibit a plateau when the bond index reaches the same certain value that yields a correlation length. For example, the plateau is attained at bond $(x_1 y_1 | \dots)$ for the first snapshot, which corresponds to a division by 4 sub snapshots, each of linear size 2^{R-1} , which is the correlation length.

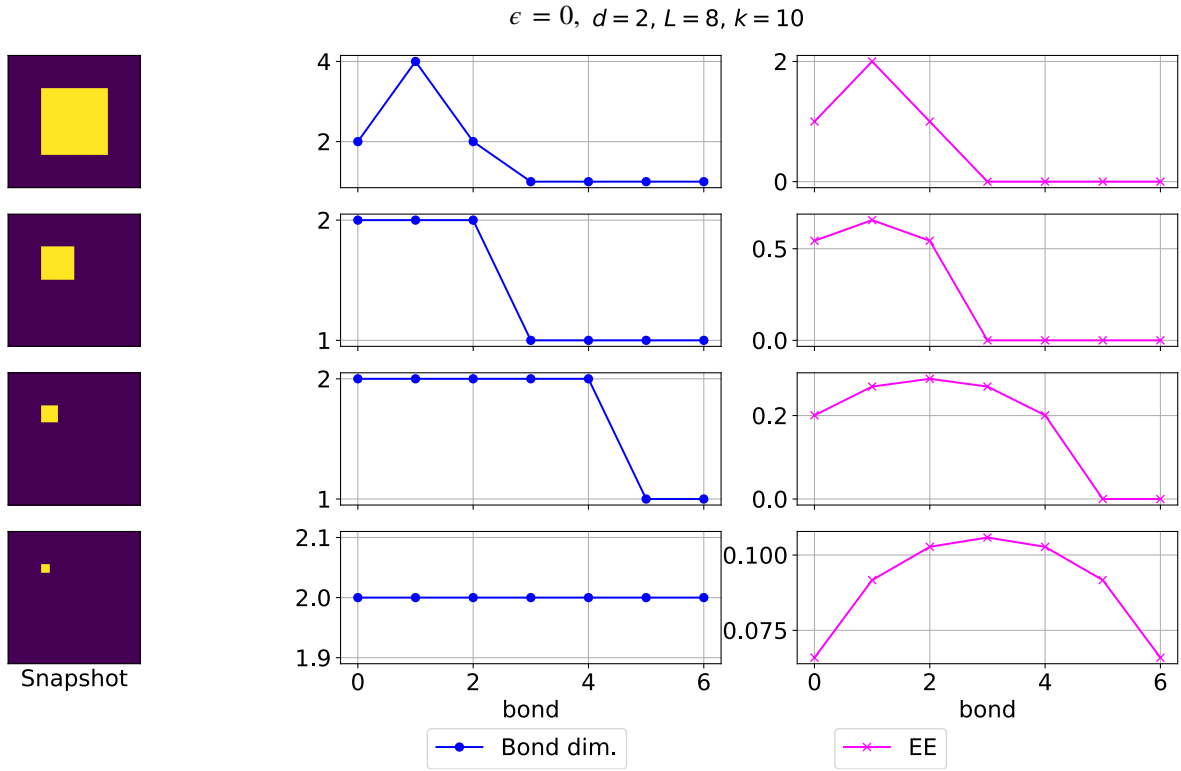


Figure 3.9: Snapshot of size $2^R \times 2^R$ with island of +1 segment of size $2^{R-a} \times 2^{R-a}$ with $a = 1, 2, 3, 4$ put at the place not exactly in the subdivision, to be compared with Fig. 3.8. The bond dimension and inter-scale EE are shown.

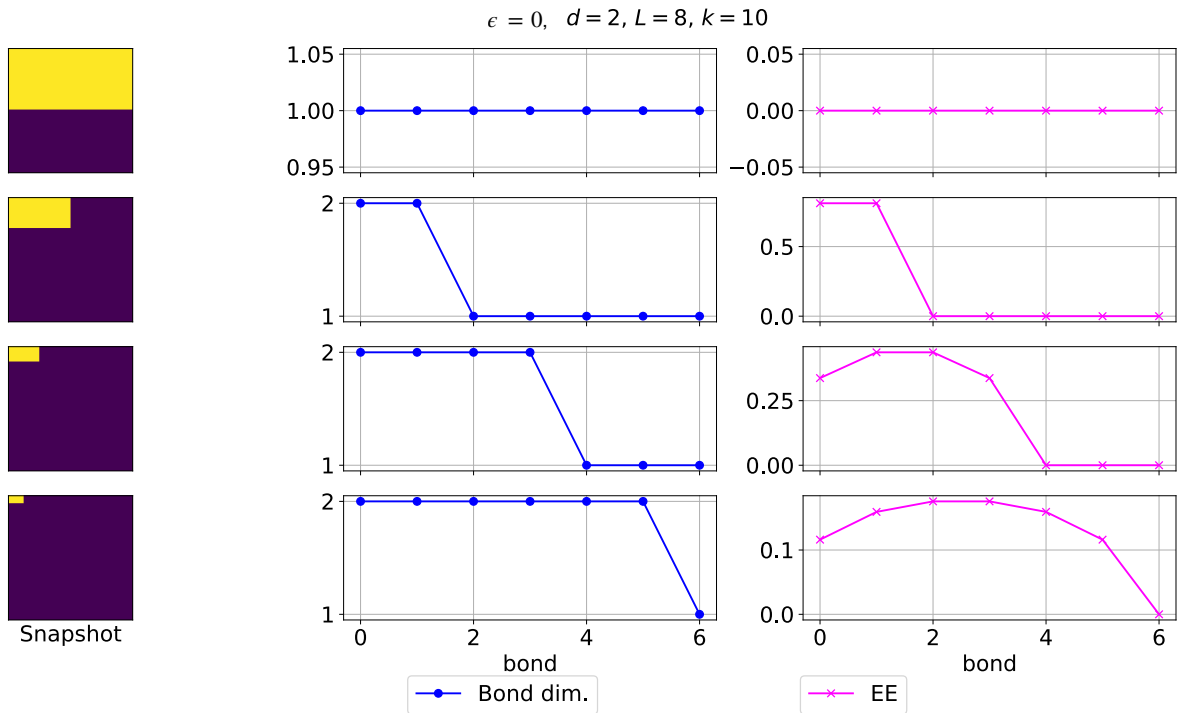


Figure 3.10: Snapshot of size $2^R \times 2^R$ with island of +1 segment of size $2^{R-a} \times 2^{R-a+1}$ with $a = 1, 2, 3, 4$ put at the place not exactly in the subdivision, to be compared with Fig. 3.8. The bond dimension and inter-scale EE are shown.

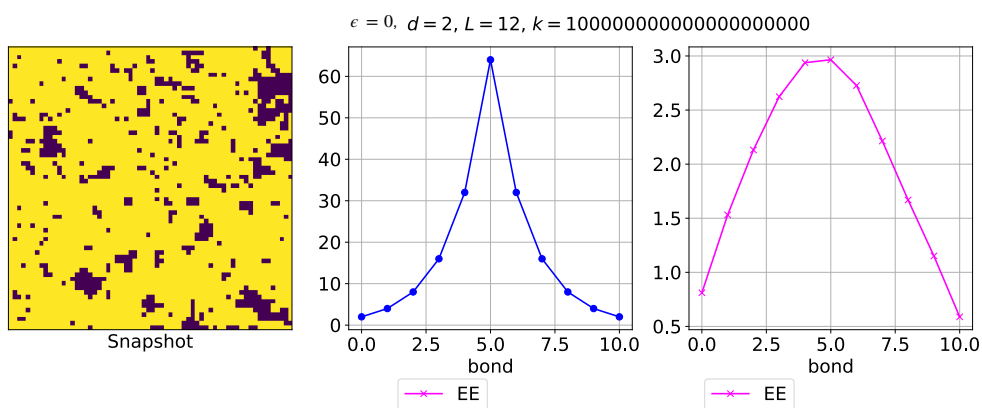


Figure 3.11: $T = 2.28$

Let us examine whether the position where EE is maximum is a good indicator of correlation length. For that, we try to move the island, such that they are not exactly positioned within a subdivision of the snapshot (Fig. 3.9). We observe two things; the correlation length (linear size of the island) remains the same, and the EE attains a maximum at a different bond for the first snapshot, while the remaining snapshots do not display a change in EE nor bond dimension. A plausible explanation is that the first snapshot contains an island that is not exactly positioned at a subdivision, in which case the EE does not detect its correlation length. Next, let us try to generate a snapshot that contains an island placed in a subdivision by 2 and not by 4 as shown in Fig. 3.10. We now find that the two cuts, (x_i) and (x_iy_i) have the same maximum EE as well as maximum bond dimension, because the y -direction has twice as large a size that keeps the color of the island the same. So analyzing these very simple snapshots, we can say that when an Island is placed at a subdivision of 2 or 4, the position at which the plateau is reached by EE and bond dimension is the linear size of that Island. Physically, we may anticipate that the size where the EE starts to decrease is the signature of the correlation length, and the maximum extends as a plateau toward the lower bond if the correlation length has a variation over different directions.

The above example was rather too simple, as the real physical systems have some complex spatial variations and the obtained snapshots will not be a smooth island in a smooth sea. For example, Fig. 3.11 shows an example of a $2^6 \times 2^6$ Ising snapshot. We see first that the snapshot is not smooth at all, because of the fluctuations, even though we can identify a small cluster ; these variations prevent the presence of a plateau and we need different ways of analyzing it.



Figure 3.12: Image taken from <https://sipi.usc.edu/database/>.

3.2 Normal image and random data

Normal images of our daily life have some inter-scale structure. Consider for example the image shown in Fig. 3.12. In this section, we want to compare these images that have spatial structure at a large-scale with completely random images ; by random we mean a snapshot where each pixel value is uniformly randomly drawn. Naturally, we expect that random snapshots are maximally entangled in the sense that each singular value matrix appearing on the MPS decomposition of the RSTTF has a lot of nonzero singular values. For the normal image, we expect that at each bond, a lot of singular values are small and so compressing does not induce a strong loss of information compared to random cases. This is because in the normal image, some structures are present, and some parts of the image are smooth ; for example in Fig. 3.12 the arms of the main character form a smooth structure. To quantitatively illustrate what we said, we compute the truncation error $e(k = +\infty, \epsilon)$ for several ϵ and the result is shown in Fig. 3.13. We see on these plots that for very big ϵ , the error is one because we lose all the information. By compressing (lowering ϵ), we see that the purple curve drops to 0.2 very quickly, whereas the blue curve drops to ~ 0.5 for a smaller ϵ . As we compress further, the error we make on the image is always smaller (except for very small values of ϵ) and drops before the random case. This is because the random image is maximally entangled, so by compressing with a ϵ , more singular values will be truncated than the normal image.

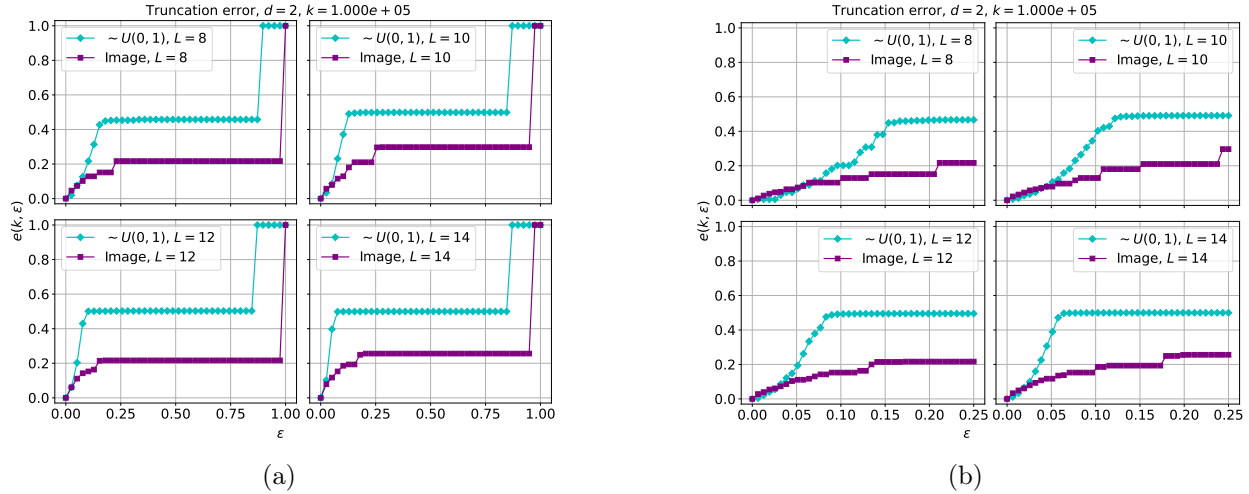


Figure 3.13: Truncation error at fixed k for the image 3.12 and a snapshot where each pixel has uniformly distributed color. Panel (b) is a zoom on panel (a).

3.3 2D Ising model on the square lattice

For a more physically realistic many-body model system, we choose the 2D classical Ising model whose most basic information related to criticality is briefly summarized in 3.3. At each temperature T , we have generated $N_s = 10$ snapshots $\{\mathbf{s}_1, \dots, \mathbf{s}_{N_s}\}$ with a zero magnetic field (Eq. 1.27), using the Monte Carlo and Wolff update method. Periodic boundary conditions are imposed, where we adopt the $L \times L$, $L = 512$ cluster which is large enough but feasible to the present analysis. We use the GitHub repository [11]. We choose an initial random configuration and start the simulation, where we can track the evolution of energy to examine whether the system reaches thermal equilibrium at that temperature. The snapshots are generated for independent runs.

In applying our framework, each spin is represented by a pixel, black or white. Each snapshot $\mathbf{s} \in \mathbb{R}^{2^R \times 2^R}$, where $2^R \times 2^R$ is the number of spins, where $R = 9$ for $L = 512$. Unless otherwise noted, the truncation parameter k is chosen to be infinity. On each sample, the MPS procedure is applied to the corresponding RSTTF.

3.3.1 Numerical analysis

Total Entanglement entropy

For the resulting MPS form, one defines the *total entanglement entropy* of the snapshot as the sum of the EE over all bonds [28],

$$S_{\text{tot}} = \sum_{j=0}^{2R-2} S_j, \quad (3.43)$$

where the j -bond indicates the bipartition, $(x_1 y_1 \dots | \dots y_R)$, where we have $(j - 1)$ variables(axes x_i or y_i) on the left-hand side of the cut. For each temperature T , we compute the average of the total EE over the N_s snapshots as $S_{\text{tot}}(T) = N_s^{-1} \sum_{i=1}^{N_s} S_{\text{tot}}^{(i)}$. For several values of R , we computed $S_{\text{tot}}(T)$ with different values of truncation.

Figure 3.14a shows the result when we attribute a white pixel 1 and a black pixel to 0, and Fig. 3.14b when -1 is attributed to black pixel.

In increasing the number of spins ($L = 2^R$) represented by R , the data becomes sharp, i.e. the variance of $S_{\text{tot}}(T)$ becomes small. Indeed, for small sizes, the number of samples average 10 is not enough. While, even for small R the temperature dependence shows a distinct feature; a sudden drop in $S_{\text{tot}}(T)$ is observed at T_c , indicating that the inter-scale correlation between snapshots increases significantly by the development of the structure.

The difference between encoding the black pixel as 0 and -1 can be viewed at the $R = 9$ panels. There is a deviation between $\epsilon = 1e^{-9}$ and 0.01 below T_c . However for $1, -1$ choices the two are coincident. This should be because below T_c the time-reversal symmetry of spin configurations is kept for $1, -1$ but not for $0, 1$. Another feature is that for $1, -1$, when taking the truncation as large as $\epsilon = 0.3$, the entropy above T_c drops to zero. It means that there are no relationships between scales. This is also due to the recovery of time-reversal symmetry of the description of the data. In that sense, the choice $1, -1$ gives a more physically meaningful choice when the object of the snapshot actually retains such symmetry.

Bond-dependence of entanglement entropy

We also computed the EE as a function of the bond index of bipartition where for each bond we averaged over N_s samples. We examined the data at several temperatures and varied the truncation parameter ϵ of the MPS. Figures 3.20a and 3.20b show the results using $0, 1$ and $-1, 1$ encoding of the data, respectively. The plots are given for two temperatures near T_c and two temperatures far away.

The bond dependence is such that the maximum value of EE at $T = 1.9$ originally located at R and its functional form is symmetric about larger and smaller bond indices. However, in approaching T_c the maximum shifts to a smaller bond index, and takes a minimum at T_c and for higher temperatures the location of the maximum increases again. This is confirmed by Fig. 3.15 where we plot the position of that maximum for different temperatures. We observe that in a narrow window around T_c , the value changes from 8 to 7. The physical implication may be such that the snapshot develops a spatial structure with the most inter-scale correlation near T_c but away from T_c it becomes either fully disordered (at high T) or uniform (at low T).

We performed the kernel regression method [29],[30],[31] on the total EE data for the $-1, 1$ encoding. It is a machine learning technique used to estimate data without accurately setting the functional form. This method is useful when we have several datasets with substantial errors but show an apparent structure, while the functional form is not necessarily analytically obtained.

The obtained data is automatically given a derivative as a function of temperature by construction, and we can extract the maximum of the derivative from the analysis. The result is shown in Fig. 3.16. From these values, one can extract the critical temperature estimations, which are shown in Tab. 3.2. As the system size increases and the compression parameter decreases, we approach the value $T_c = 2.269$, confirming that this method can accurately estimate the critical temperature.

In Figure 3.20b, the turquoise curve represents the mean EE for $\epsilon = 0.1$, where we observe that it becomes a plateau at bond 4 for low temperature, at bond 9 near critical temperature, and then this bond position increases as the temperature increases.

To better understand this behavior, we plot in Fig. 3.17 the real space data after compression with $\epsilon = 0.1$ at the 4 temperatures present in 3.20b. At $T = 1.9$, the compressed data presents some islands of size $2^{R-1} \times 2^{R-1}$ in blue color. With the discussion in Section 3.1.3 in mind, it

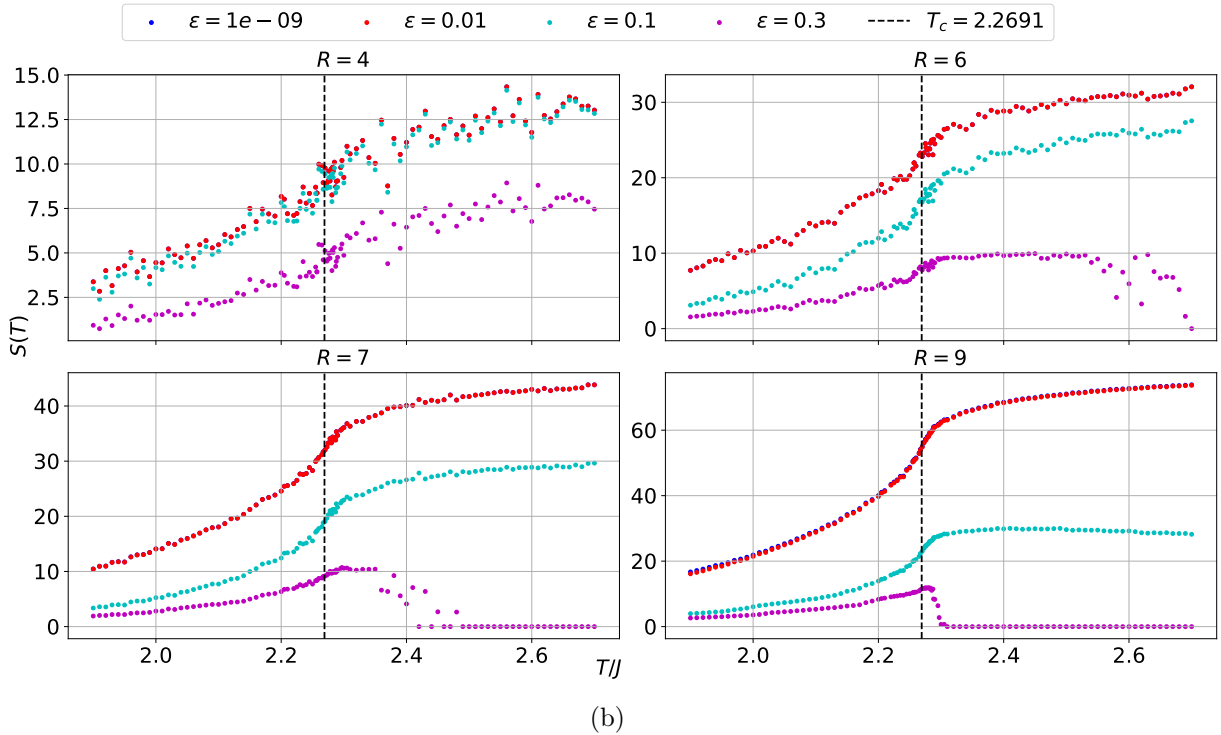
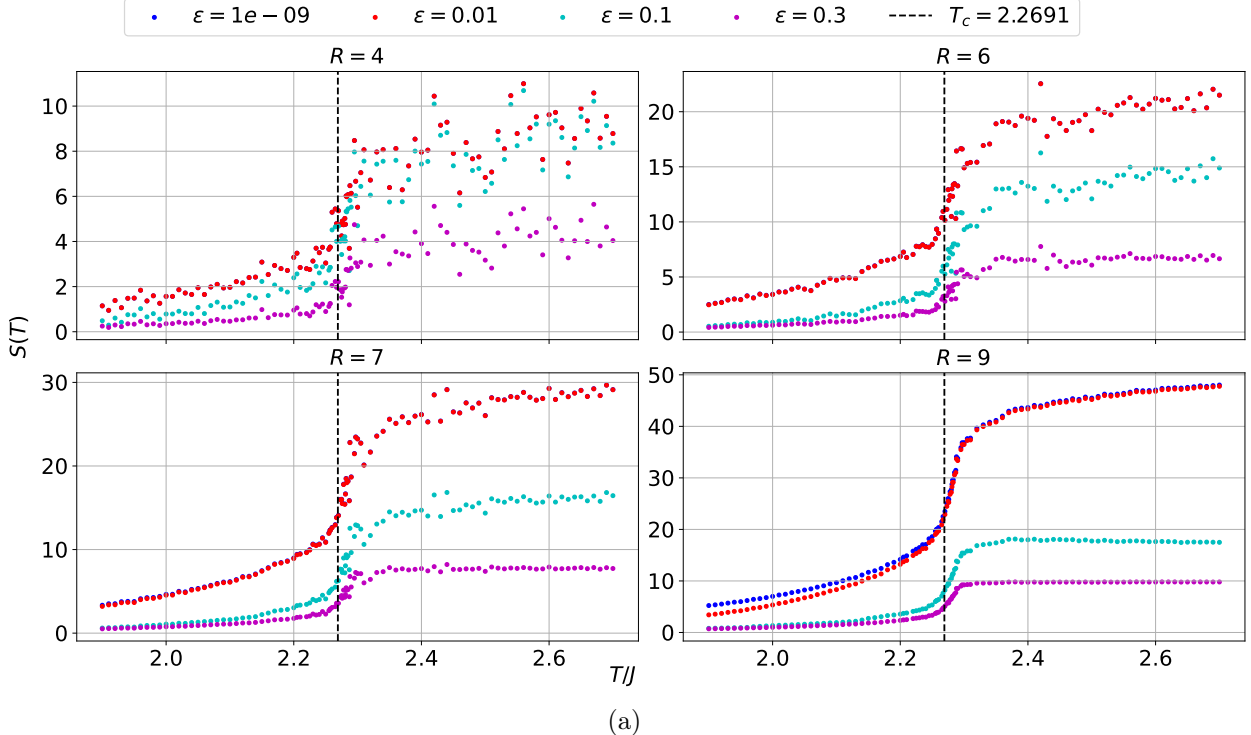


Figure 3.14: Total EE averaged over $N_s = 10$ MC samples of 2D Ising model with zero magnetic field at several T . Each panel corresponds to a value of R , where $2^R \times 2^R$ is the system size. Several truncation parameters ϵ of the MPS are plotted. Panel (a) corresponds to attributing the value 0 to the black pixel and 1 to the white pixel. Panel (b) corresponds to giving a value -1 instead of 0 to black pixel.

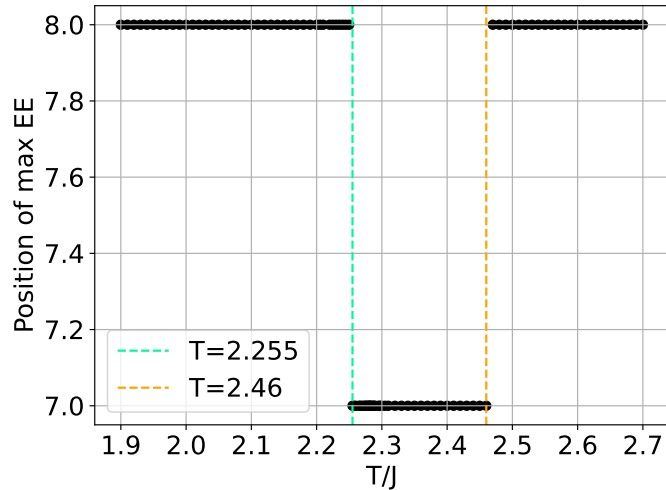


Figure 3.15: Position where EE averaged over 10 samples attains its maximum, as a function of T . In the numerical treatment, the first bond is at zero.

Table 3.1: Data

R	ϵ	T_c
4	0.00	2.22900000
4	0.01	2.23000000
4	0.10	2.23400000
4	0.30	2.27000000
6	0.00	2.26600000
6	0.01	2.26600000
6	0.10	2.27100000
6	0.30	2.26800000
7	0.00	2.26600000
7	0.01	2.26400000
7	0.10	2.26600000
7	0.30	2.27800000
9	0.00	2.26900000
9	0.01	2.26900000
9	0.10	2.26100000

Table 3.2: Table of the estimated critical temperature obtained by finding the maximum of the derivative of the total EE using the kernel regression method. This method is applied on the data for different system size R , different truncation parameter ϵ .

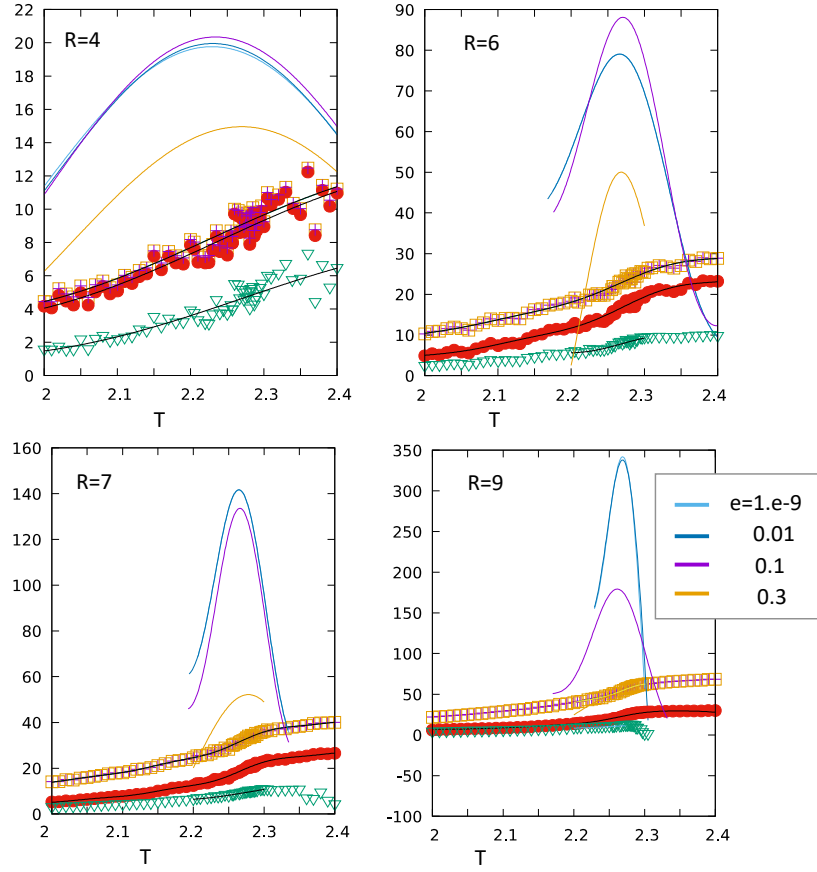


Figure 3.16: Kernel regression method to compute derivative of total EE : plain lines are the kernel regression data of the total EE, lines on the top are the derivatives of the total EE.

makes sense that the Entanglement Entropy (EE) starts a plateau at bond 4. However, the original snapshot does not contain islands of these sizes. At the two middle temperatures, we observe that structures/islands are present in both the original and compressed snapshots, explaining the presence of plateaus.

Why is the plateau for $T = 2.265$ larger than the one for $T = 2.35$? One explanation could be that in the first snapshot, the largest smooth structure (light green) is larger than the smooth structure at $T = 2.35$ (which appears darker).

At $T = 2.7$, some smaller islands are still present and are distributed uniformly in the snapshot, both in compressed and uncompressed form, as illustrated by a small plateau.

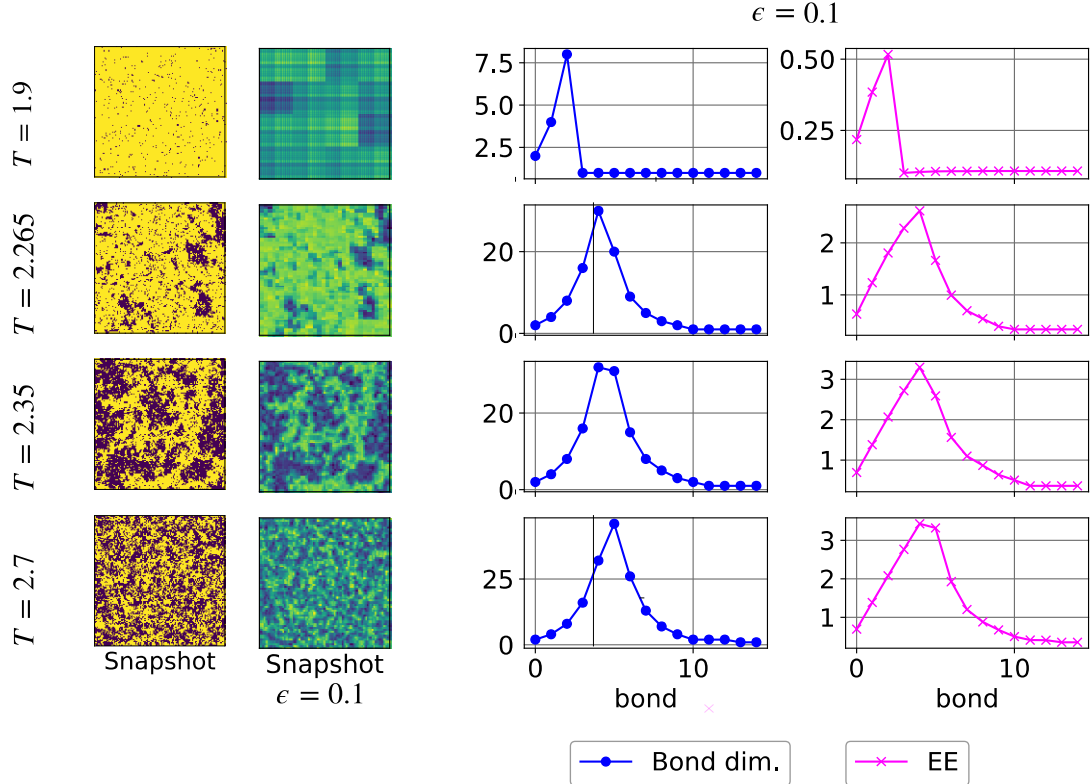


Figure 3.17: Ising snapshot with no compression (first column) and after compression (second column) at 4 temperatures. System size is $2^8 \times 2^8$.

To compare the behavior of EE and bond dimension as the temperature is varied, we plotted in Fig. 3.21 the mean EE and mean bond dimension for several temperatures on the same panel, where we chose three different values of ϵ . The low-temperature snapshot is very smooth, which is why compressing a little (panel (b)) results in a constant mean EE and flatter bond dimension. Completely smooth snapshots are self-similar, and we expect, according to Section 3.1.2 that their EE and bond dimension are constant. However, in the physical example of the Ising model, the low-temperature snapshot is not perfectly smooth (but presents fluctuations) and still without any compression, EE is constant, and the bond dimension becomes flat as we compress. This suggests that for a snapshot that is almost self-similar, or almost smooth, by compressing, we expect EE and bond dimension to become constant, or more flat than a snapshot that presents some inter-scale

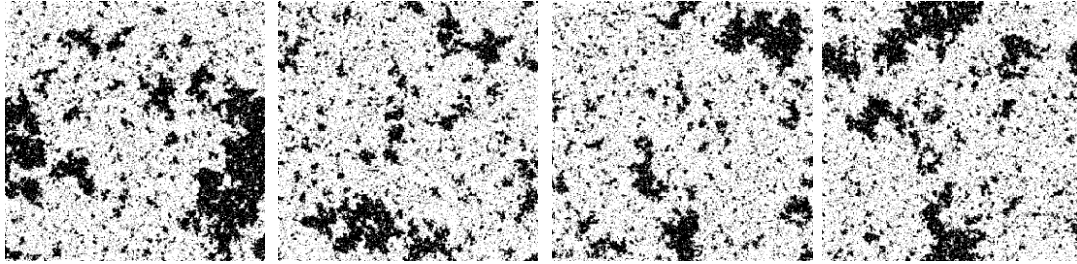


Figure 3.18: Snapshots of the 2D Ising model at $T = 2.27$.

structure. The high temperature $T = 100$ snapshot is such that each spin is random, so at any bond, the number of linearly independent sub-snapshots is maximal, and this property is, as we can see on panels (a) and (b) maintained even when compressing.

Finally, we present in Fig. 3.18 several snapshots sample of the 2D Ising model at $T = 2.270$, which is close to critical temperature. For each of the 10 samples at this temperature, we plot the EE in Fig. 3.19. We see that fluctuations occur the most in the middle bonds, but the shape of the curves are all the same, and appear to be continuous transformations of each other, although the snapshots in Fig. 3.18 look really different. So it might be that EE captures some universal feature of critical phenomena.

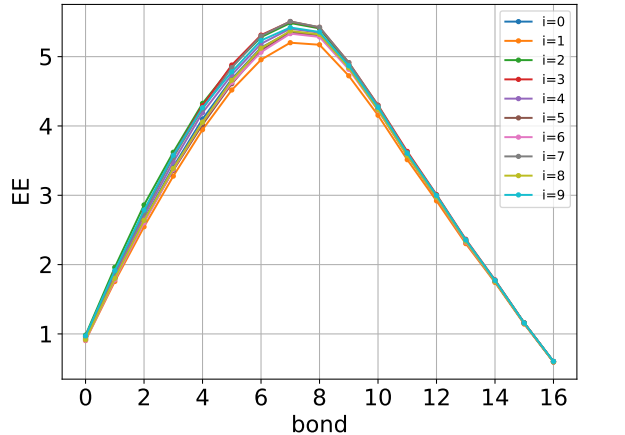
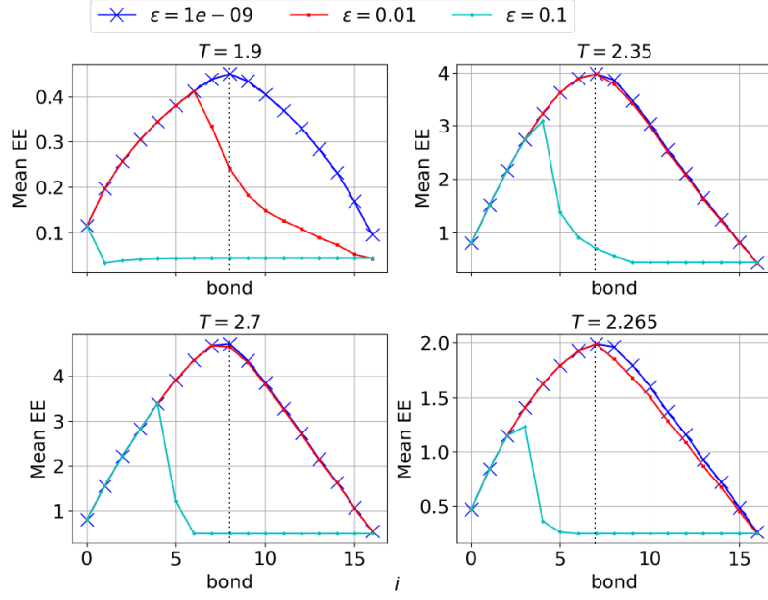
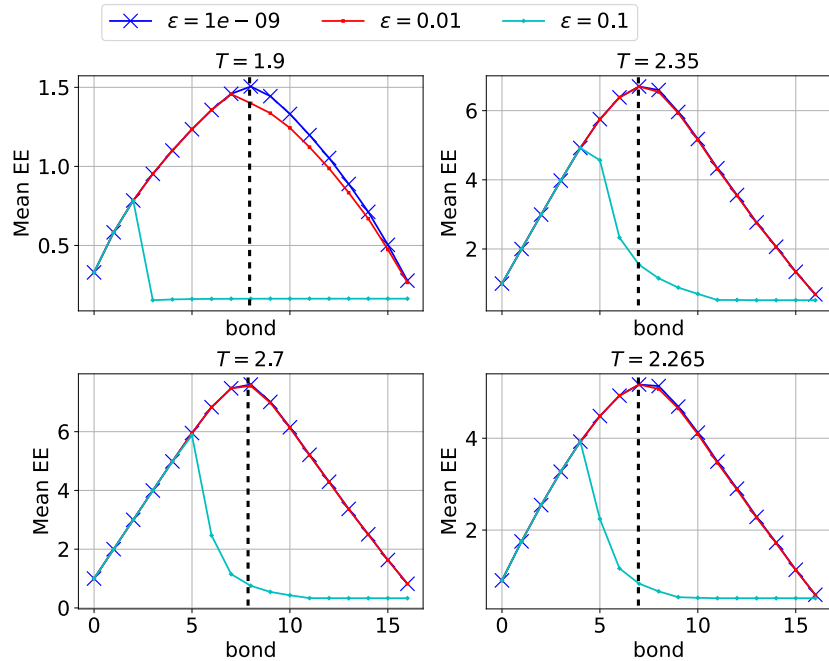


Figure 3.19: EE of each snapshot i of the 2D Ising model at $T = 2.270$.

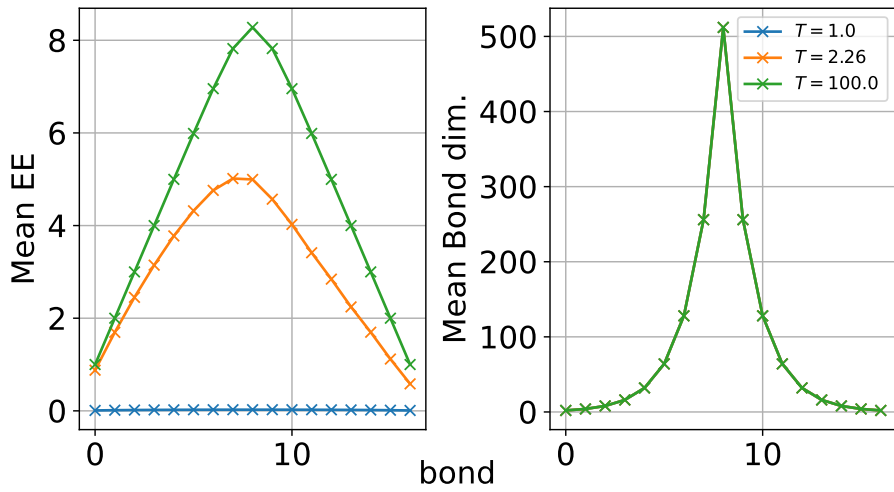


(a)

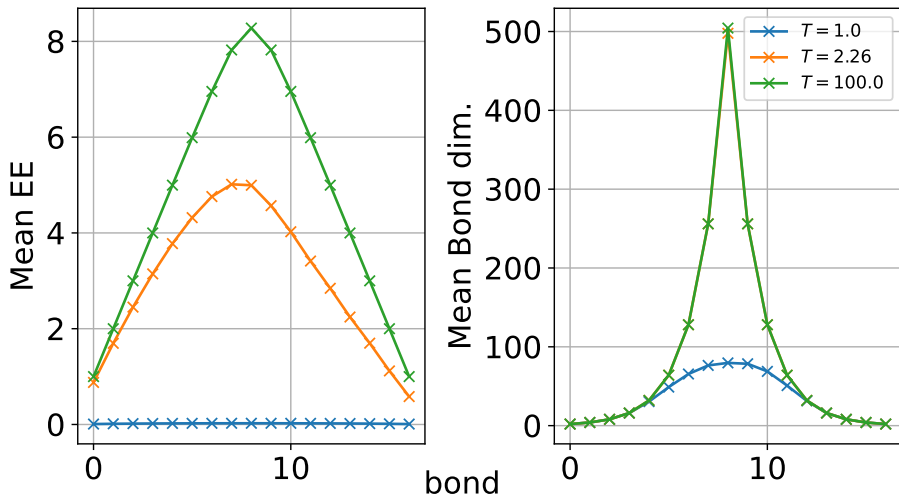


(b)

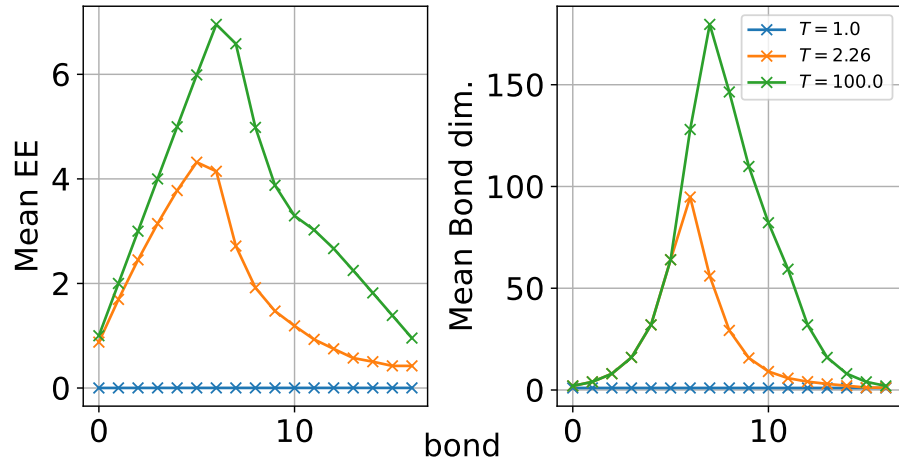
Figure 3.20: Mean EE averaged over $N_s = 10$ MC samples of 2D Ising model in a zero magnetic field for several truncation parameter ϵ . The vertical black dashed line indicates the position of the maximum of the less compressed/blue curve. System size is $2^R \times 2^R$ where $R = 9$, corresponds to a rank $L = 2R = 18$ of the MPS. Panel (a) corresponds to attributing the value 0 to the black pixel and 1 to the white pixel. Panel (b) corresponds to giving a value -1 instead of 0 to black pixel.



(a) Mean EE



(b)



(c)

Figure 3.21: Mean EE of the 2D Ising model with zero magnetic field at different T for different truncation parameter (a) : $\epsilon = 1e - 100$, (b) : $\epsilon = 0.001$ and (c) : $\epsilon = 0.05$ for $-1, 1$ encoding.

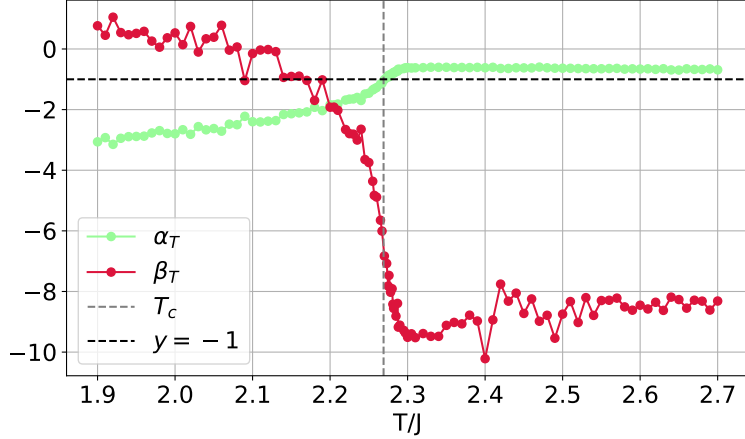


Figure 3.22: Coefficients α_T, β_T of the function that fits the island size distribution (Eq.(3.44)).

Snapshot correlation length

Consider a snapshot of our 2D Ising model. We can identify islands of spins as those pointing in the same direction and are connected with each other at least by one neighbor. Because the shape of the island varies a lot, we can only measure the size of the island as the number of spins that join that island. The island's sizes can vary with temperature, and we are interested in how these sizes are distributed, and in what measure the EE and bond dimension can give us a hint on the behavior of that distribution.

In statistical physics, the correlation length usually refers to the characteristic length scale over which the local degrees of freedom are correlated. It can be extracted by the decay of two-point correlation functions of spins or other relevant local variables.

The correlation length is not really identical to the size of the island, but there have been several studies that relate the islands and the criticality of the Ising model [32],[33].

From the sizes of these islands, we can define a *snapshot correlation length*, which is essentially the maximum size of these islands. Both quantities provide information about the structure of the system, but they capture different aspects of it. The usual correlation length in physics deals with the decay of correlations between spins, while the snapshot correlation length deals with the size of connected clusters or islands in a single snapshot of the system.

The usual correlation length is infinite in the ferromagnetic phase, however, the snapshot correlation length can be finite or infinite depending on what value of spin defines an island.

More precisely, we define an *island* as a set of nearest-neighbor spins that have spin -1 . In a given snapshot at T , several islands exist, each with a given size. Let us call $p_{\text{size},T}(\ell)$ the distribution of these sizes ℓ , that are determined using the flood fill algorithm. At each temperature, the distribution $p_{\text{size},T}(\ell)$ seem to follow a power law

$$p_{\text{size},T}(\ell) \sim \ell^{\alpha_T} \log^{-1}(\beta_T) \Rightarrow \log_2(p_{\text{size},T}(\ell)) = \alpha_T \log_2(\ell) + \beta_T \quad (3.44)$$

For several temperatures, we computed α_T, β_T for a system of size $2^9 \times 2^9$, and the result is plotted in Fig. 3.22. Let us focus on the average island size at a given T , which we will denote L_T . By

definition

$$L_T = \sum_{\ell} p_{\text{size},T}(\ell) \ell \quad (3.45)$$

where the sum runs over all possible sizes of islands at this temperature. By using the fit (3.44)

$$L_T = \log_2^{-1}(\beta_T) \sum_{\ell} \ell^{\alpha_T + 1} \quad (3.46)$$

The Figure 3.22 tells us that $\alpha_T < 0$ and that

$$\begin{cases} |\alpha_T| \geq 1 \text{ for } T \leq T_c \\ |\alpha_T| \leq 1 \text{ for } T > T_c \end{cases} \quad (3.47)$$

The fact that $\alpha_T < 0$ allows us to write

$$L_T = \log_2^{-1}(\beta_T) \sum_{\ell} \ell^{1-|\alpha_T|} \quad (3.48)$$

so by taking the \log_2 on both side

$$\log_2(L_T) = \beta_T + \log_2 \left(\sum_{\ell} \ell^{1-|\alpha_T|} \right) \quad (3.49)$$

and for $T \leq T_c$, $1 - |\alpha_T| \leq 0$, we can expand the \log_2

$$\log_2(L_T) = \beta_T + \log \left(1 + \sum_{\ell>1} \ell^{1-|\alpha_T|} \right) \quad (3.50)$$

$$\approx \beta_T + \sum_{\ell>1} \ell^{1-|\alpha_T|} \quad (3.51)$$

Fitting the Entanglement entropy

The Figure 3.23 shows 3 snapshots of the 2D Ising model, at 3 temperatures, $T = 1.9$, $T = 2.25$, $T = 2.7$ from top to down. The second column shows the bond dimension of each snapshot, and the third column shows 3 plots: the black dashed line represents $\log_2(r_i)$, which is at each bond the upper bound on the entanglement entropy (magenta curve), and the green dashed line represents $y(i) := \log_2(r_i) - S_i$, namely the difference between the maximum EE at that bond with the EE. At low temperatures, we see that the snapshot is globally smooth, with a very small island. The EE is very small compared to its upper bound because, for most scales, there is not a lot of information contained in the snapshot. However, as T increases, the EE becomes closer to its upper bound, especially in the first scales. At $T = 2.7$, we see that the green curve is zero for the first 4 bonds. It seems that if we increase temperature, on the first half-bonds, the green curve $y(i)$ has a power law behavior. Since it seems to be related to the size of the Islands, we investigate more this green curve, by fitting $y(i)$ with a power law $ai^b + c$ in the first half bonds. The parameter $c(T)$ is equal to the value at which the green curve intersects that vertical axis, and the more $c(T)$ is close to zero, the more the EE is close to its upper bond $\log_2(2) = 1$ on the first bond. The parameters $a(T)$ and $b(T)$ determine how this green curve increases in this region. The result of this fitting for a system

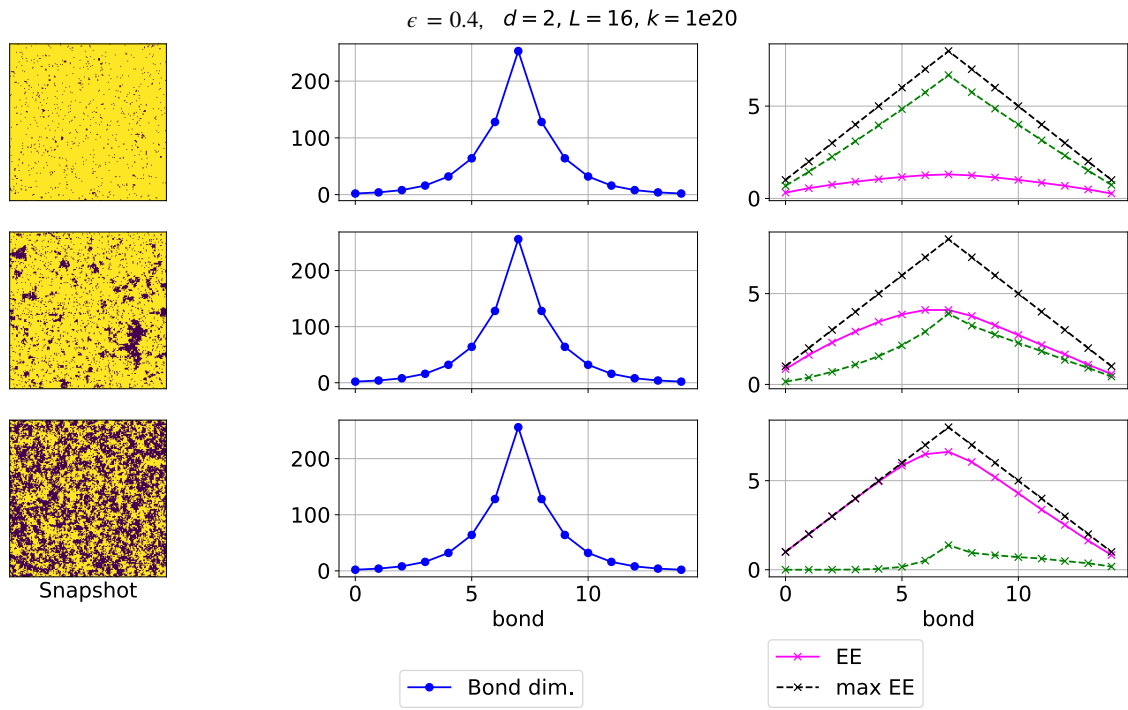


Figure 3.23: Snapshots of 2D Ising model of size $2^8 \times 2^8$.

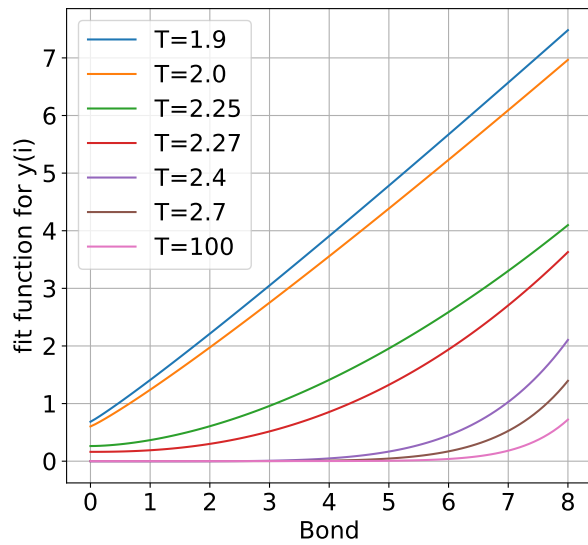


Figure 3.24: Function fitting the difference between $\log_2(r_i) - S_i$, at several temperatures.

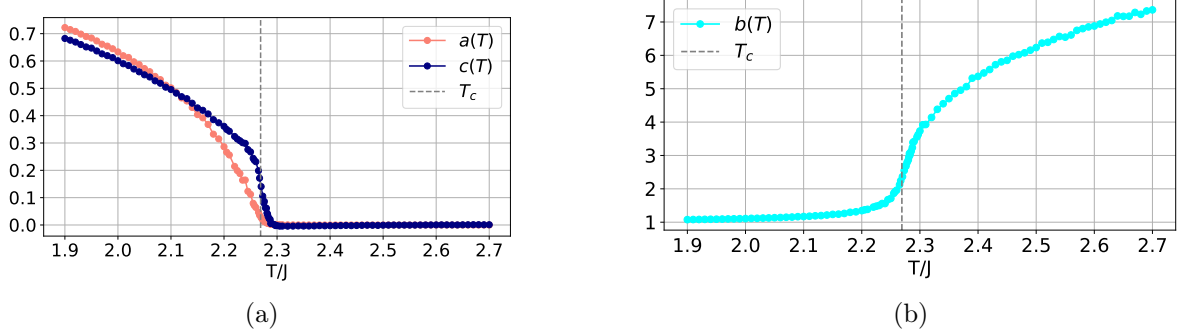


Figure 3.25: Fitting coefficient a, b, c of the function $y(i)$ with a power law $ai^b + c$.

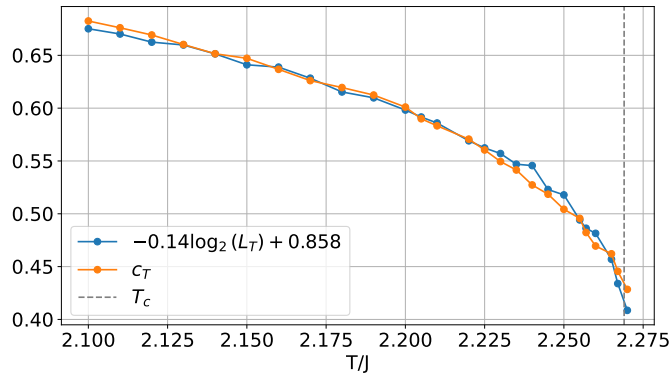


Figure 3.26: In blue, result of the optimization problem that consists in minimizing $\sqrt{(c_T - [\log_2(L_T^{a_1}) + a_2])^2}$.

with size $2^9 \times 2^9$ is presented in Fig. 3.24 and 3.25 where we respectively plot the functions of the fit and the fitting coefficients. The parameters of the MPS are such that there is no truncation: $\epsilon = 0, k = 1^{20}$. These plots confirm what we said about Fig. 3.23: as we increase the temperature, the EE becomes closer to its upper bound on the first half bonds; this is illustrated by $a(T), c(T)$ going to zero. But we have more, we observe that $a(T)$ decreases smoothly from $T = 1.9$ towards zero at T_c , whereas $c(T)$ decreases sharply at T_c , towards zero. So there is a narrow region around T_c where $c(T) \neq 0$ whereas $a(T) = 0$, and we can see this in Fig. 3.24 where green and red curves intersect the y -axis at a nonzero value.

The coefficient $b(T)$ is also increasing really sharply around T_c , and represents the increasing tail of the fitting function for $T = 2.4, 2.7, 100$.

Relation between EE and Island size

By using numerical minimization of the MSE between $\log_2(L_T^{a_1}) + a_2$ and c_T over the parameters a_1 and a_2 , it is observed that the minimal MSE is when we restrict the fit in $T \in [2.1, T_c]$, resulting in an MSE of 6.05×10^{-5} . The result with optimal parameters is presented in Fig. 3.26. We conclude that

$$\forall T \in [2.1, T_c] \quad c_T \approx -0.14 \log_2(L_T) + 0.858 \quad (3.52)$$

We are not able to explain this relation but ideally we would like to link it with the relation (3.51).

3.4 Spin-Glass

Finally, we analyze a Heisenberg model of spin glass on a cubic lattice briefly presented in Section 1.3.2. Skewed periodic boundary conditions are imposed.

3.4.1 Data available

We use the data provided by Prof. Tota Nakamura [2], obtained by the nonequilibrium relaxation method of the Monte Carlo simulation, where he measured the correlation length of the spin glass and stopped the calculation at the Monte Carlo step that the length scale reaches 1/10 of the system length. This is because when the correlation length develops further, competition between the spin-glass order and a boundary condition causes difficulties. In equilibrium Monte Carlo simulation, the spin glass phase suffers slow dynamics and it takes a very long time to equilibrate the system. For this reason, it is not possible to increase the system size to a sufficiently large scale, and the finite-size scaling analysis encounters large finite-size corrections partially due to boundaries.

Nakamura applied the dynamical scaling analysis using the spin-glass susceptibility and spin glass correlation length, choosing carefully the data that has a correlation length sufficiently smaller than the system length. The evaluation is given in the unpublished form, where $T_{SG} \sim 0.188\text{--}0.194$.

The data we analyze are both below and above T_{SG} , while because the data is not taken as equilibrium ones but has the finite spin glass correlation length which is already given by Nakamura's analysis, our analysis will provide a test case to see how such development of the correlation length may appear in what ways.

Drawing $\{J_{ij}\}$ gives a so called random bond configuration. Several random configurations are drawn independently at each temperature, let's label them by $a : \{J_{ij}\}_a$

For several bond configurations, then, $m(T)$ replicas are generated, each corresponding to an initial spin state. Then MC simulation is made to make them evolve. Call $\{\mathbf{S}_a^A(T)\}$ the set of spins on the Cubic lattice of the replica $A \in \{1, \dots, m\}$ with random bond configuration a , at temperature T .

On the lattice, each site is assigned a classical spin vector (S_{ix}, S_{iy}, S_{iz}) . The site i itself has 3 coordinates $i = (x, y, z)$ where $x, y \in \llbracket 0, L - 1 \rrbracket$ and $z \in \llbracket 0, L \rrbracket$.

The provided data is produced through Monte Carlo (MC) simulations utilizing a single-spin-flip algorithm. Each MC step comprises a single heat-bath update, followed by 124 relaxation updates, and a Metropolis update occurring once every 20 steps. Typically, the simulation runs for 10000 steps.

3.4.2 Raw and overlap snapshots

For a given 3D set $\{\mathbf{S}_a^A(T)\}$, we can extract several slices of data. The slices of data are 2D data that can be analyzed on equal footing with those of the 2D Ising model. Let us call $\alpha \in \{x, y, z\}$ the parameter that determines the plane in which the slice is taken. If $\alpha = x$, take the yz plane is extracted, if $\alpha = y$ take the xz plane. We call α_i the coordinate of the plane on the α axis.

In addition to the standard raw snapshot, for a given and fixed random configuration a and a given temperature T , we also want to generate several overlap snapshots denoted as AB , which is constructed in the following way :

Prepare two replicas A and B belonging to same a . These replica data are obtained independently in the simulation.

Take slices from replica A and replica B that have same slice parameters (α, α_i)

Create the overlap snapshot $\{\mathbf{S}_a^{AB}(T)\}$. Each site in the overlap snapshot contains data that is the product of component $\gamma \in \{x, y, z\}$ of spin in A with spin in B . We call $q_{i,\gamma,\gamma'}^{AB} = S_{i\gamma}^A S_{i\gamma'}^B$ the overlap data of site i . Here, based on the definition of replica overlap of the Heisenberg spins, the indices can be $\gamma = \gamma' = x, y, z$ and also $\gamma \neq \gamma'$ which all equivalently contribute to the spin-glass susceptibility. We test the case $q_{i,\gamma}^{AB} = S_{i\gamma}^A S_{i\gamma}^B$ for different γ .

The raw snapshots and the overlap snapshots are expressed in the RSTTF and then put in the MPS procedure, where the rank of the RSMLT is $L = 2R = 2 \cdot 8 = 16$, and each leg has dimension $d = 2$. The truncation parameter k is taken to be infinite.

Snapshot figures

Figures 3.27a, 3.28a, 3.29a, and 3.30a show the raw snapshots of a slice in the plane (x, y) whose coordinate is $z = 150$, and we take three values of compression of the MPS and $T = 0.15, 0.1945, 0.1960, 0.21$. These temperatures include the ones both above and below T_{SG} , while since these data are taken in the non equilibrium relaxation process, we need to classify them as the dynamical data, not the static spin glass state in the equilibrium. Here, we show three replicas $A = 0, 1, 2$, and the site data is chosen to be S_{ix} . We can see that the raw snapshot looks completely random.

After expressing the snapshots in RSTTF we truncate the data for $\epsilon = 0, 0.002, 0.03$ and convert them back to the real space, to see how the degree of truncation manifests. As we see, for all temperatures, the truncation will diminish the fine structure which appears in yellow but the overall figure remains the same in quality.

Figures 3.27b, 3.28b, 3.29b, and 3.30 show the overlap snapshots for three possible available pairs of replicas for $A = 0, 1, 2$. The overlap data at a given site i is the product of the x component of the spin of each replica on this site: $q_{ix}^{AB} = S_{ix}^A S_{ix}^B$.

The overlap snapshots display an apparent macroscopic structure and it does not seem to change with the degree of truncation up to $\epsilon = 0.3$.

RSTTF analysis

The question is, can we detect this structure in the RSTTF of the overlap snapshots? To answer this question, we plot the EE and bond dimension of the resulting MPS of each overlap snapshot, and compare them with the one obtained from a slice of random spins, each uniformly distributed on the unit sphere. The results are presented in Figs. 3.31, 3.32, 3.33, and 3.34. We see that at all available temperatures, the EE of the overlap spin glass snapshots starts to differ from the one of the random snapshots at bond 4. Moreover, as we compress, the bond dimension also differs from the random one, only in bonds 7 and 8.

The most surprising feature of these plots is that, all possible overlap snapshots at a given T have more or less the same EE and the same bond dimension, which was *not the case of the 2D critical Ising model* (Fig. 3.19).

To compare the EE and bond dimension of the spin glass overlap snapshots at different temperatures, we plot EE for each of the available T in the same plot. We do it for the three different overlap

function $q_{ix}^{AB}, q_{iy}^{AB}, q_{iz}^{AB}$ and each column in Fig. 3.35 corresponds to one, where each row corresponds to a truncation parameter ϵ . We see on the zoomed plot that all the curves have the same shape, but at all bond, as we increase the temperature, the EE becomes higher.

Finally, as we did in Section 3.2, we computed the truncation error $e(k = \infty, \epsilon)$ for a spin glass snapshot overlap and a random spin slice, and result is presented in Fig. 3.36. As expected due to the development of correlation length in the overlap snapshot, the compression produces more quickly a loss of information on the random snapshots than on the overlap snapshots.

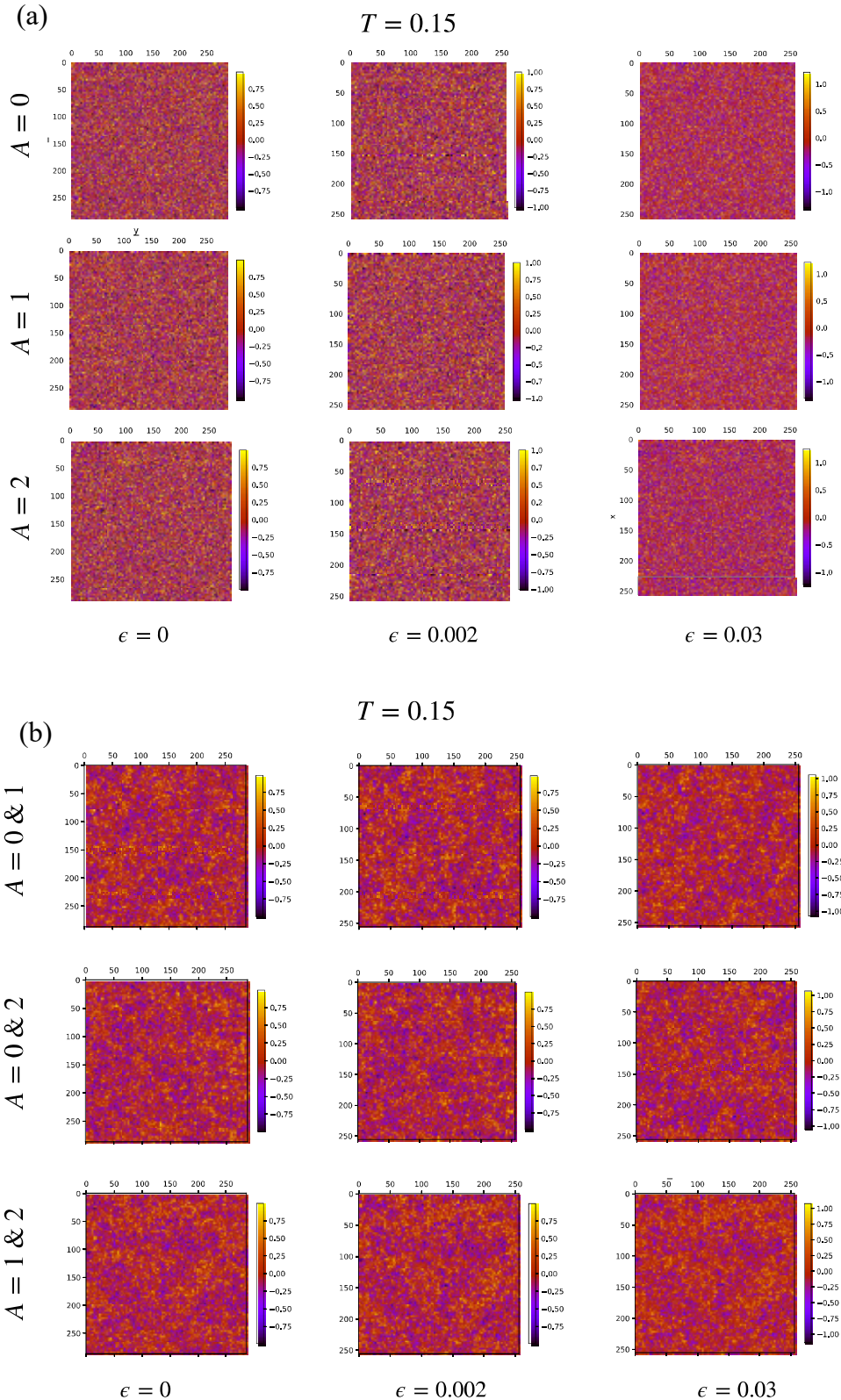


Figure 3.27: The first column shows the (a) raw (b) overlap spin glass snapshots, without any MPS procedure, at $T = 0.15$. The middle and last columns show the snapshots after compression in the MPS. When $A = a\&b$, overlap between replica n and m is made.

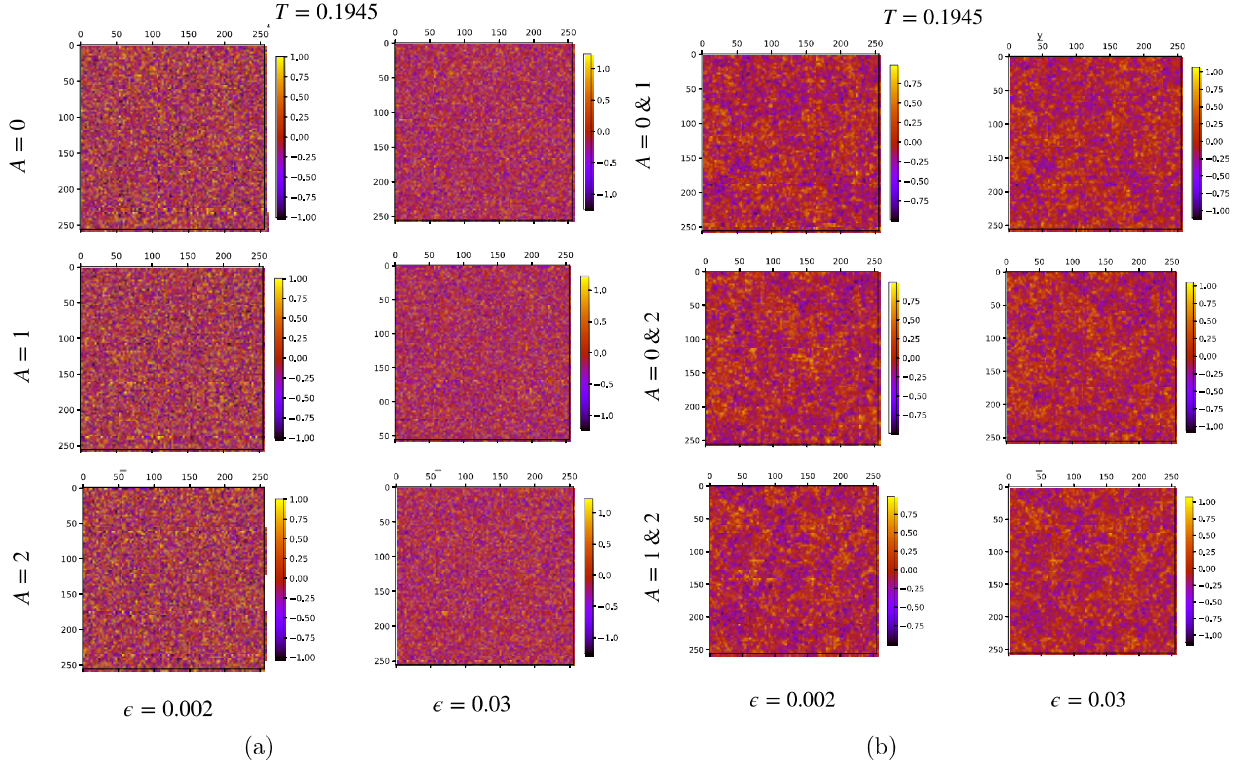


Figure 3.28: The first column shows the (a) raw (b) overlap spin glass snapshots, without any MPS procedure, at $T = 0.1945$. The middle and last columns show the snapshots after compression in the MPS. When $A = a\&b$, overlap between replica n and m is made.

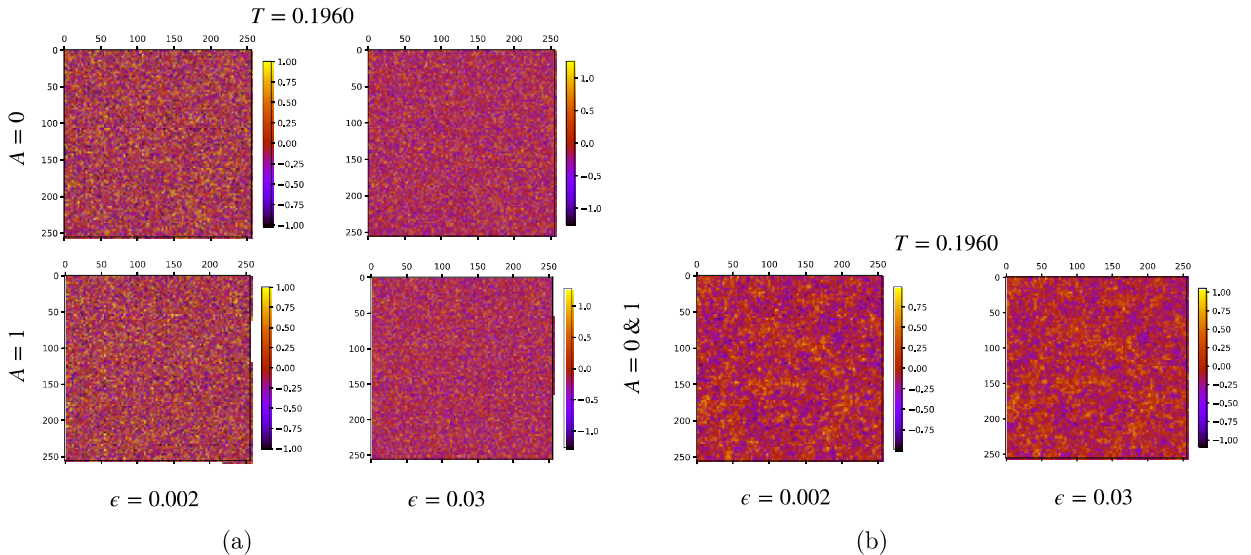


Figure 3.29: The first column shows the (a) raw (b) overlap spin glass snapshots, without any MPS procedure, at $T = 0.1960$. The middle and last columns show the snapshots after compression in the MPS. When $A = a\&b$, overlap between replica n and m is made.

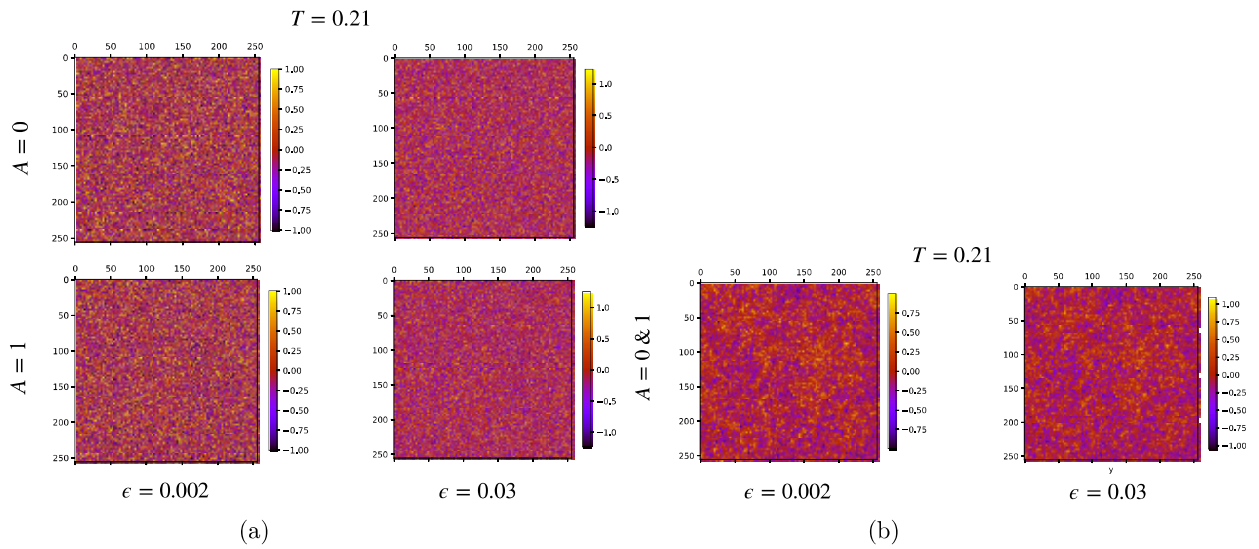


Figure 3.30: The first column shows the (a) raw (b) overlap spin glass snapshots, without any MPS procedure, at $T = 0.2100$. The middle and last columns show the snapshots after compression in the MPS. When $A = a \& b$, overlap between replica n and m is made.

$T = 0.15$

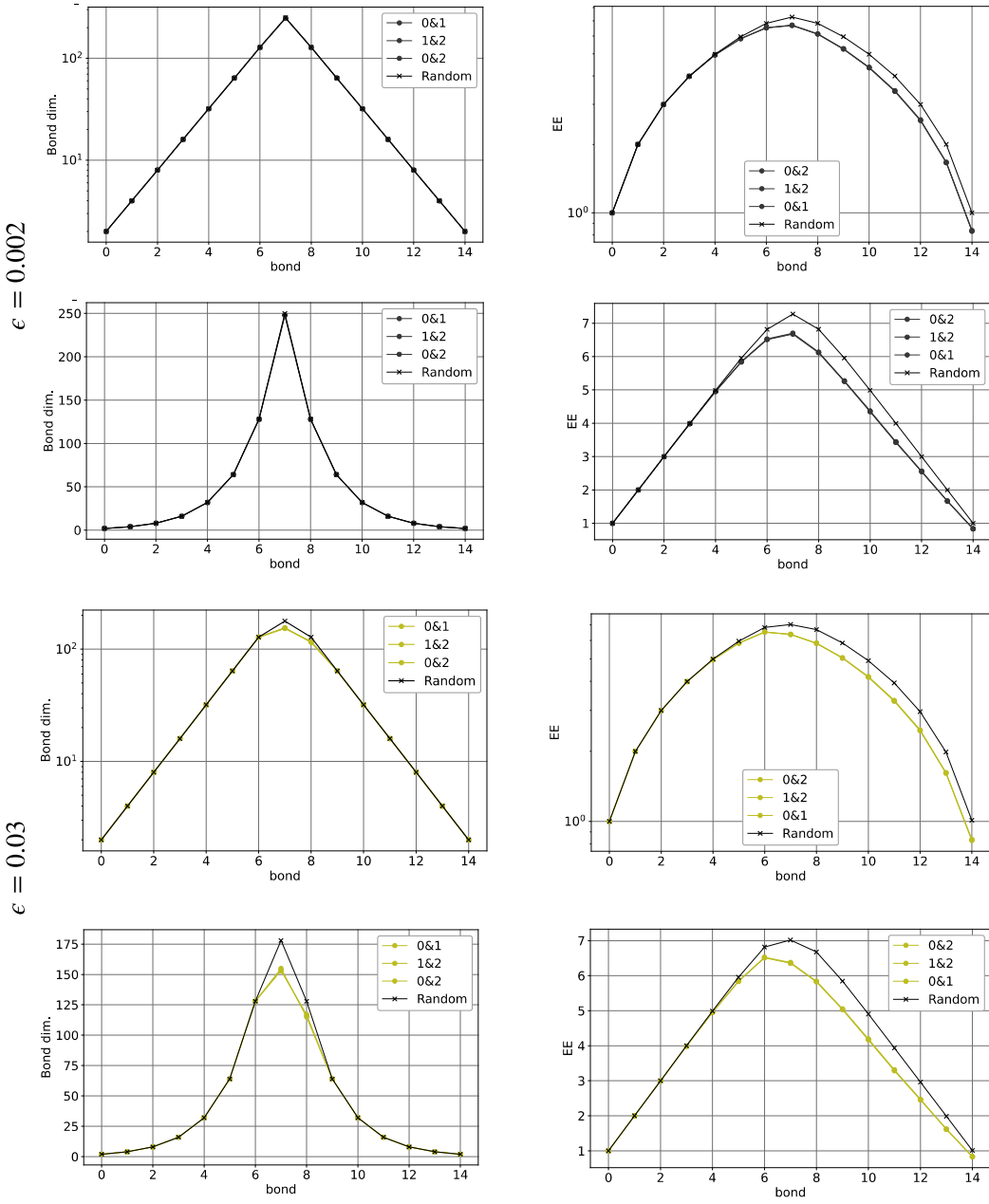


Figure 3.31: $T = 0.15$. The upper four figures show the bond dimension and EE in the semilog scale (upper 2 figures) and also in the linear-linear scale (down 2 figures), of the spin glass overlap snapshots, and also of the random snapshot. The down four figures show the same but with another truncation parameter.

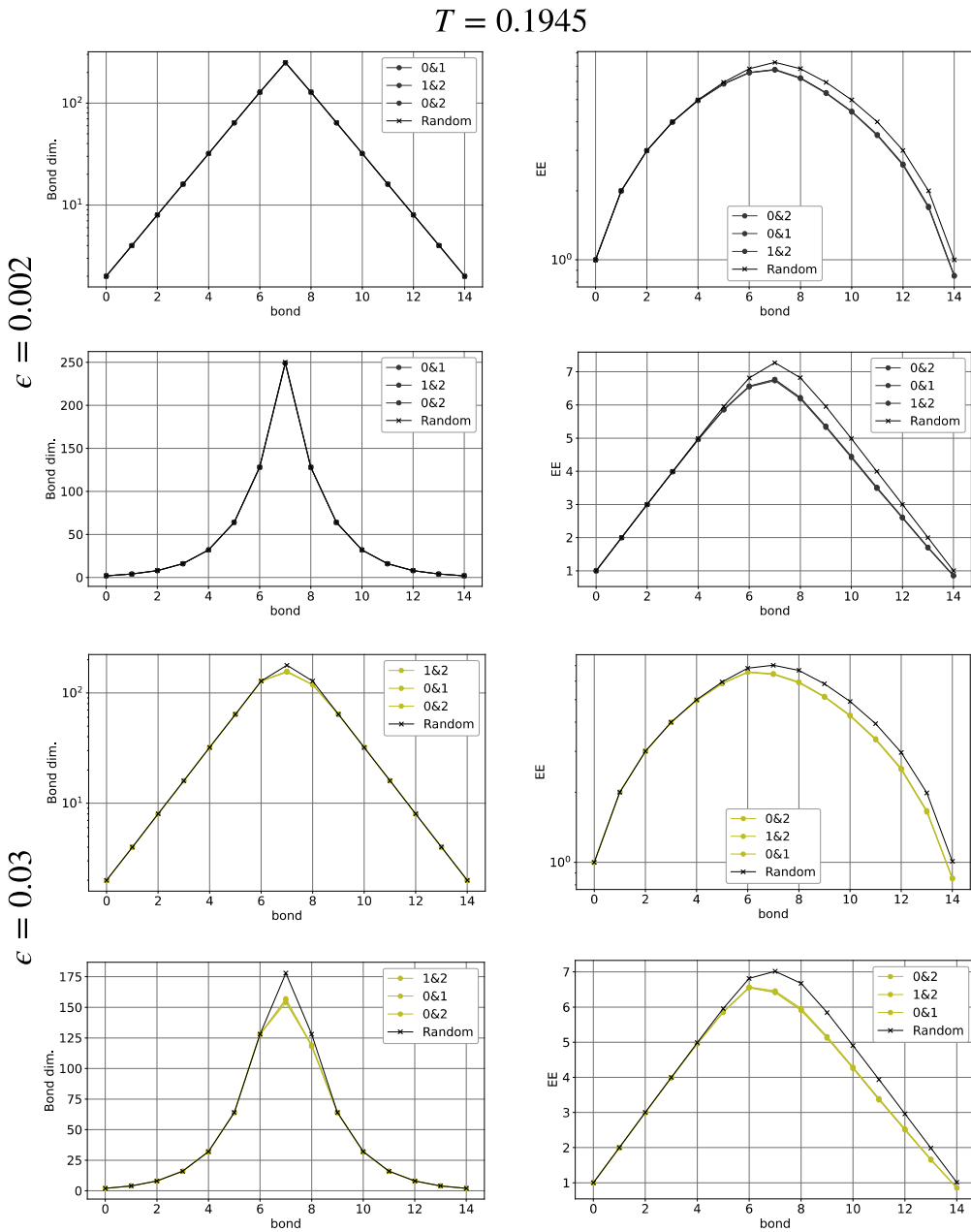


Figure 3.32: $T = 0.1945$. The upper four figures show the bond dimension and EE in the semilog scale (upper 2 figures) and also in the linear-linear scale (down 2 figures), of the spin glass overlap snapshots, and also of the random snapshot. The down four figures show the same but with another truncation parameter.

$T = 0.1960$

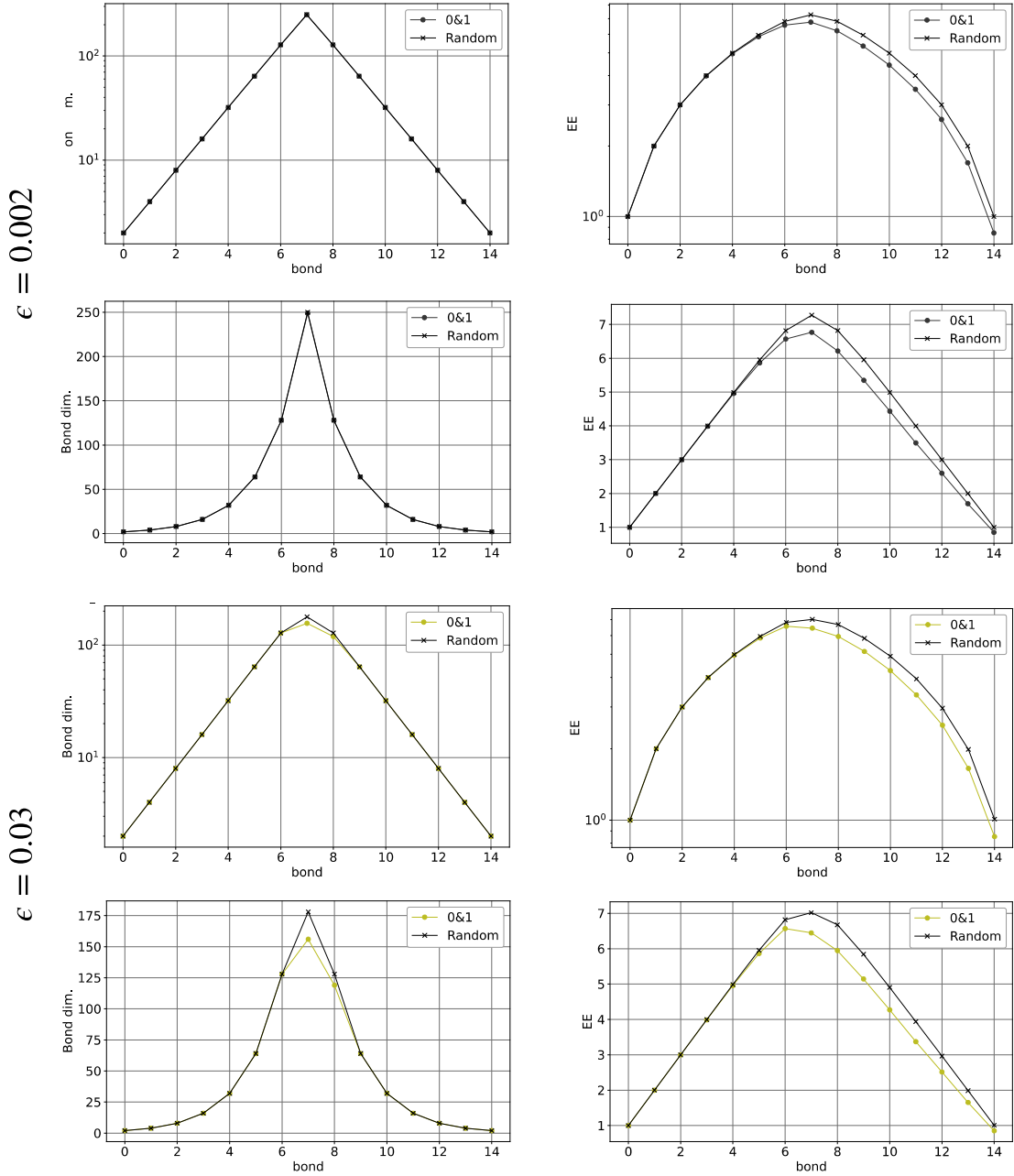


Figure 3.33: $T = 0.1960$. The upper four figures show the bond dimension and EE in semilog scale (upper 2 figures) and also in the linear-linear scale (down 2 figures), of the spin glass overlap snapshots, and also of the random snapshot. The down four figures show the same but with another truncation parameter.

$T = 0.21$

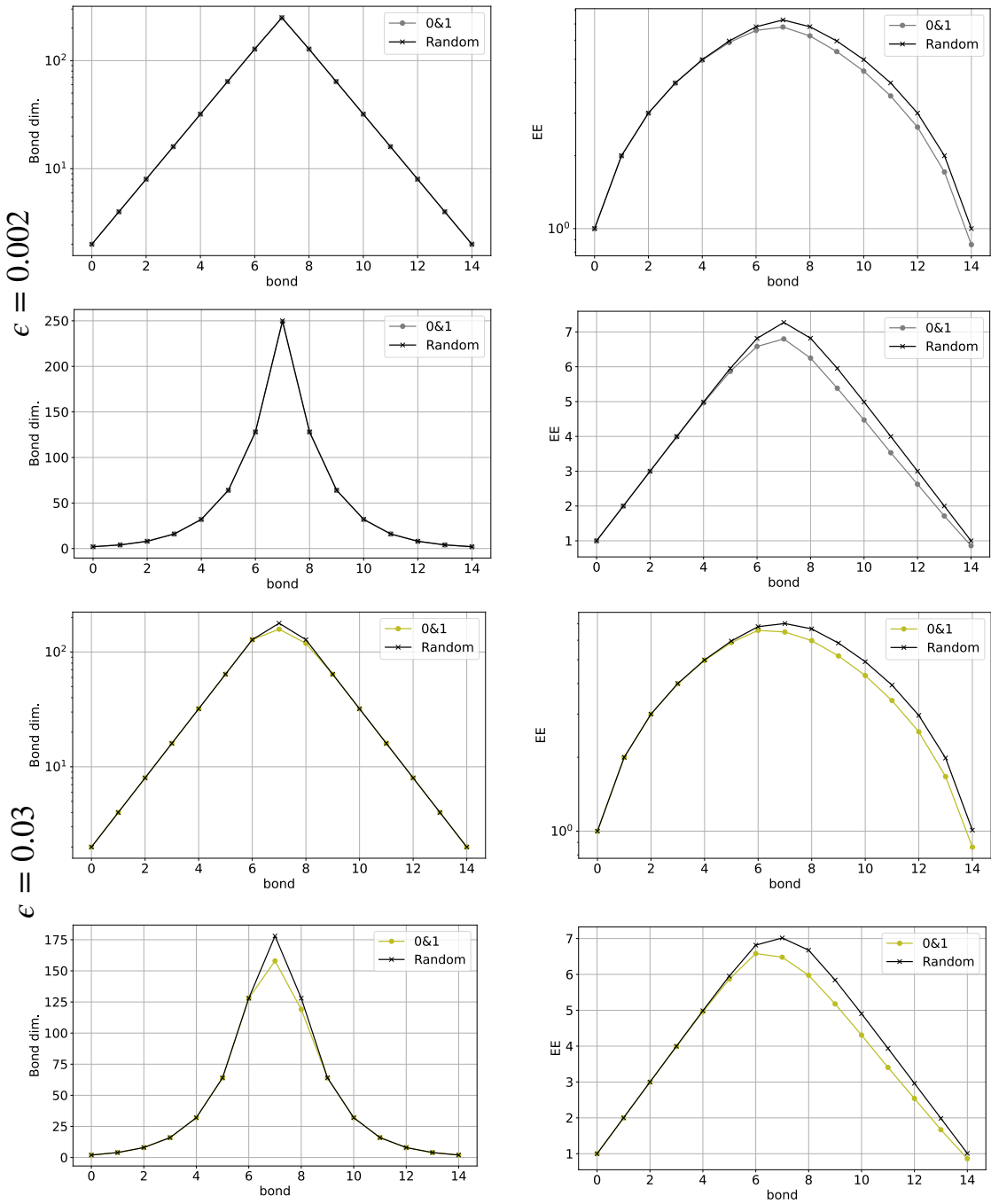
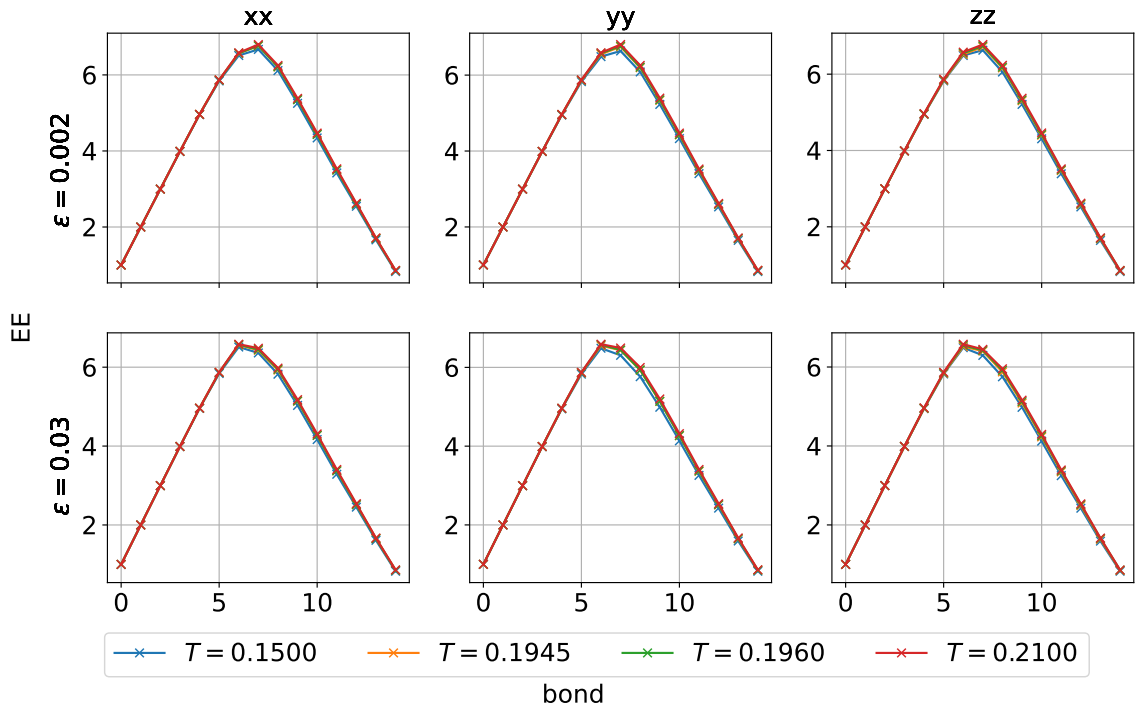
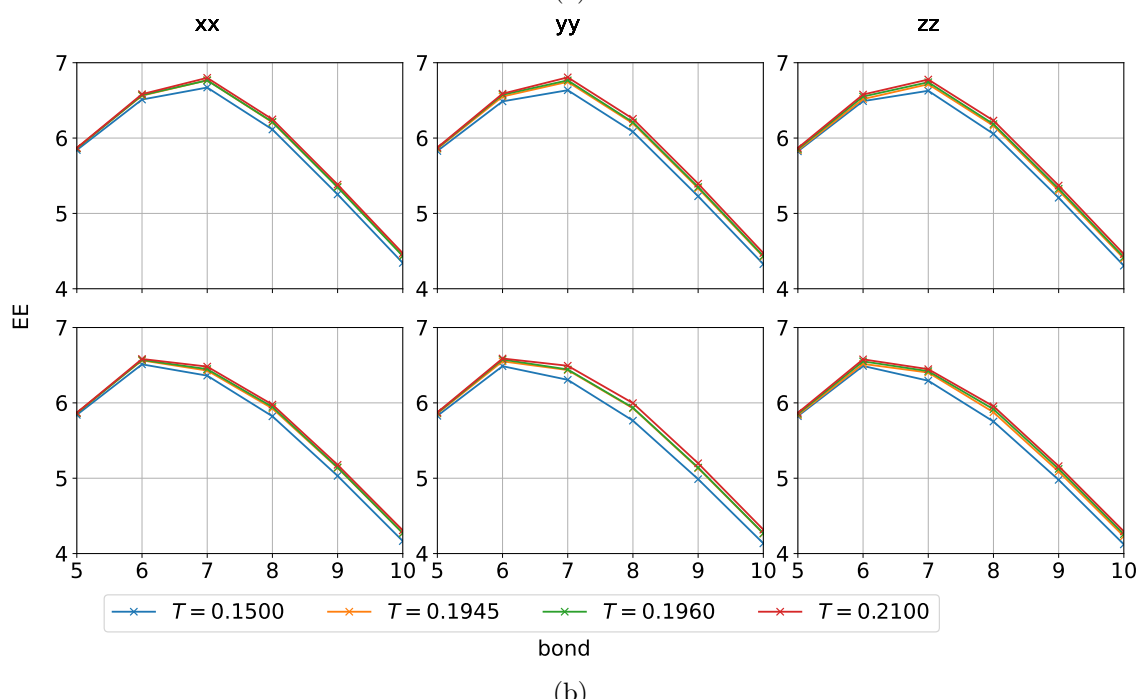


Figure 3.34: $T = 0.2100$. The upper four figures show the bond dimension and EE in the semilog scale (upper 2 figures) and also in the linear-linear scale (down 2 figures), of the spin glass overlap snapshots, and also of the random snapshot. The down four figures show the same but with another truncation parameter.



(a)



(b)

Figure 3.35: Comparison of EE of spin glass overlap snapshots as temperature changes. Panel (a) is zoomed and presented in (b). The overlap is made between $A = 0$ and $A = 1$.

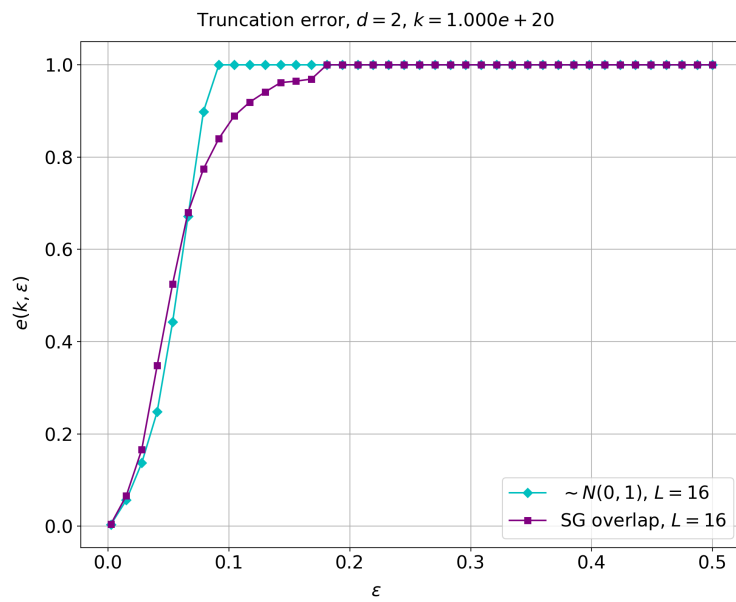


Figure 3.36: Truncation error for an overlap snapshot between $A = 0$ and $A = 1$ of $T = 0.15$ for $q_{ix}^{AB} = S_{ix}^A S_{ix}^B$ and $(\alpha, \alpha_i) = (x, 150)$ and for a slice where each spin point randomly on the unit sphere.

Chapter 4

Conclusion

Detecting or characterizing physical phases of matter relied often on the examination of correlation length, extracted from the two-point correlation function of local observables. However, studies developed over the decades defy Landau’s paradigm, showing that there are more phases than the ones that can be characterized by such locally defined order parameters, such as those belonging to the correlated disorders including spin liquid, spin ice, and spin glasses. These cases lack the local order parameter and the accumulation of knowledges about e.g. entanglement structure, pinch point singularity, replica symmetry breaking, has served as a tool to clarify these phases. However, the question arises: even though our eyes cannot discriminate them from a simple paramagnetic disorder or a purely random state, maybe the machines can detect them.

In this thesis, we proposed a new approach to analyze the snapshot defined as a discrete D -dimensional data set using one of the machineries developed recently. The idea is to know how the profiles of data belonging to different scales are entangled with each other. Focusing on the $D = 2$ case, we made several trials to characterize the inter-scale relations to deduce some property of the underlying data/phase of matter.

The fundamental component of this approach is the RSTTF, which encodes the data as a product of matrices, with physical indices representing different scales of the data. We analytically demonstrated that if some data is self-similar at a particular scale, the Entanglement Entropy (EE) and bond dimension will remain constant across the bonds within that scale. We have exactly computed the EE and bond dimension of the Quantum Cantor Set (QCS) for different types of encoding analytically, and have posed the problem of the facultativity of the data, introducing a new perspective on compression by selecting appropriate data to attribute to pixels, such as minimizing the EE.

Additionally, we have numerically detected the ferromagnetic-paramagnetic phase transition of the 2D Ising model with a very sharp transition in the total EE, using only 10 Monte Carlo (MC) samples for each temperature, and determined the critical temperature. Furthermore, we apply the method to overlaps of slices of a cubic lattice following the Heisenberg Edwards–Anderson model. We found that the EE, as a function of the bond, differs from that obtained from a slice with random spins, indicating the development of the correlation length. We confirm that no such development appears in the raw snapshots.

There are still some unresolved aspects that trigger further investigation. Specifically, we are interested in developing a method to infer the distribution of island sizes from the Entanglement Entropy (EE). Additionally, we aim to extend our analysis to detect the Spin Glass transition, similar to how we successfully identified the transition in the 2D Ising model. We think that these aspects

can be clarified by relating more quantitatively the island size and critical exponent.

Acknowledgements

I would like to express my gratitude to Professor Chisa Hotta for her availability and enthusiasm towards the project, and for guiding me through all procedures in Japan and abroad. My sincere thanks to the lab members of the Hotta group for warmly welcoming me and providing guidance during my time in Japan. Additionally, I extend my appreciation to Professor Frederic Mila for his invaluable support and guidance.

Bibliography

- [1] Shmuel Friedland and Venu Tammali. Low-rank approximation of tensors. In *Numerical Algebra, Matrix Theory, Differential-Algebraic Equations and Control Theory: Festschrift in Honor of Volker Mehrmann*, pages 377–411. Springer, 2015.
- [2] Tota Nakamura. Strategy for solving difficulties in spin-glass simulations. *Physical Review E*, 99(2):023301, 2019.
- [3] Barry M McCoy and Tai Tsun Wu. *The two-dimensional Ising model*. Harvard University Press, 1973.
- [4] Lars Onsager. Crystal statistics. i. a two-dimensional model with an order-disorder transition. *Physical Review*, 65(3-4):117, 1944.
- [5] Bruria Kaufman. Crystal statistics. ii. partition function evaluated by spinor analysis. *Physical Review*, 76(8):1232, 1949.
- [6] Mark Kac and John C Ward. A combinatorial solution of the two-dimensional ising model. *Physical Review*, 88(6):1332, 1952.
- [7] Renfrey B Potts and John C Ward. The combinatrial method and the two-dimensional ising model. *Progress of Theoretical Physics*, 13(1):38–46, 1955.
- [8] Elliott W. Montroll, Renfrey B. Potts, and John C. Ward. Correlations and Spontaneous Magnetization of the Two-Dimensional Ising Model. *Journal of Mathematical Physics*, 4(2):308–322, February 1963.
- [9] Hendrik A Kramers and Gregory H Wannier. Statistics of the two-dimensional ferromagnet. part i. *Physical Review*, 60(3):252, 1941.
- [10] Elliott H Lieb. Solution of the dimer problem by the transfer matrix method. In *Condensed Matter Physics and Exactly Soluble Models: Selecta of Elliott H. Lieb*, pages 537–539. Springer, 2004.
- [11] Matt Bierbaum. <https://github.com/mattbierbaum/ising.js?tab=readme-ov-file>, 2014.
- [12] JL Cambier and M Nauenberg. Distribution of fractal clusters and scaling in the ising model. *Physical Review B*, 34(11):8071, 1986.
- [13] Samuel Frederick Edwards and Phil W Anderson. Theory of spin glasses. *Journal of Physics F: Metal Physics*, 5(5):965, 1975.

- [14] Marc Mézard, Giorgio Parisi, and Miguel Angel Virasoro. *Spin glass theory and beyond: An Introduction to the Replica Method and Its Applications*, volume 9. World Scientific Publishing Company, 1987.
- [15] Flaviano Morone, Francesco Caltagirone, Elizabeth Harrison, and Giorgio Parisi. Replica theory and spin glasses. *arXiv preprint arXiv:1409.2722*, 2014.
- [16] Ada Altieri and Marco Baity-Jesi. An introduction to the theory of spin glasses. *arXiv preprint arXiv:2302.04842*, 2023.
- [17] Hiroshi Shinaoka, Markus Wallerberger, Yuta Murakami, Kosuke Nogaki, Rihito Sakurai, Philipp Werner, and Anna Kauch. Multiscale space-time ansatz for correlation functions of quantum systems based on quantics tensor trains. *Physical Review X*, 13(2):021015, 2023.
- [18] Marc K Ritter, Yurie Núñez Fernández, Markus Wallerberger, Jan von Delft, Hiroshi Shinaoka, and Xavier Waintal. Quantics tensor cross interpolation for high-resolution, parsimonious representations of multivariate functions in physics and beyond. *arXiv preprint arXiv:2303.11819*, 2023.
- [19] Ivan V Oseledets. Tensor-train decomposition. *SIAM Journal on Scientific Computing*, 33(5):2295–2317, 2011.
- [20] Ivan V Oseledets. Approximation of $2^d \times 2^d$ matrices using tensor decomposition. *SIAM Journal on Matrix Analysis and Applications*, 31(4):2130–2145, 2010.
- [21] Erika Ye and Nuno FG Loureiro. Quantum-inspired method for solving the vlasov-poisson equations. *Physical Review E*, 106(3):035208, 2022.
- [22] Nikita Gourianov, Michael Lubasch, Sergey Dolgov, Quincy Y van den Berg, Hessam Babaee, Peyman Givi, Martin Kiffner, and Dieter Jaksch. A quantum-inspired approach to exploit turbulence structures. *Nature Computational Science*, 2(1):30–37, 2022.
- [23] Jose I Latorre. Image compression and entanglement. *arXiv preprint quant-ph/0510031*, 2005.
- [24] Yukinari Imura, Tsuyoshi Okubo, Satoshi Morita, and Kouichi Okunishi. Snapshot spectrum and critical phenomenon for two-dimensional classical spin systems. *Journal of the Physical Society of Japan*, 83(11):114002, 2014.
- [25] John Michael Kosterlitz and David James Thouless. Ordering, metastability and phase transitions in two-dimensional systems. In *Basic Notions Of Condensed Matter Physics*, pages 493–515. CRC Press, 2018.
- [26] Alexander Yu Shibakov and Andrzej Trybulec. The cantor set. *Formalized Mathematics*, 5(2):233–236, 1996.
- [27] Frank Verstraete and J Ignacio Cirac. Matrix product states represent ground states faithfully. *Physical review b*, 73(9):094423, 2006.
- [28] Lambert Lin and Steven R White. A novel method of function extrapolation inspired by techniques in low-entangled many-body physics. *arXiv preprint arXiv:2308.09001*, 2023.

- [29] Kenji Harada. Bayesian inference in the scaling analysis of critical phenomena. *Physical Review E*, 84(5):056704, 2011.
- [30] Tota Nakamura. From measurements to inferences of physical quantities in numerical simulations. *Physical Review E*, 93(1):011301, 2016.
- [31] Tota Nakamura. Machine learning as an improved estimator for magnetization curve and spin gap. *Scientific Reports*, 10(1):14201, 2020.
- [32] Masuo Suzuki. Phase transition and fractals. *Progress of Theoretical Physics*, 69(1):65–76, 1983.
- [33] K Binder. “clusters” in the ising model, metastable states and essential singularity. *Annals of physics*, 98(2):390–417, 1976.